MXene Rheology and Phase Behavior: Exploring the Effects of Sheet Size and Salt Addition

by

Mackenzie B. Woods

A dissertation submitted to the Graduate Faculty of
Auburn University
in partial fulfillment of the
requirements for the Degree of
Doctor of Philosophy

Auburn, Alabama
December 9, 2023

Keywords: nanomaterials, MXenes, microstructure, rheology, liquid crystals

Approved by

Virginia A. Davis, Chair, Daniel F. and Josephine Breeden Professor, Chemical Engineering
Bryan S. Beckingham, Associate Professor of Chemical Engineering
Tae-Sik Oh, Assistant Professor of Chemical Engineering
Majid Beidaghi, Associate Professor of Materials Engineering
Kyle Schulze, Assistant Professor of Mechanical Engineering

Abstract

The overall research goal of this dissertation is to understand the effects of sheet size and salt addition on the phase behavior and rheological properties of aqueous MXene dispersions. The charged surfaces of the MXenes, their irregular shape, and the polydispersity that ensues from their synthesis process complicates the extension of two-dimensional (2D) colloid fundamental knowledge to this recently discovered family of nanomaterials. This research provides an increased fundamental understanding of aqueous $Ti_3C_2T_x$ MXene behavior through the tuning of sheet size, MXene concentration, and ionic strength. The knowledge gained of MXene lyotropic liquid crystalline behavior and associated rheological properties can be directly utilized to improve the processability of MXenes in fluid-phase manufacturing methods, such as direct ink writing. Through consideration of MXenes as a specific example within the family of 2D colloids, the knowledge gained through this work improves the overall current scientific understanding of 2D materials by providing new insights to classical colloid science questions.

The first half of this research focused on investigating three size fractions of $Ti_3C_2T_x$ MXenes: large MXene sheets with an average longest lateral dimension of ~3 μm, small MXene sheets with an average longest lateral dimension of ~0.3 μm, and a bimodal mixture of large and small MXene sheets. A series of concentrations of each MXene size fraction was studied through polarized optical microscopy (POM) and steady and oscillatory shear rheology to elucidate the effects of selective size polydispersity on lyotropic liquid crystalline phase transitions. Changes in microstructure and rheological properties as a function of MXene concentration and sheet size provided experimental evidence necessary to produce the first phase transition chart for aqueous size fractionated MXene dispersions. Dispersions of large MXene sheets were observed to readily form long-range liquid crystalline alignment at relatively low concentrations; however, they also

exhibited a tendency toward aggregation as concentration was increased. Small MXene dispersions remained more stable throughout increasing concentration. Signatures of liquid crystallinity were not observed in small MXene dispersions, indicating that the smaller sheets were unable to form extended aligned structures. A 1:1 bimodal mixture of large and small MXenes served as a selectively polydisperse size fraction to compare to the more monodisperse large MXene and small MXene dispersions. The inclusion of small MXene sheets into dispersions of large MXenes resulted in increased stability while maintaining the ability to achieve liquid crystalline alignment. Signatures of liquid crystallinity in bimodal MXene dispersions occurred at slightly higher concentrations than that observed in monodisperse large MXene dispersions; however, the resistance toward aggregation is a desirable characteristic for fluid-phase processing.

The second half of this work involved the addition of sodium chloride (NaCl) to increase the ionic strength of bimodal MXene dispersions. By investigating the effects of ionic strength on dispersion phase behavior, microstructure, and associated rheological properties, the effectiveness of utilizing NaCl as a rheological modifier to aqueous MXene dispersions and inks could be revealed. It was observed that low concentrations of NaCl could induce increased rheological properties, including yield stress and storage modulus (G'), in lower concentrations of MXenes. At higher concentrations of MXenes (0.80 vol % and greater) the addition of NaCl was observed to initially weaken the percolated structure of MXenes, resulting in lower rheological properties. However, slightly raising the ionic strength of these dispersions increased the rheological properties above that of the 0 M dispersions. As expected from fundamentals of colloid science, high concentrations of NaCl (0.5 M) resulted in dispersion instability and severe flocculation of MXene sheet. This behavior was observed across an order of magnitude of concentrations (0.10 – 1.00 vol %), indicating that low MXene concentrations are not resistant to flocculation. The results

from this research produced a MXene/NaCl phase diagram consisting of nematic liquid crystalline phases.

Acknowledgements

This work was achieved through the help of so many people. I thank my advisor, Dr. Virigina Davis, for guiding me through the years of graduate school, research, and academic growth. I also thank Dr. Majid Beidaghi and his research group for their collaboration on this work. I appreciate the rest of my committee, Dr. Bryan Beckingham and Dr. Tae-Sik Oh, and their continued advisement throughout the extent of my research. Thank you also to my university reader, Dr. Kyle Schulze, for aiding in the development of this dissertation. This research was funded by the National Science Foundation Award Number 2005413 and the U.S. Department of Education GAANN Fellowship.

Thank you to Dr. Fatima Hamade for your trainings, knowledge, and guidance throughout graduate school and MXene research. I also thank prior lab group members Dr. Matthew Noor and Dr. Zahra Karimi for their trainings and advice in the lab. Thank you to Elnaz Jamshidi and Shahrouz Zamani for their efforts in synthesizing the MXenes for this work and collaboration with MXene printability. I thank the undergraduate researchers that I worked with and mentored – Rory Luthin, for the excellent preliminary work with MXene printing, and Lindsay Parsons, for the collaborative work with the phase behavior of manganese dioxide nanowires. To all of my colleagues, Dr. Fatima Hamade, Dr. Matthew Noor, Dr. Zahra Karimi, Madhuri Nori, Sadat Amit, Delaney Clouse, Daniel Meadows, Tanmay Rahman, and Francis Mekunye, I thank you for the wonderful graduate research experience that I have had. I appreciate all of the collaborative efforts, office discussions, group lunches, and unending support that helped me to succeed.

A special thank you to my family and friends, without whom I would not be where I am today. To my husband, Andy Woods, I thank you for the overabundance of support, love, and guidance you have given me over the years. Thank you for encouraging me through the long days

that went into this research – without you, I could not have accomplished it all. I will always be so thankful for our Auburn years. To my parents, Don and Sandi Bockhold, thank you for believing in me since the very beginning, encouraging me to pursue my passions, and maintaining a solid foundation for me to always lean on. To all my siblings – Ashley, Emily, Dax, Grayson, and Silas, I thank you for your constant love and support and for always making me look forward to coming home. To my in-laws, the Woods family – Al, Carrie, Chris, Mollie, and Sarah, thank you for welcoming me into your family with open arms and cheering me on throughout the years. To the wonderful friends Auburn has given me – Ali Bradford, Delaney Clouse, Nicole Habbit, Katie Lawson, and Paige Kington, thank you so much for all the girls' nights, beach trips, tailgates, and the random Jeff Foxworthy show. Those times will remain some of my best memories, and I will always treasure the bonds we formed here at Auburn University.

Last, but most importantly, I want to thank God for the grace and the gifts He has bestowed upon me that have resulted in where I am today, and my Catholic faith for grounding me throughout these past years. I owe all that I am and have accomplished to Him.

Table of Contents

List of Tables

List of Figures

List of Abbreviations

1D	One-dimensional
2D	Two-dimensional
3D	Three-dimensional
AFM	Atomic Force Microscopy
B	Biphasic
B-MXene	Bimodal MXenes
C	Columnar
DI	Deionized Water
DIW	Direct-Ink-Writing
DLVO	Derjaguin-Landau-Verwey-Overbeek
EDL	Electric Double Layer
EV	Electroviscous
F	Flocculation
G	Gel
GO	Graphene Oxide
I	Isotropic
IG	Isotropic Gel
ITO	Indium Tin Oxide
LC	Liquid Crystal
L-MXene	Large MXenes
MILD	Minimally Intensive Layer Delamination
N	Nematic

NG	Nematic Gel
NW	Nanowire
rGO	Reduced Graphene Oxide
SANS	Small Angle Neutron Scattering
SAOS	Small Amplitude Oscillatory Shear
SAXS	Small Angle X-Ray Scattering
SEM	Scanning Electron Microscopy
S-MXene	Small MXenes
TGA	Thermal Gravimetric Analysis
TMV	Tobacco Mosaic Virus
UV-vis	Ultraviolet-Visible
vdW	van der Waals

Chapter 1 – Introduction

The objective of this research was to elucidate the effects of sheet size and salt addition on the phase behavior and rheological properties of aqueous MXene ($Ti_3C_2T_x$) dispersions. In this work, three size fractions of MXenes were investigated: large MXenes (denoted as L-MXenes) with an average lateral dimension of ~3 μm, small MXenes (denoted as S-MXenes) with an average lateral dimension of ~0.3 μm, and a bimodal mixture of 50% L-MXene and 50% S-MXene by volume (denoted as B-MXenes). The contribution of this work will extend beyond MXene dispersions to other two-dimensional (2D) nanomaterial dispersions in both furthering fundamental understanding and increasing practical use without the extent of the time and financial obligation that many current trial-and-error research methods require.

Exploration of the lyotropic liquid crystalline phase behavior of anisotropic nanomaterial dispersions is advancing fundamental colloid science and enabling the manufacture of aligned materials through fluid-phase processes, such as direct-ink-writing and wet fiber spinning.[1-4] Lyotropic liquid crystals are mesophases where a rigid or semi-rigid anisotropic material (called a mesogen) spontaneously aligns with increasing concentration because the gain in translational entropy associated with ordering more than offsets the loss in rotational entropy. In Onsager's seminal 1949 theory for monodisperse spherocylinders in an athermal solvent, this ordering was solely a function of the length to diameter ratio of the mesogen; more recent refinements have accounted for the impacts of polydispersity and thermodynamic interactions.[5-7] In increasing the understanding of lyotropic phase behavior, the manufacturing of aligned materials through fluid-phase processes can be significantly advanced.[1-4] This has already been proven with the extensive research surrounding one-dimensional nanomaterials such as carbon nanotubes,[5] cellulose nanocrystals,[8] and inorganic nanorods and nanowires.[9-11] More recently, the production of graphene, graphene oxide, and MXenes has sparked a resurgence of interest into the phase behavior of two dimensional (2D) nanomaterials, a field whose inception started with naturally occurring 2D nanoclays.[12-14]

In terms of liquid crystal science, MXenes are particularly fascinating because their inorganic character, charged surfaces, and high relative densities make them interesting analogs to nanoclays while their irregular shapes make them analogous to the graphene family of materials. In a little more than ten years, this family of 2D transition metal carbides, nitrides, and carbonitrides has rapidly progressed from discovery to intense excitement over their potential applications.[15-19] However, achieving the full potential of MXenes requires an improved understanding of their colloidal and liquid crystalline phase behavior. MXenes follow the formula of $M_{n+1}X_nT_x$, where M is an early transition metal, X is either carbon and/or nitrogen, n =1, 2, or 3, and T_x represents the surface termination groups, (e.g. -O, -OH, and/or -F).[20] These terminal groups on the basal plane of the MXenes aid their dispersion in aqueous solvents.[21] The first reported, and most widely studied, form of MXene is $Ti_3C_2T_x$, which has promising applications in many fields, including energy storage,[15, 16, 19] conductive and antibacterial coatings,[17, 22] and electromagnetic interface shielding.[18]

Among the outstanding properties of MXenes, the formation of liquid crystals has recently received interest.[23] Due to the structural similarities of MXenes to inorganic nanoclays, such as laponite, it was reasonably hypothesized that MXene dispersions would also exhibit rich liquid crystalline phase behaviors. The primary focus of this dissertation stems from this hypothesis with a goal to extend the original nanoclay framework to MXenes. Nanoclay literature, dating back nearly one hundred years, states that concentration, aspect ratio, and ionic strength are the primary factors affecting aqueous dispersion behavior.[24-31] To extend the nanoclay framework to MXenes, two primary questions must be answered:

- What are the effects of MXene sheet size on phase behavior and rheology?
- What are the effects of sodium chloride (NaCl) addition on phase behavior and rheology?

By answering these questions, a MXene size-dependent phase diagram and MXene-NaCl phase diagrams were developed. These are the first detailed phase diagrams for $Ti_3C_2T_x$ MXenes published in the literature, and they provide insight into the tunability of these dispersions to enhance processability in various fluid-phase manufacturing methods, such as direct-ink-writing (DIW). The alignment of advanced materials or devices produced through fluid phase processing can be improved by utilizing an assembled liquid crystalline phase, which then typically enhances the anisotropic properties of the solidified device or material. The efficiency and resolution of DIW processes are also directly correlated to associated rheological properties of the printed ink. The shear that the ink undergoes during the printing process can be imitated by steady shear rheological tests, providing insight into the printability of the ink before DIW trials. Viscoelasticity, or the relative amounts of solid-like and liquid-like behavior, is particularly important in DIW because the printed layers must both merge and support one another.

Developing phase diagrams for colloidal dispersions is of scientific merit and paves the way for impending application developments. It is known that dispersion concentration, size distribution, and electrostatic effects all influence the phase behavior of colloidal dispersions. Rheological properties, which in turn affect dispersion microstructure and processability, are directly related to the phase behavior. At the current time, there is limited fundamental understanding of MXene phase behavior and associated rheological properties. Preliminary research into the concentration threshold required for small and large MXene sheets was conducted by Zhang et al. in 2020.[23] Their work confirmed that aqueous $Ti_3C_2T_x$ MXenes could form lyotropic liquid crystalline phases and that the phase boundaries were dependent on the sheet size. While Zhang et al. initiated the investigation of size fractionated MXenes, their work primarily focused on achieving a liquid crystalline phase to spin into highly aligned additive free fibers. A deeper understanding of MXene sheet size effects on phase behavior and associated rheological properties is necessary for expanding the processability of these dispersions to a wider range of applications; the results of this dissertation will support future research in the processing of MXene dispersions into aligned materials. Through understanding the tunability of MXene dispersions by selection of sheet size, future researchers can better predict final properties of processed dispersions and more easily achieve desired results.

Salt concentration is known to affect the properties and phase behavior of colloidal dispersions; however, the outcomes of these effects are not well understood for aqueous MXene systems. The surfaces of MXene particles are negatively charged while the edges are positively charged providing face and edge interactions that can result in network formation similar to the mechanisms for nanoclays.[30] The classical Derjaguin-Landau-Verwey-Overbeek (DLVO) theory describes the interactions between charged surfaces in a liquid medium by a combination of the van der Waals attractive and electrostatic repulsive forces.[32] Interparticle interactions due to thermal motion and distribution of charge can induce the formation of various structure types. However, tuning a dispersion by pH changes or salt and/or polymer addition can also induce flocculation.[33, 34] The instability of a flocculated dispersion detracts from its processability and often results in manufactured devices with insufficient properties. Understanding how to balance concentration and ionic strength to achieve an aligned phase with desirable properties while simultaneously avoiding the induction of flocculation increases the range of applicability of such a dispersion.

In summary, this dissertation contributes to the fundamental understanding of size effects and salt concentration on lyotropic phase transitions, microstructural alignment and aggregation, and rheological properties of aqueous MXene dispersions. The knowledge gained from this work will directly contribute to the formulation of structure-property-processing relationships of aqueous $Ti_3C_2T_x$ MXene dispersions. In turn, this will increase MXene processability and performance of MXene-based devices, as well as contribute to the fundamentals of 2D colloid science. Chapter 2 includes a literature review of liquid crystals and their formation and applications, MXenes and their similarities to other 2D nanomaterials, effects of polydispersity and charged surfaces in other colloidal dispersions, and rheological signatures and properties of lyotropic phases. Chapter 3 discusses the experimental methods used throughout this work, including MXene synthesis and preparation, characterization techniques, and theoretical phase transition calculations. Chapter 4 provides a brief discussion on preliminary experimental investigations of nanowire synthesis and phase behavior to serve as a baseline for the more complex MXene work to follow. Chapter 5 discusses the size effects of MXene sheets on dispersion phase behavior and rheological properties, as well as the benefits of utilizing selective polydispersity to tune dispersions to achieve the highest processability parameters. Chapter 6 explores the effects of NaCl salt addition on the phase behavior and rheological properties of bimodal MXene dispersions. Chapter 7 summarizes the conclusions from this research and describes future applications that will directly benefit from the knowledge and understanding gained.

Chapter 2 – Background

2.1 Liquid Crystal Phase Behavior

Liquid crystals are an intriguing material phase that exhibit both the fluidity of a liquid and the crystallinity of a solid. The building blocks of these liquid crystals are rigid, anisotropic mesogens. The first noted observation of a liquid crystal dates back to 1888, when Friedrich Reinitzer believed he witnessed a material with two melting points. This material, cholesteryl benzoate, displayed characteristics of both a liquid and a solid, leading to the mesophase name of "liquid crystal."[35] Otto Lehmann extended this observation through the use of his recent invention: a hot stage polarizing microscope. Through this use of this groundbreaking technology, Lehmann witnessed a material that contained the optical properties of a crystal while maintaining the ability to flow like a liquid. This was the first noted observation of thermotropic liquid crystalline behavior, earning Lehmann the moniker of the "father" of liquid crystals.[36] However, the validity of these observations was questioned for many years.[2]

The first observation of lyotropic liquid crystallinity occurred a few decades later in the early 20th century when induced optical anisotropy of one dimensional (1D) vanadium pentoxide (V_2O_5) sols was noted by Freundlich.[37] He showed that the optical anisotropy, or birefringence, could be induced through physical preparation means and by electric fields. Freundlich compared his own experimental observations to that of the previous thermotropic liquid crystalline observations by Lehmann and others, eventually emphasizing that there were two classes of liquid crystals: thermotropic and lyotropic. Further investigations with V_2O_5 by Zöcher focused on the dependence of birefringence on flow rate, temperature, concentration, and age.[37] These experiments found that birefringence developed over time and increased linearly with increasing flow rate. Around the same timeframe, in 1922, Friedel published his seminal classification system of liquid crystals based on their positional and orientational ordering. He also noted that as liquid crystals are not true physical crystals, they should not be named similarly. He termed the phrase “mesogen” in reference to mesomorphic phases of the substances that had the ability to form liquid crystals.[38]

Observations of birefringent liquid crystalline dispersions continued throughout the next decade, in materials such as 2D nanoclays and tobacco mosaic virus (TMV), though practical applications of the materials remained scarce.[39] The theoretical knowledge of the materials progressed mainly through the use of empirical polarized microscopy of these systems. The experimental findings of TMV became inspiration for Onsager’s seminal theory of hard rod behavior in 1949 and therefore, is often seen as the prototype of a rigid rod system.[4, 40] Decades later, further investigation into the liquid crystalline behavior of TMV by Fraden et al. found that birefringence was also a function of ionic strength and polydispersity.[4, 41] This resulted in the conclusion that TMV dispersion stability was determined by electrostatic repulsion, thus adding to the parameters that influence lyotropic liquid crystal phase behavior.[4]

In the more recent decades, applications of liquid crystals have caused an increased spark of interest in the field. The introduction of liquid crystal displays in the 1970s is often considered the earliest application of broad interest, though other electronic and energy related applications have proved to be just as relevant in society.[42] Synthetic approaches have advanced the production of anisotropic materials that can form liquid crystalline phases. The most well-known of these is poly(p-phenylene terephthalamide (PPTA), which forms lyotropic liquid crystals in sulfuric acid and is the basis of high strength Kevlar® fiber. More recently, the desire to utilize anisotropic nanomaterials properties for macroscale applications has spurred a resurgence in liquid crystalline research and a branching of the science into other academic fields, including biotechnology and optics.[42]

2.1.1 Classification of Liquid Crystals

There are two overarching classes of liquid crystals, based on the controllable parameter of the material. Thermotropic liquid crystals are regulated by either temperature or pressure.[43] The liquid crystal that Friedrich Reinitzer discovered with two melting points is an example of a thermotropic liquid crystal. In this type of liquid crystal, raising the temperature of the material causes the phase to change from crystal to liquid crystal to isotropic fluid.[35] Lyotropic liquid crystals, however, are modified via dispersion concentration changes. For this class of liquid crystals, liquid crystalline behavior is seen when a specific solvent, most often water, is introduced to the system.[35, 43] Friedelian classification of liquid crystals are based on their microstructure into three groups: nematics, cholesterics, and smectics (**Figure 2.1**).[44] The ordering microstructure of the liquid crystal is the determining factor in classification. A director vector, denoted by n, is used to show the general long-range orientation of the molecules in these different mesophases. Nematic mesophases are characterized by long-range, parallel mesogen orientational order; however, there is no long-range mesogen center of position. Therefore, the mesogen are mostly aligned along the director but have no further positional order. Cholesteric mesophases display similar characteristics as nematics, though cholesterics have a twisting average molecular orientation. The molecules in this type can be separated into thin layers with each layer's director rotating slightly from the adjacent layer's order, producing a helical shape altogether. Smectic mesophases are highly stratified, meaning the molecules are arranged in layers that can slide over one another. Within these layers, there is high orientational ordering along the director and the centers of position are moderately ordered. There are several different molecular packing methods of the smectic mesophases, such as planar and hexagonal.[35, 43]

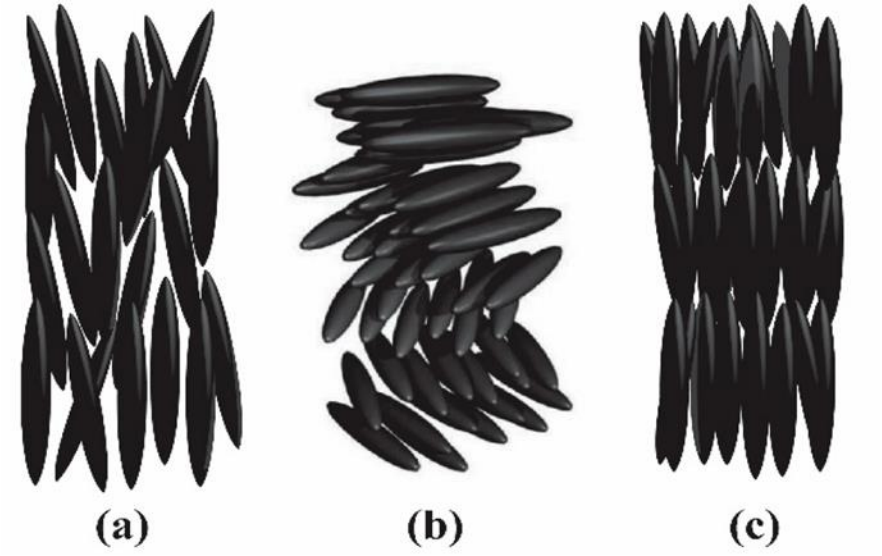

Figure 2.1. Friedelian classes of liquid crystalline ordering: a) nematic, b) cholesteric (twisted nematic structure), and c) smectic.[44] Reprinted with permission from Hamade, F.; Amit, S. K.; Woods, M. B.; Davis, V. A., The Effects of Size and Shape Dispersity on the Phase Behavior of Nanomesogen Lyotropic Liquid Crystals. *Crystals* **2020**, 10 (8), 715.

2.1.2 Fundamental Theory

Liquid crystal phase behavior is mostly described using two popular seminal theories: Onsager[40] and Flory.[45] These theories have been further advanced and expounded upon since first publications, though much of the fundamentals found in these works are the basis for many more new and evolving theories. Onsager spurred the study of rod-like molecule phase behavior with his 1949 seminal work that brought forth a mechanical and statistical based theory of dispersed rod orientation. It is important to note that while rods are classified as 1D nanomaterials, 2D nanomaterials can also be classified as "short hard rods" and thus follow the behavior of hard rods in Onsager's theory. This theory hinges on the prediction that phase behavior is entropy-driven and directly affected by excluded volume interactions. While the motion and the alignment of the rods in dispersion depend on their aspect ratio and volume fraction, it is the balance of rotational and translation entropy that causes phase changes to occur.[46] The motion of the rods is described by the rotational entropy, which reaches a maximum when there is equal probability for the rods to align in all directions. The translational entropy, however, reaches a maximum when the rods align in a single direction and resultingly maximizes the free volume of the dispersion.[47] The competition between these two entropies results in the formation of the liquid crystalline phase as the translational entropy overtakes the rotational entropy for dominance in the dispersion, and the whole system maximizes total entropy by breaking orientational symmetry and gaining a preferred directional alignment of the rods. Through the thermodynamic equation for Gibbs free energy (**Equation 2.1**) it follows that the maximization of the total entropy of the system will result in the minimization of the free energy at constant temperature and pressure.

$$\Delta G = \Delta H - T\Delta S \tag{1}$$

where ΔG is the change in Gibbs free energy, ΔH is the change in enthalpy, T is the constant temperature of the system, and ΔS is the change in total entropy, in this case both translational and rotational entropy. In Onsager's theory, free energy is modeled through a virial expansion truncated at the second virial coefficient. This truncation is considered justifiable for long, hard rods but application to 2D nanomaterials leads to higher error, resulting in the need for theory refinements as discussed further below.[6]

Figure 2.2 illustrates the general behavior of hard rods as the concentration, or volume fraction ϕ, of the rods increases. In lower concentrations, dispersions are in dilute phases in which the rods (or sheets, in the case of 2D materials) do not interact with one another. As the concentration is increased, the dispersion enters the semidilute phase where rod rotation becomes limited. Once the isotropic concentrated phase is reached, both rotational and translational motion of the rods are inhibited. Upon further increase in colloid concentration, the rotational and translational entropies compete with one another, and as a result, regions of a liquid crystalline phase form in equilibrium with the isotropic phase. This is known as the isotropic-nematic transition ϕ_I, or the biphasic region due to the presence of two competing phases. The liquid crystalline phase transition ϕ_{LC} is reached once no isotropic regions remain, resulting from thermodynamic equilibrium between orientational and positional entropies.[40]

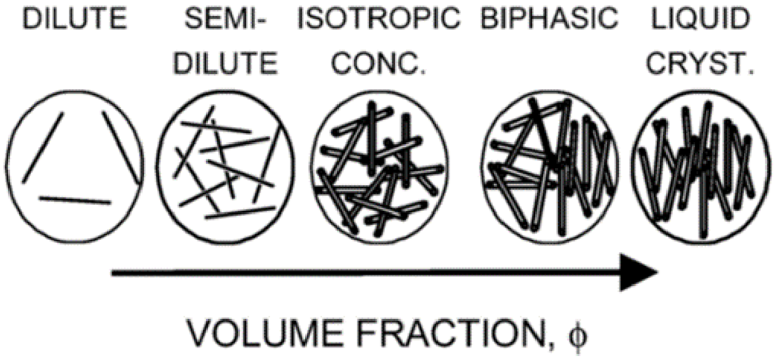

Figure 2.2. Phase behavior of Brownian rigid rods in solution.[48, 49] Reprinted with permission from Davis, V. A.; Ericson, L. M.; Parra-Vasquez, A. N. G.; Fan, H.; Wang, Y.; Prieto, V.; Longoria, J. A.; Ramesh, S.; Saini, R. K.; Kittrell, C.; Billups, W. E.; Adams, W. W.; Hauge, R. H.; Smalley, R. E.; Pasquali, M., Phase Behavior and Rheology of SWNTs in Superacids. *Macromolecules* **2004**, 37 (1), 154-160. Copyright 2004, American Chemical Society. Adapted from Doi and Edwards, 1986.

Onsager's theory can be used to calculate the theoretical critical phase transitions. Assumptions of Onsager's theory exclude the effects from attractive van der Waals forces, repulsive electrostatic forces, solute-solvent interactions, and sedimentation. This theory is also only applicable to long (L>>D) and rigid rods dispersed in an athermal solvent. Despite the restrictive assumptions of Onsager's theory, using equations from this work can provide a baseline prediction for critical phase transitions of rigid, anisotropic mesogens. Onsager's equations are as follows:[40]

$$\phi_I = \frac{3.34}{L/_D} \tag{2}$$

$$\phi_{LC} = \frac{4.49}{L/_D} \tag{3}$$

Where ϕ refers to the volume fraction (v/v) of the rods in the dispersion, *L* is the length of the rod, and *D* is the diameter of the rod. Volume fraction is the concentration measurement of choice for colloid and liquid crystal science. This is because colloids can have a range of relative densities (1 gm/cm^3 – 10 g/cm^3), especially compared to the solvents in which they are dispersed.[44] When switching between possible solvents for a single nanomaterial or comparing the behavior of different nanomaterials, the weight fraction can vary greatly. Additionally, the phase behavior is driven by volume occupied. Volume fraction of a dispersion can be calculated from the weight fraction through the following equations:

$$\phi = \frac{w\rho_{rel}}{1+(\rho_{rel}-1)w} \tag{4}$$

$$\rho_{rel} = \frac{\rho_s}{\rho_p} \tag{5}$$

where ρ_{rel} is the relative density, ρ_s is the aqueous solvent density, and ρ_p is the particle density. The dispersion concentration c can also be converted into units of mg/mL from the determined weight fraction through Eq. 6:

$$c = \frac{w}{w+(\rho_{solvent}-w\rho_{rel})} \tag{6}$$

In the decades since Onsager's work was first published, refinements and extensions have been made to broaden the scope of materials and dispersions that fit to his theory and improve the calculation of phase transitions of more complex systems.[6, 7, 50-53] These improved models, calculations, and computer simulations have provided more insight into typical phase transition behavior of 2D colloids, as well as polydispersity and electrostatic effects in a variety of colloidal systems. Numerical refinements and extensions to include nonhomogeneous systems and attractive interactions were early areas of focus.[54-57] The original theory was also notably based solely on monodisperse rods – a system that is difficult to achieve. Speranza et al.[58, 59] and Wensink et al.[53] analyzed the effects of polydisperse rod systems, including log normal distributions, and expanded the theoretical framework to include such systems. Green et al.[46] further extended the theory to include thermodynamic interactions that have resulted in rich colloidal phase behavior, specifically the short-range repulsion and long-range attraction of polydisperse Brownian rods. Flory's theory was published in 1956 as an early attempt at improving the limitations of Onsager's theory and other previous work. Flory added in a lattice model for rod location that is stated to apply to any particle orientation distribution and lift the concentration restrictions previously seen.[45] This theory results in critical concentration values that are higher than those reported earlier by Onsager due to his truncation of the virial equation and his assumption of only long and rigid rods (L>>D).[40] Flory's theory has also been improved, most popularly in the addition of the Flory Huggins Interaction parameter (χ) which allows for the inclusion of attractive interparticle interactions.[46] However, the many numerical approximations used in Flory's theory makes its quantitative applications limited.[46] While Flory theory is typically used for polymeric mesogens, materials with high aspect ratios and persistence lengths have been found to still find a better fit in Onsager's theory due to its use of infinite length and high rigidity, and the many refinements made to Onsager's theory has made it applicable to many more systems than at its original publication.

2.1.3 Properties of Liquid Crystals

Many properties of liquid crystals arise from their anisotropic structure. Anisotropic materials display different physical properties depending on which directional axis the property is measured. In liquid crystals, the macroscopic anisotropy causes them to be optically anisotropic, meaning that that the refractive index parallel to the director is different from the refractive index perpendicular to the director.[42] This changing refractive index leads to the optical property of birefringence. A liquid crystal's birefringence varies throughout the material based on the orientation of the director. Optically, this creates light and dark areas, or domains, in the liquid crystal, which can then be used to identify liquid crystalline phase textures and to estimate phase transition concentrations.[43, 60] Birefringence can be detected via polarized optical microscopy (POM). The material sample is placed between two crossed polarizers, or optical filters, as seen in **Figure 2.3**. As the light passes through the first cross-polarizer, it becomes linearly polarized, and then becomes elliptically polarized as it passes through the sample material. The light can take one of two paths: ordinary rays or extraordinary rays, depending on whether it is perpendicular or parallel to the director. When the light passes through the second polarizer, it now has a component that can pass through it. The intensity of this transmitted light causes the light and dark domains to appear, depending on the angle of the analyzer with respect to the polarizer. When the liquid crystal sample or the microscope stage is rotated, the domains switch between light and dark. The birefringence of the liquid crystal can be determined through the change in refractive indices:

$$\Delta n = n_e - n_o \tag{7}$$

where n_e is the refractive index of the extraordinary axis and n_o is the refractive index of the ordinary axis of rodlike polymers.[61] The color patterns of the liquid crystalline textures observed with POM are also affected by the thickness of the material sample. The Michel-Levy chart (**Figure 2.4**) can be used to determine birefringence based on sample thickness and interference order.[62]

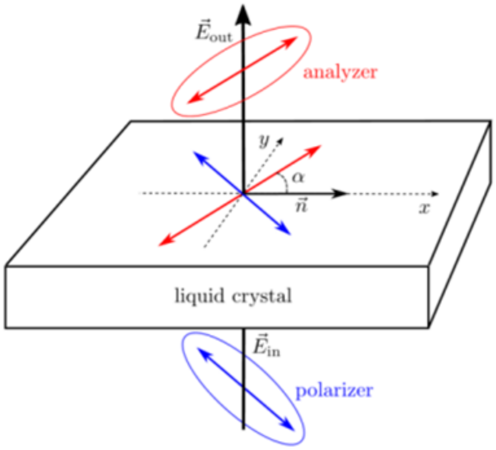

Figure 2.3. Illustration of the cross-polarizers used to capture birefringence.[43] Reprinted from Andrienko, D., Introduction to liquid crystals. *Journal of Molecular Liquids* **2018**, 267, 520-541, with permission from Elsevier.

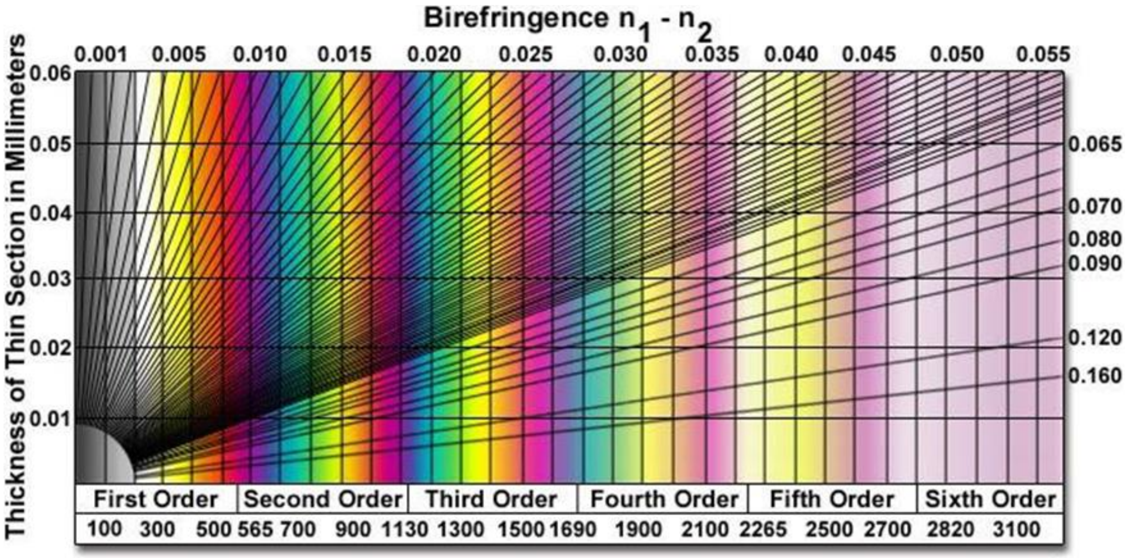

Figure 2.4. The Michel-Levy chart depicting the relationship between birefringence, liquid crystal sample thickness, and interference order.[62]

Liquid crystals also have unique rheological behavior and specific rheological signatures, making rheology a leading method in the detection of liquid crystals. A liquid crystal's rheological behavior depends on its molecular orientation in regards to the flow direction.[63] The rheological behavior of many liquid crystals follows the flow curve of a "three region behavior", as first described by Onogi and Asada in lyotropic polymer liquid crystals (**Figure 2.5**).[64] Region I and

Region III both exhibit shear thinning viscosity behavior, which means the fluid's viscosity decreases with increasing applied shear rate. Region II, however, exhibits a plateau in the fluid's viscosity. In this region, as the shear rate increases, the viscosity remains at a steady value, producing the flat horizontal line seen in the flow curve. This three region behavior occurs due to changes in dispersion microstructure at varying shear rates. In the low shear region (Region I), the shear-thinning behavior is typically attributed to tumbling behavior or the rods or sheets. In Region II, where the viscosity plateaus, the rods or sheets are likely exhibiting wagging-behavior.[49, 64] At the high shear rates of Region III, the rods or sheets align with the flow direction, resulting in shear-thinning behavior once again.[65] Other rheological signatures that are also widely useful in detecting the existence of a liquid crystal include the following:[64]

- A maximum and minimum on viscosity versus concentration curves
- A change in sign from positive to negative and back to positive for the 1st normal stress difference (N_1)
- The Cox-Merz rule is not obeyed
- In transient shearing tests, shear stress and N_1 oscillate over ~100 shear units before reaching steady state

It should be noted that these rheological signatures are a result of studies focused mainly on nematic liquid crystals.[9]

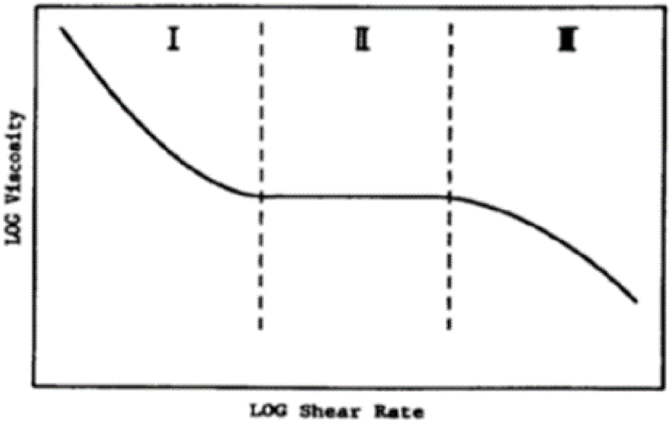

Figure 2.5 Three-region flow behavior, changing from shear-thinning (Region 1) to Newtonian plateau (Region 2) to shear-thinning (Region 3).[64] Reprinted with permission from Onogi, S.; Asada, T., Rheology and Rheo-Optics of Polymer Liquid Crystals. In *Rheology: Volume 1: Principles*, Astarita, G.; Marrucci, G.; Nicolais, L., Eds. Springer US: Boston, MA, 1980; pp 127-147.

The presence of a maximum and minimum on a viscosity versus concentration curve is often detected in liquid crystalline dispersions and used to determine the transition into the liquid crystalline phase (**Figure 2.6a,b**).[49, 66] This phenomena occurs due to change in motion of the mesogens with increasing concentration. In the isotropic phase and predominately isotropic biphasic regions, the hard rods or sheets lose rotational and translational mobility as concentration increases. This loss of mobility causes the viscosity to increase with increasing volume fraction in the isotropic phase and early biphasic region. The dispersion viscosity will then decrease as liquid crystalline regions supersede that of isotropic phase due to the alignment reducing resistance to flow. When the dispersion becomes fully liquid crystalline, the viscosity reaches a local minimum. Viscosity begins to increase once again after the transition into the liquid crystal phase as resistance to flow heightens with increasing concentration, up into a liquid crystalline gel phase. However, it should be noted that there have been reported cases of liquid crystalline dispersions not following this non-monotonic viscosity trend. This is particularly true for charged mesogens, such as sulfated cellulose nanocrystals (**Figure 2.6c**).[67]

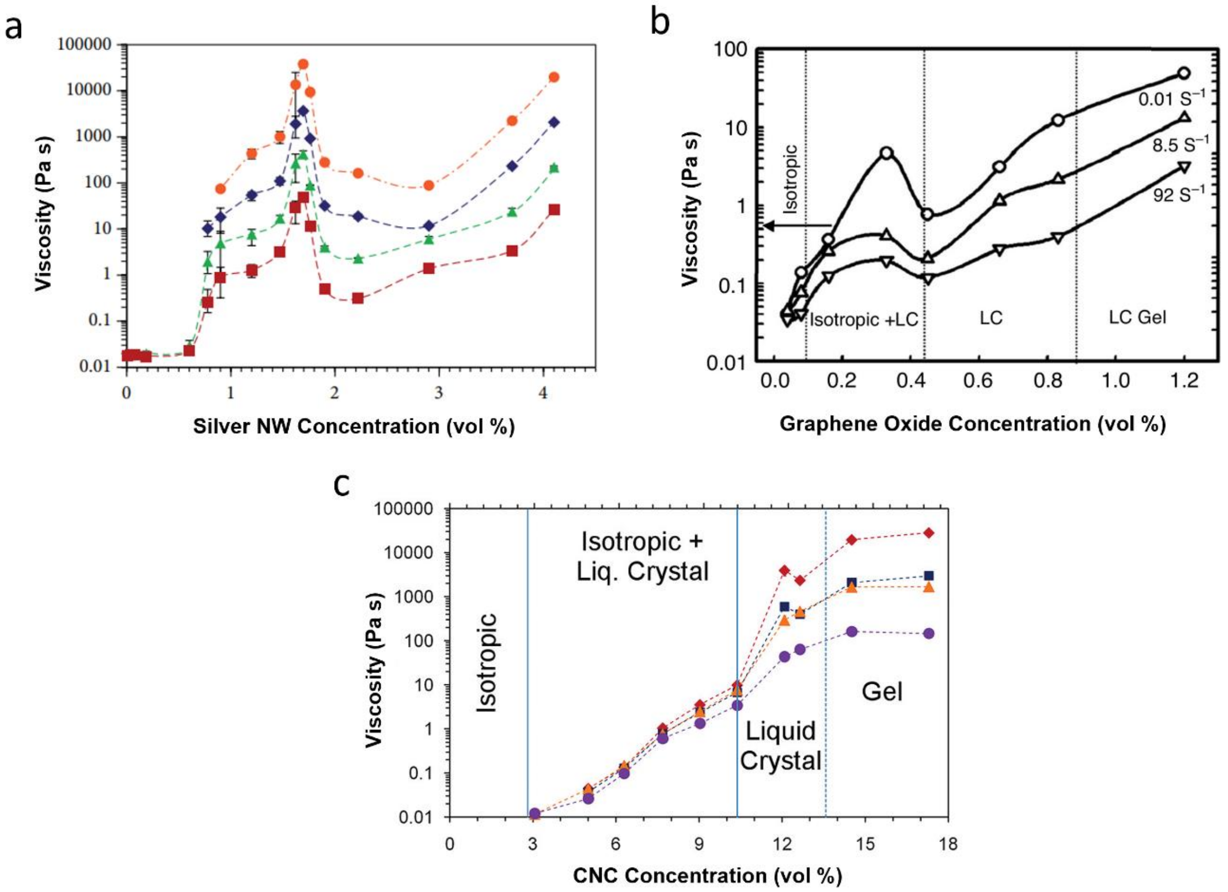

Figure 2.6. Examples of non-monotonic shear viscosity as a function of colloid concentration in a) silver nanowire dispersions[68] (Reprinted with permission from Xu, T.; Davis, V. A., Rheology and Shear-Induced Textures of Silver Nanowire Lyotropic Liquid Crystals. *Journal of Nanomaterials*, **2015**, 939587.) and b) GO dispersions.[66] Reprinted from Kumar, P.; Maiti, U. N.; Lee, K. E.; Kim, S. O., Rheological properties of graphene oxide liquid crystal. *Carbon* **2014**, 80, 453-461, with permission from Elsevier. c) Relationship of shear viscosity as a function of CNC concentration.[67] Reprinted with permission from Ureña-Benavides, E. E.; Ao, G.; Davis, V. A.; Kitchens, C. L., Rheology and Phase Behavior of Lyotropic Cellulose Nanocrystal Suspensions. *Macromolecules* **2011**, 44 (22), 8990-8998. Copyright 2011 American Chemical Society

2.2 MXenes

MXenes are a large family of 2D materials consisting of carbides, nitrides, or carbonitrides of transition metals that were discovered just over ten years ago through the process of exfoliation of ceramic materials known as MAX-phases. This has since spurred the synthesis of dozens of different MXene compositions, and even more are theoretically predicted.[69] The microstructure of MXenes, seen in **Figure 2.7**, follows the formula of $M_{n+1}X_nT_x$ where M is an early transition metal, X is either carbon or nitrogen, n is the number of X layers (between 1-4), and T_x represents the surface terminations (typically O, OH, Cl, and/or F) bonded to the outer M layers.[69] These terminal groups on the basal plane of the MXenes aide in their dispersion in aqueous solvents.[21]

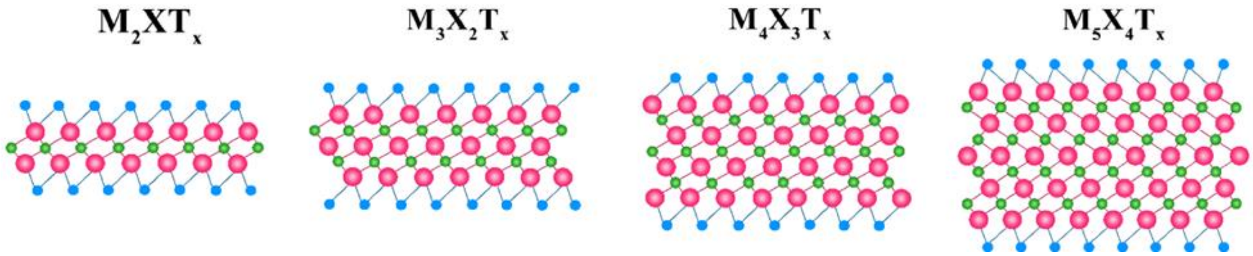

Figure 2.7. Four possible configurations of MXene structure, with n = 1-4.[70] Reprinted with permission from Pogorielov, M.; Smyrnova, K.; Kyrylenko, S.; Gogotsi, O.; Zahorodna, V.; Pogrebnjak, A., MXenes - A New Class of Two-Dimensional Materials: Structure, Properties and Potential Applications. *Nanomaterials* **2021**, 11 (12), 3412.

The first reported and most widely studied form of MXene is $Ti_3C_2T_x$, which has promising applications in many fields, including energy storage,[15, 16, 19] conductive and antibacterial coatings,[17, 22] and electromagnetic interface shielding.[18] $Ti_3C_2T_x$ MXenes are synthesized through a selective etching process of a parental MAX phase, Ti_3AlC_2.[71] Hydrofluoric acid[71] or a combination of hydrochloric acid and lithium fluoride[16] is used to remove the aluminum atoms between the individual Ti_3C_2 layers, resulting in exfoliated sheets. Both of these etching methods result in significant size polydispersity with lateral dimensions ranging from nanometers to microns.[72] Polydispersity is also seen in other 2D colloidal materials, including graphene, GO, and laponite clay.[73-75] In addition to polydispersity, the structure of MXenes is analogous to that of many nanoclays. The exfoliated MXene sheets have negatively charged faces and positively charged edges. This allows for face and edge interactions among the dispersed sheets that can result in the formation of networks similar to that found in various nanoclays.[30, 76] The charged surfaces of MXenes result in complex interactions that are only heightened by the irregular shapes and polydisperse nature of MXene sheets.

MXenes are exciting through their excellent electrical, electrochemical, and thermal properties, making it an ideal material for a range of practical applications, most notably those in electronics and energy storage.[69, 77, 78] Properties that surpass those of other 2D materials, as well as improved synthesis methods, have contributed to the increase of excitement and research on MXenes and their potential applications, such as micro-supercapacitors, sensors, and biomedical devices.[20, 79-83] Akuzum et al.[84] developed processability charts for multi-layer and single-layer MXene sheets through analysis of rheological properties under specified conditions (**Figure 2.8**). Though these results provided insight into processing for various applications, the results were restricted to a specific type of MXene, synthesis method, and sheet size. Achieving the full potential of MXenes requires an improved understanding of their colloidal and liquid crystalline phase behavior.

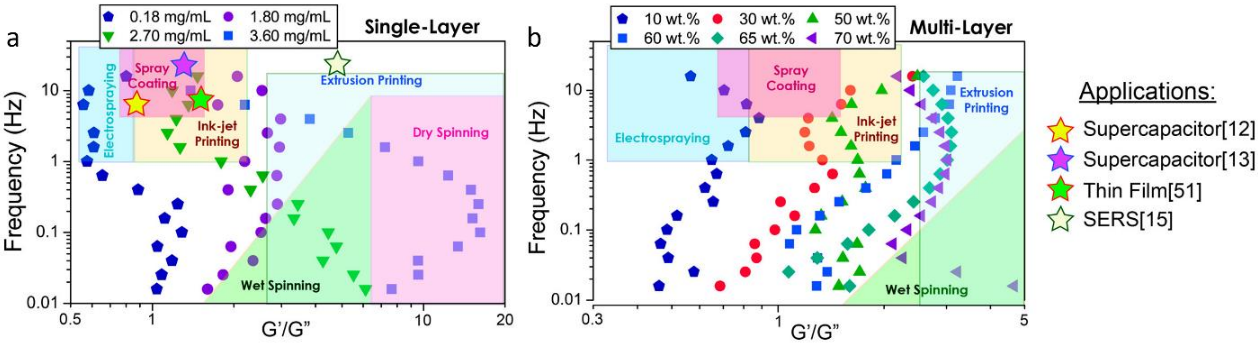

Figure 2.8. Processability charts for a) single-layer and b) multilayer MXenes based on oscillatory rheological properties.[84] Reprinted with permission from Akuzum, B.; Maleski, K.; Anasori, B.; Lelyukh, P.; Alvarez, N. J.; Kumbur, E. C.; Gogotsi, Y., Rheological Characteristics of 2D Titanium Carbide (MXene) Dispersions: A Guide for Processing MXenes. *ACS Nano* **2018**, 12 (3), 2685-2694. Copyright 2018 American Chemical Society.

Recently, Zhang et al.[23] confirmed that aqueous $Ti_3C_2T_x$ could form lyotropic liquid crystalline phases without the use of additives and that the phase boundaries were dependent on the sheet size. **Figure 2.9a** depicts the relationship of MXene lateral sheet size to phase transitions, with the two stars in the diagram indicating the concentration at which the large MXenes and the small MXenes transitioned into the nematic phase. As expected from Onsager's theory, it was found that larger MXene sheets (~3 μm, red star on diagram) required a lower concentration to form aligned nematic liquid crystals than small MXene sheets (~0.3 μm, black star on diagram). Cross-polarized microscopy was used to observe microstructural changes in the large and small MXene dispersions as concentration was increased (**Figure 2.9b**). The nematic phase was confirmed at ~13.2 mg mL^{-1} for large MXenes and 66.3 mg mL^{-1} for small MXenes by the presence of schlieren textures in these cross-polarized images. The liquid crystalline phase dispersions could then be spun into highly aligned additive free fibers through the fluid-phase process of wet-spinning. The fiber properties could be tuned through tailoring MXene dispersion properties, highlighting the practicality of tuning dispersions on the nano- or micro-scale to enhance macroscale performance.

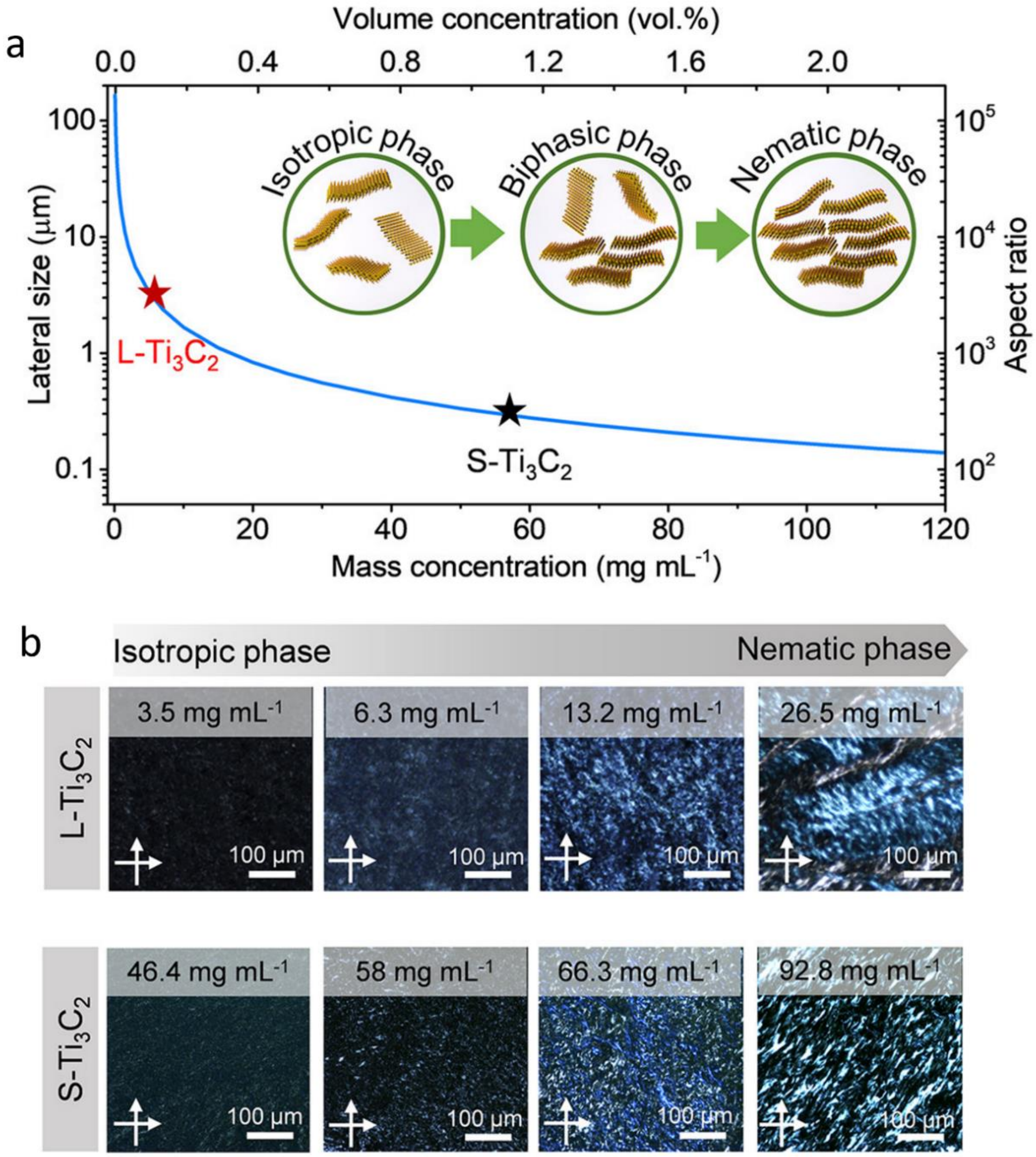

Figure 2.9. a) Relationship between the MXene dispersion concentration and MXene sheet size for liquid crystal phase transition according to theoretical calculations. b) Polarized optical microscopy images of large and small MXene sheets dispersed in water at varying concentrations to depict the transition into a nematic liquid crystal.[23] Reprinted with permission from Zhang, J.; Uzun, S.; Seyedin, S.; Lynch, P. A.; Akuzum, B.; Wang, Z.; Qin, S.; Alhabeb, M.; Shuck, C. E.; Lei, W.; Kumbur, E. C.; Yang, W.; Wang, X.; Dion, G.; Razal, J. M.; Gogotsi, Y., Additive-Free MXene Liquid Crystals and Fibers. *ACS Central Science* **2020**, 6 (2), 254-265. Copyright 2020 American Chemical Society.

2.3 Other Anisotropic Nanomaterials

2.3.1 Nanoclays

The field of 2D nanomaterials began with the study of nanoclays, dating back to the early 1900s when Langmuir reported the phase behavior of "California Bentonite."[29] Other types of nanoclays that have been studied include laponite, gibbsite, and bentonite. Most nanoclays have a plate-like structure, though terminology related to their structure can also include disc-like and sheet-like. Nanoclays have charged surfaces that contribute to their complex phase behavior that include disordered states, such as fluids, gels, and glasses, that can also interfere with the formation of ordered states such as liquid crystals.[85]

Due to the overarching similarities in structures across 2D nanomaterials, the knowledge of nanoclay structural formation and behavior provides a framework that can be extended to much of the rest of the field. Most nanoclays are layered mineral silicates built up of nano-sized sheets held together by attractive van der Waals forces.[86] Using laponite as an example (**Figure 2.10**), this nanoclay consists of two parallel sheets of tetrahedrally coordinated silica between which is an octahedrally coordinated magnesium oxide sheet.[85] Referring back to **Figure 2.7**, the structural similarities between laponite and MXenes are striking.

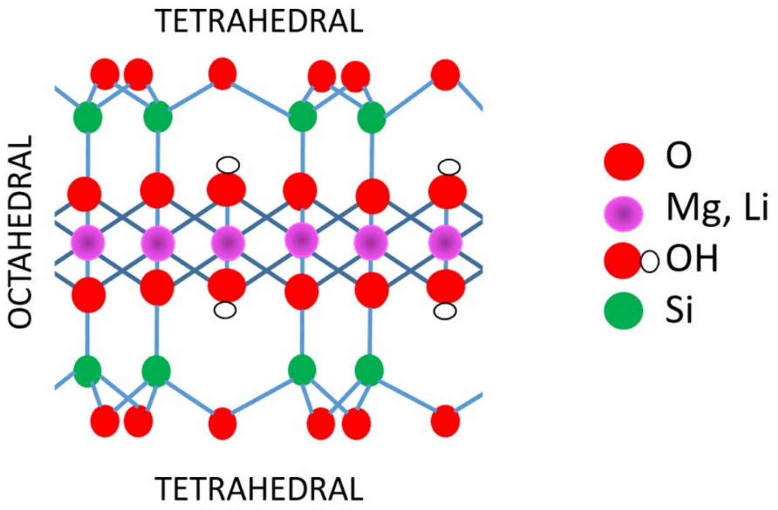

Figure 2.10. Structure of laponite nanoclay.[87] Reprinted from Tomás, H.; Alves, C. S.; Rodrigues, J., Laponite®: A key nanoplatform for biomedical applications? *Nanomedicine: Nanotechnology, Biology and Medicine* **2018**, 14 (7), 2407-2420, with permission from Elsevier.

Dispersions of nanoclays have been reported to form various associated structures due to the face and edge interactions of their charged surfaces. The charge distribution across the surface of a nanoclay and its thermal motion contributes to whether a dispersed phase is achieved or if flocculated or aggregated structures form. Throughout the literature, there is some discrepancy surrounding the definition of flocs and aggregates. Often, aggregates are considered closely packed agglomeration of mesogens, typically resulting from face-face interactions, that cannot readily be broken from applied shear.[88] Flocs, however, can be easily broken due to their more loosely connected structure formed face-edge and edge-edge interactions,.[88, 89]Flocs or aggregates can form from interactions between the clay particles, such as face-face interactions, edge-edge interactions, or face-edge interactions (**Figure 2.11**).[88] Dilute nanoclay dispersions typically do not flocculate or aggregate, due to the diffuse double layers around their charged surfaces. However, flocculation has been found be readily induced by pH changes and the addition of salts or polymers in nanoclay dispersions as well as in biological materials.[85, 90, 91] Once an additional substance is added to the dispersion, the particles may approach one another until flocculation begins. The concentration of salt or electrolyte at which flocculation is induced is known as the critical flocculation value.[88]

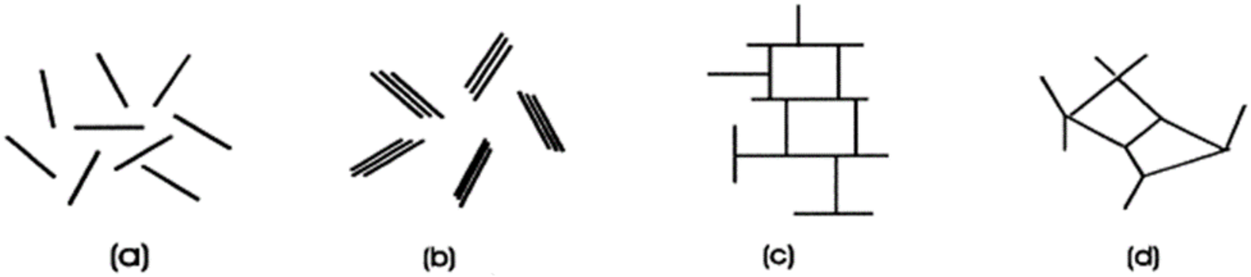

Figure 2.11. Particle association in nanoclay suspension, showing a) a fully dispersed state, b) face-face interactions, c) face-edge interactions, and d) edge-edge interactions.[88] Reprinted from Luckham, P. F.; Rossi, S., The colloidal and rheological properties of bentonite suspensions. *Advances in Colloid and Interface Science* **1999**, 82 (1), 43-92., with permission from Elsevier.

Nanoclay dispersions also exhibit lyotropic liquid crystalline phase behavior. The charged surfaces of many nanoclays result in a rich phase behavior with the formation of aligned phases as well as gel-like arrested states that are influenced by both nanoclay concentration and electrolyte addition. Gibbsite has been observed to form both columnar and nematic liquid crystalline phases, depending on the ionic strength of the suspension (**Figure 2.12a**).[92] At higher gibbsite concentrations, a gel phase was established, though notably the gel-phase boundary line was of opposite slope compared to prior studies of nanoclay suspensions, such as bentonite (**Figure 2.12b**). Gibbsite suspensions of higher ionic strengths required greater nanoclay concentration to form a gel, likely due to dominating repulsive interparticle interactions.[92]

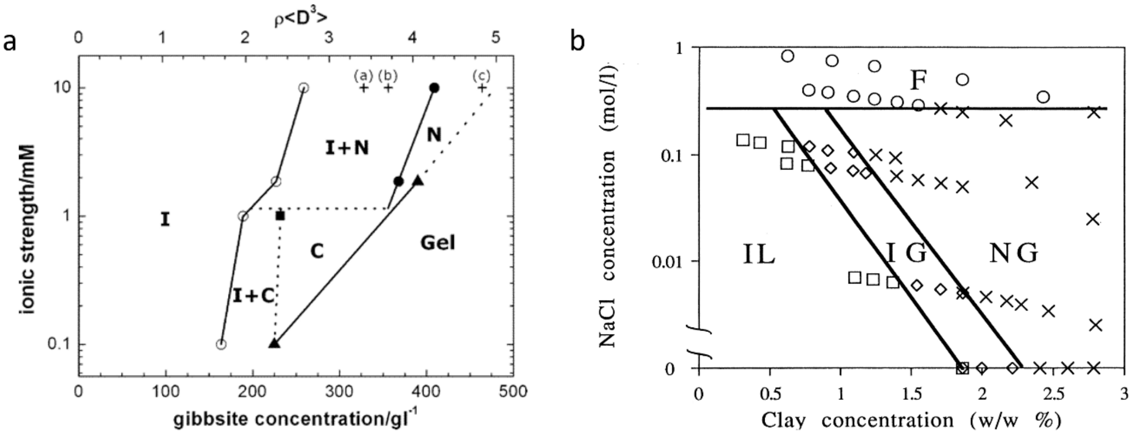

Figure 2.12. Phase diagram for a) gibbsite[92] (Reprinted with permission from van der Beek, D.; Lekkerkerker, H. N., Liquid crystal phases of charged colloidal platelets. *Langmuir* **2004**, 20 (20), 8582-8586. Copyright 2004 American Chemical Society) and b) bentonite[28] (Reprinted with permission from Gabriel, J.-C. P.; Sanchez, C.; Davidson, P., Observation of Nematic Liquid-Crystal Textures in Aqueous Gels of Smectite Clays. *The Journal of Physical Chemistry* **1996**, 100, 11139-11143. Copyright 1996 American Chemical Society) with legends following I/IL-isotropic liquid, C-columnar, N-nematic, IG-isotropic gel, NG-nematic gel, and F-flocculation.

Despite early experimental work dating back decades, there remains ongoing debate of the phase behavior of laponite dispersions; thus, emphasizing the complexity of elucidating colloidal dispersion phase behavior. According to early research by Mourchid et al., laponite formed both isotropic and nematic gel phases at relatively low concentrations, and regardless of nanoclay concentration, flocculated at sufficiently high ionic strengths (**Figure 2.13a**).[93] However, there have been differing reports of phase behavior for laponite and discussion of gel versus glass phases, causing confusion throughout the field. Ruzicka and Zaccarelli reviewed both experimental and theoretical works investigating laponite phase behavior to bring clarity to the opposing results.[85] It was found that a more unified phase diagram could be established if sample aging and preparation was more carefully taken into account for experimental results. By extensively comparing experimental results from a variety of prior work and theoretical results from simulations run by Ruzicka, an improved phase diagram was developed (**Figure 2.13b**). This diagram states that gels are formed at low laponite concentrations and glasses formed at higher laponite concentrations, with phase separation, or flocculation, occurring with increasing salt addition.[85] However, it should be noted that there remains some disagreement in the field over the definitions of attractive and repulsive-dominated phases.

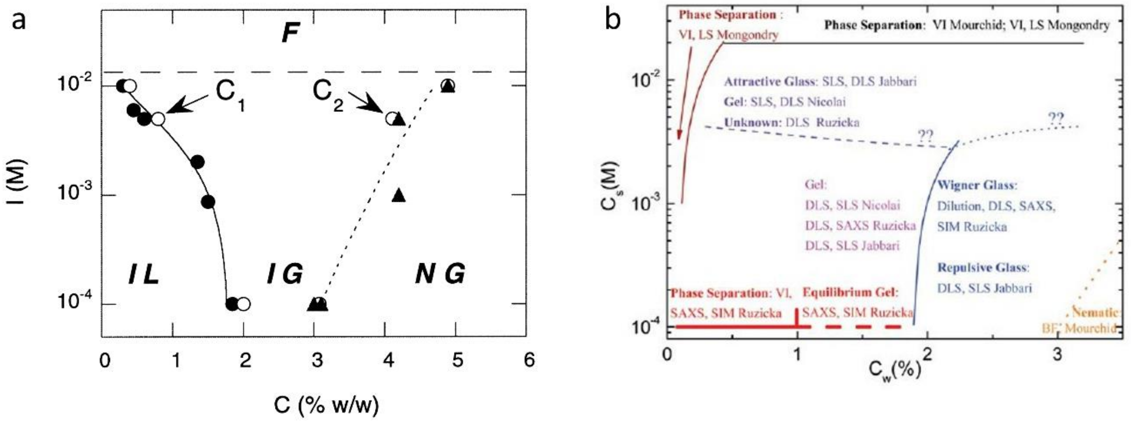

Figure 2.13. a) Early laponite phase diagram proposed by Mourchid et al., where IL-isotropic liquid, IG-isotropic gel, NG-nematic gel, and F-flocculation.[93] Reprinted with permission from Mourchid, A.; Lécolier, E.; Van Damme, H.; Levitz, P., On Viscoelastic, Birefringent, and Swelling Properties of Laponite Clay Suspensions: Revisited Phase Diagram. *Langmuir* **1998**, 14 (17), 4718-4723. Copyright 1998 American Chemical Society. B) Proposed phase diagram of laponite suspensions by Ruzicka and Zaccarelli, taking into consideration attractive versus repulsive states.[85] Reprinted from Ruzicka, B.; Zaccarelli, E., A fresh look at the Laponite phase diagram. *Soft Matter* **2011**, 7 (4), 1268-1286, with permission from Royal Society of Chemistry.

Despite the long history of nanoclay phase behavior research, deeper fundamental understanding in 2D colloidal science is necessary to maintain progress in the field and continue advancing 2D nanomaterial applications. Studying the individual phase diagrams of various nanoclays produced thus far has not resulted in a unifying method to predict the phase behavior of 2D materials. The added complexity of electrostatic interactions, irregular shape, size polydispersity, and density ranges of many 2D colloids complicates the ability to gain a comprehensive method of phase predictability. Extending the knowledge of 2D colloid behavior by continuing to investigate new complex materials through experimental methods will contribute to a broader understanding of behavior similarities and advance theoretical predictions.

2.3.2 Graphene and Graphene Oxide

Graphene is a carbon-based 2D nanomaterial, in which single-layer atoms are ordered in hexagonal, honeycomb-like lattices (**Figure 2.14a**). Due to the excellent properties of graphene, including high electrical and thermal conductivity (10^4-10^5 S/m and 3000 W/(m K), respectively),[94] it is utilized in applications such as sensors, solar cells, and supercapacitors.[95-97] Graphene can be produced from the three-dimensional (3D) material graphite through various processes, such as micromechanical cleavage and liquid-phase exfoliation.[98, 99] The first use of liquid-phase exfoliation to produce graphene by Hernandez et al. in 2008 changed the future of 2D material production from bulk material.[100] This process dispersed graphite in organic solvents, resulting in a large-scale exfoliation process with the ability to mass produce graphene for the first time.[99] Intercalation-based exfoliation can also be used to produce graphene and other 2D materials, such as MXenes.[78, 100] Intercalating graphite with acids and exfoliating through sonication yields solution-based graphene oxide (GO). GO is predominantly monolayer nanosheets ranging in size from 50-100 µm, though depending on synthesis conditions, these sheets can bear a variety of functional groups (**Figure 2.14b**).[100] In some applications, the functional groups can be beneficial, such as aiding in water solubility. The functional groups can be removed through chemical, electrochemical, or thermal reduction methods to produce reduced graphene oxide (rGO). The carbon structure of this material includes defects from the reduction process, resulting in a material that is not pristine like graphene and GO (**Figure 2.14c**).[100]

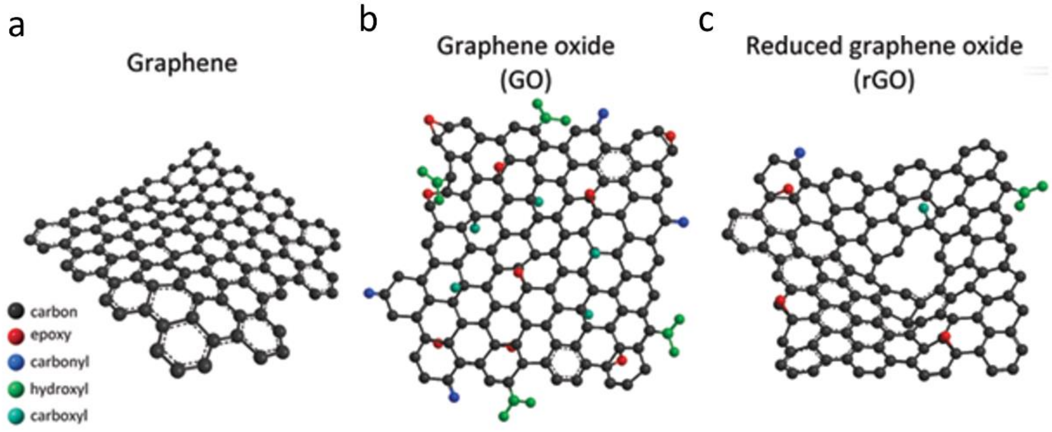

Figure 2.14. Molecular structures of a) graphene, b) graphene oxide, and c) reduced graphene oxide.[101] Reprinted and adpated with permission from Amieva, E. J. C.; Lopez-Barroso, J.; Martínez-Hernández, A. L.; Velasco-Santos, C. In *Graphene-Based Materials Functionalization with Natural Polymeric Biomolecules*, **2016**.

Due to the anisotropic structure of graphene and its derivatives, they are able to form lyotropic liquid crystalline phases. GO is the most widely studied member of the graphene family in terms of liquid crystal science. The self-assembly of GO in liquid crystalline phases allows for *in situ* fabrication of highly complex GO structures.[14] These structures, as well as associated properties, are dependent on interactions between GO sheets. The repulsive forces between the sheets result in steric hindrance that limits the distance to which the sheets can approach each other. As in all colloidal dispersions, excluded volume effects play a pivotal role in the self-assembly of GO. Larger GO sheets consist of higher excluded volumes than smaller GO sheets, which led to the hypothesis that size fractionated GO sheets will behave differently. Jalili et al. studied the difference in liquid crystalline phase behavior between ultra-large GO sheets and smaller GO sheets, depicted in **Figure 2.15**.[14] Due to the large excluded volume of ultra-large GO sheets, the sheets had to orientate themselves parallel to one another to minimize volume excluded and maximize packing alignment. In accordance with Onsager theory, this ordering of the ultra-large GO sheets resulted in nematic ordering.[14] The small GO sheets have such small excluded volumes that ordering of the sheets was not required to maximize packing of the sheets. Therefore, small GO sheets remained in an isotropic phase regardless of concentration. Extending this investigation to mixing large and small GO sheets at selective amounts resulted in a proposed mechanism to systematically manipulate a GO dispersion into a liquid crystalline phase to enhance processability with increased tunable parameters.[14]

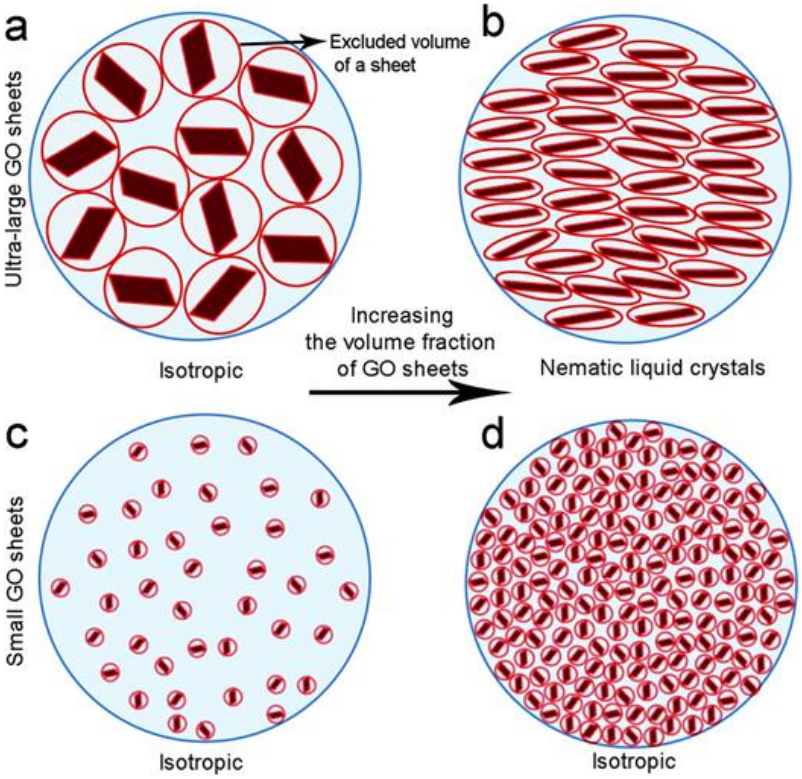

Figure 2.15. Evolution of liquid crystal phases in GO dispersions upon increasing concentration with a,b) ultra-large GO sheets and c,d) small GO sheets.[14] Reprinted from Jalili, R.; Aboutalebi, S. H.; Esrafilzadeh, D.; Konstantinov, K.; Razal, J. M.; Moulton, S. E.; Wallace, G. G., Formation and Processability of Liquid Crystalline Dispersions of Graphene Oxide. *Materials Horizons* **2014**, 1 (1), 87-91, with permission from the Royal Society of Chemistry.

Naficy et al. extended ultra-large GO research by relating liquid crystalline phase formation to changes in rheological properties and microstructure upon increases in concentration.[102] In accordance with theory, Jalili et al. showed low concentrations of ultra-large GO rotated and translated freely in an isotropic phase, with rheological properties indicating liquid-like behavior

(G''>G'), seen in **Figure 2.16a**. Increasing the concentration of GO induced some nematic ordering, as observed in the appearance of microstructure in the microscopy images of **Figure 2.16b,c**, as well as G' becoming larger than G''. These changes indicated a transition into the biphasic region. **Figure 2.16d** depicts a single nematic liquid crystalline phase. Upon increasing GO concentration further, the nematic phase underwent higher packing of the sheets and resulted in nearly plateaued viscoelastic properties (**Figure 2.16e**). In addition to extended nematic alignment, long-range positional order was achieved in some parts of the GO dispersion in **Figure 2.16f**, indicating that a full nematic liquid crystal had been achieved. Increasing GO further beyond this concentration resulted in the formation of smaller monodomains with large increases in G' (**Figure 2.16g,h**).[102] The insight from Naficy et al.'s research increased the fundamental understanding of 2D materials as well as the tunability of those materials to enhance processability according to what technique or method is to be used.

2.3.3 Manganese Dioxide Nanowires

Manganese dioxide (MnO_2) is a metal oxide that can be synthesized to produce multiple 1D morphologies. It has an atomic structure of octahedron units of MnO_6 that can be linked together in various ways to produce these multiple morphologies as well as different crystallographic forms. The synthesis of MnO_2 used in this work was facile with quick precipitation at relatively low temperature and short reaction time. The use of two solvents in the synthesis provided more tunability to achieve the differing forms. The ratio of the two solvents used, deionized water and isopropanol, was altered to produce different morphologies. H_2O molecules bind to the O atom of the octahedral MnO_6 units more so than the isopropanol molecules, and so, it is the amount of H_2O molecules available that affects the crystal growth of

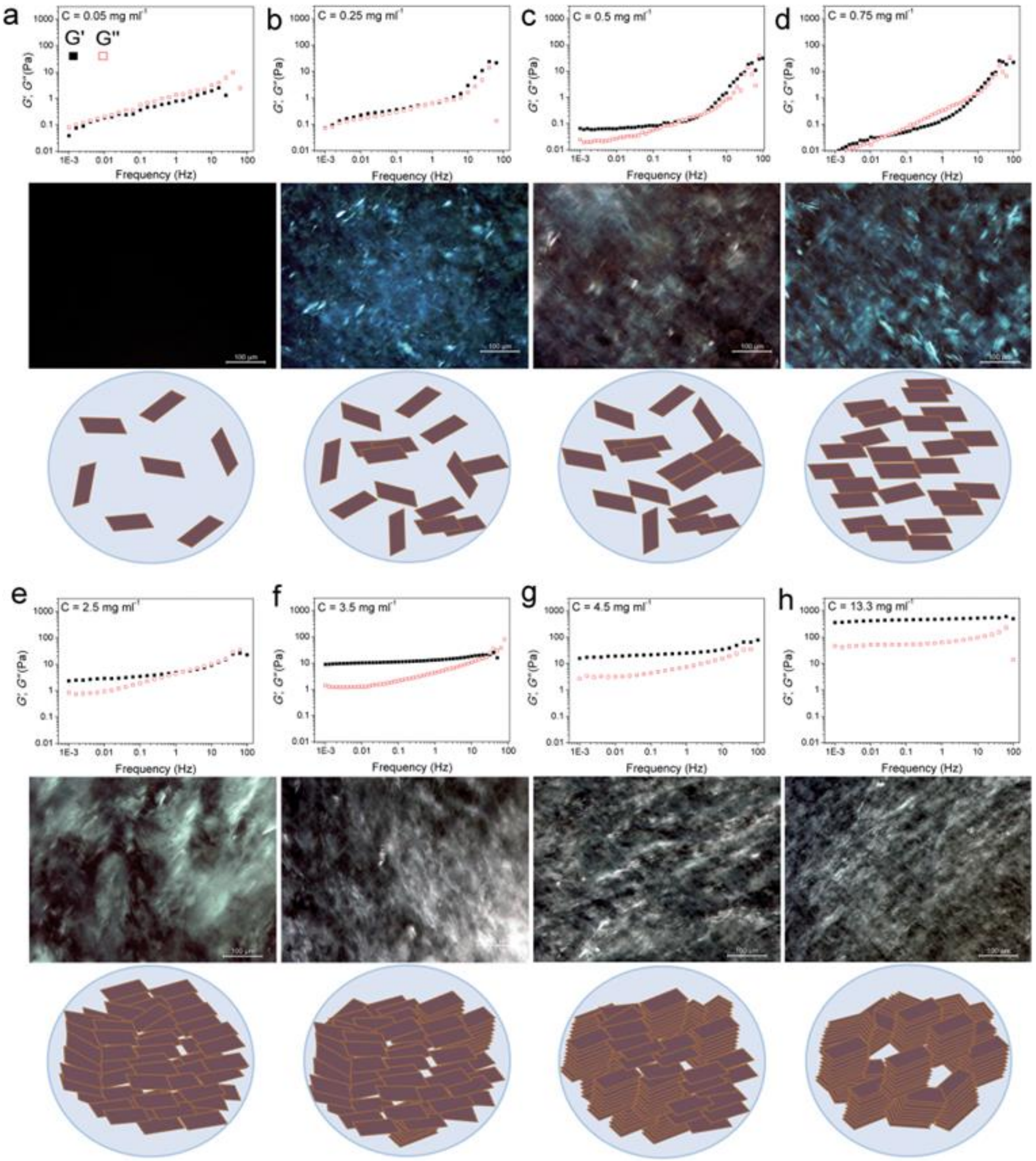

Figure 2.16. Schematic depicting the relationship between viscoelastic properties (G' – storage modulus and G'' – loss modulus), microstructural alignment, and dispersion concentrations for ultra-large GO dispersed in water.[102] Reprinted from Naficy, S.; Jalili, R.; Aboutalebi, S. H.; Gorkin Iii, R. A.; Konstantinov, K.; Innis, P. C.; Spinks, G. M.; Poulin, P.; Wallace, G. G., Graphene oxide dispersions: tuning rheology to enable fabrication. *Materials Horizons* **2014**, 1 (3), 326-331, with permission from the Royal Society of Chemistry.

the MnO_2. When the ratio of DI water to isopropanol is kept low at 1:10, there are fewer H_2O molecules in the reaction. This minimizes the binding to only the most energetic faces, which are those along the (001) direction. From this, unidirectional growth resulted, thus producing only rod- and needle-like morphologies. In order to obtain a spindle-like morphology, that ratio would need to be increased to 2:5. In this case, there are more H_2O molecules available in the reaction, so crystal growth can occur in more directions than the one.[103] **Figure 2.17** illustrates the formation mechanism for the different morphologies. In this work, the rod- or wire-like morphology was desired due to the higher aspect ratio that it provides.

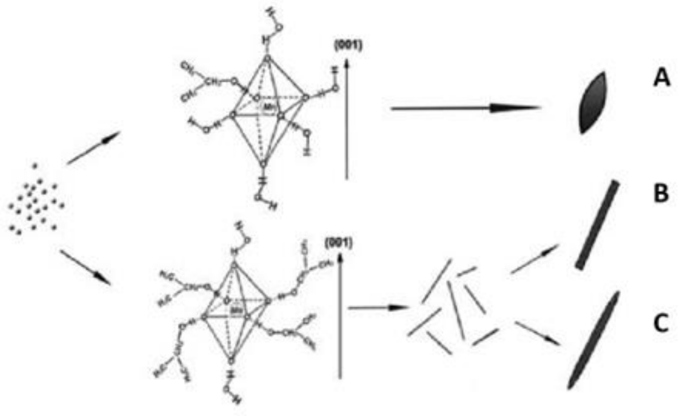

Figure 2.17 Formation mechanism of the different MnO_2 morphologies: A) spindle-like B) rod-like and C) needle-like. Reprinted from Chen, S.; Zhu, J.; Han, Q.; Zheng, Z.; Yang, Y.; Wang, X., Shape-Controlled Synthesis of One-Dimensional MnO_2 via a Facile Quick-Precipitation Procedure and its Electrochemical Properties. *Crystal Growth & Design* **2009**, 9. Copyright 2009 American Chemical Society.

2.3.3 Metal Nanowires

Silver is the most conductive element, which theoretically makes it an excellent choice to use in many electrical applications; however, its high cost detracts from the feasibility of using silver in many applications. Copper is over 1000 times more abundant than silver, though only 6% less conductive. Because of these properties, copper has become a popular element of choice in new electrical applications and developments.[104] Copper nanowires (Cu NWs) have been explored as low-cost alternatives to silver nanowires and indium tin oxide (ITO) in applications such as forming water-based films for transparent electrodes.[105]

In order to make Cu NWs a better alternative to more expensive materials, a better understanding of their synthesis and growth mechanisms was necessary. High quality Cu NWs were first produced in large-scale quantities by Chang et al. in 2005.[106] In 2016, Ye et al. achieved the first direct measurement of Cu NW growth kinetics in solution through visualization.[104] Up until that point, the growth process of Cu NWs was not well understood. By understanding the growth mechanism to a greater degree, better control over their structure could be achieved and tunability could be enhanced. From their work, a greater understanding of nanowire growth could be applied to various nanowire syntheses.[104] This provides evidence that by gaining a deeper understanding of a specific colloid and its tunability, the increased knowledge can be extended to the overarching field of colloid science.

2.4 Applications of Anisotropic Nanomaterials

The ability for many anisotropic nanomaterials to readily form lyotropic liquid crystalline phases has long since enabled their use in a variety of fluid-phase manufacturing techniques, such as direct-ink-writing and fiber spinning (**Figure 2.18**). The aligned phases of liquid crystals can facilitate the production of advanced materials with anisotropic properties.[2] It is well understood that the properties of the initial dispersion directly impacts the macroscale properties and performance of manufactured devices. Recent progress in the field includes advancing the fundamental understanding of liquid crystalline phase behavior of 2D nanomaterials. Along with recent manufacturing innovations, this progress promises increased liquid crystal processability and scalable production of advanced, aligned materials.[2]

Figure 2.18. Illustration of shear-induced fluid-phase processes for anisotropic nanomaterials. Reprinted with permission from Davis, V. A., Anisotropic Nanomaterial Liquid Crystals: From Fiber Spinning to Additive Manufacturing. *Langmuir* **2023,** *39* (11), 3829-3836. Copyright 2023 American Chemical Society.[2]

2.4.1 Direct-Ink-Writing

Direct-ink-writing (DIW) is an additive manufacturing technique that uses extrusion-based methods to print, or build, a 3D structure in a layer-by-layer process. The ink is deposited via a movable nozzle. Ink composition varies based on the device being printed and the properties needed for successful printing. Colloidal gels and suspensions, polymer melts, waxes, and polyelectrolyte complexes are all examples of materials used in DIW inks.[107] With a wide variety of ink composition materials available, potential applications of DIW are also widespread. Sensors, drug delivery devices, printed electronics, and MEMS devices are a few examples.[107, 108]

DIW can be subdivided based on the extrusion method used. The two most common are continuous filament-based, in which a continuous stream of filament is deposited on the printer stage, and droplet-based, in which individual drops of ink are deposited (**Figure 2.19**).[107] Robocasting and inkjet printing are examples of each, respectively. Other types of DIW include tip-based direct writing and laser-based direct writing. No matter which deposition technique is used, all DIW methods are beneficial in that material is only deposited where desired, thus reducing waste material, and structure design is completed via CAD or another similar computer design software, making design changes and prototyping easy to manage.[108]

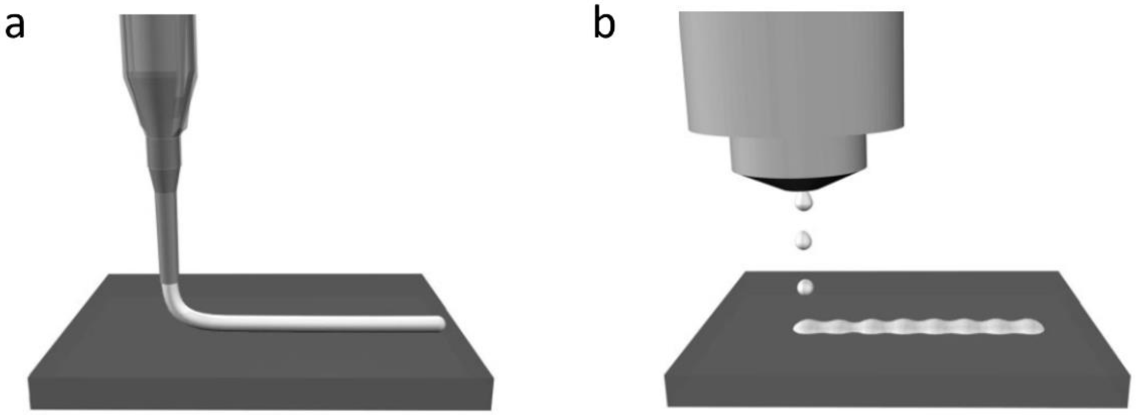

Figure 2.19. a) Filament-based DIW and b) droplet-based DIW.[107] Reprinted with permission from Lewis, J. A., Direct ink writing of 3D functional materials. *Advanced Functional Materials* **2006**, 16 (17), 2193-2204.

Formulating ink for any of the DIW methods is a complex task. The ink must simultaneously hold the properties required for flow through the printer equipment, most notably the narrow deposition nozzle, while also maintaining the necessary properties for successful printing. Desired rheological parameters, such as apparent viscosity, viscoelastic properties, and yield stress, are important in these regards and depend on the specific DIW technique implemented.[109] The ink's viscoelastic response determines its ability to flow through the nozzle which must then be immediately followed by "setting" so that printed structure maintains its shape and is able to have more layers of the ink built upon it. Interparticle attraction within the ink can also be manipulated to tune mechanical properties such as yield stress and shear modulus.[107] Controlling these rheological parameters allows for more complex build geometries with finer scales and higher resolution than what may have been achievable with preliminary inks.

Salt concentration also affects the interparticle forces of the nanoparticle ink discussed above. Interparticle attractions generally increase with increasing salt concentration. Formulating inks with a specific salt concentration aids in the effort to build 3D spanning features, a task that is often difficult to do with DIW techniques. By adding salt to the ink, Li et al. induced a phase transition from a fluid phase to a gel phase.[110] This produced an ink with a greater than needed elasticity to achieve the spanning features due to the increased interparticle attraction, and thus, resulting in the ink becoming more of a rod-like filament as it is deposited from the print nozzle.

Two-dimensional nanomaterials have been successfully used in DIW processes. Due to their high mechanical strength, electrical conductivity, and thermal conductivity, many 2D nanomaterials have the perfect combination of desirable properties for conductive DIW ink fillers. An additional benefit of many nanosheets and nanoplatelets is the natural affinity for alignment in the printing process, as illustrated in **Figure 2.20**. Even in droplet jetting DIW, the drying process of the droplets has been utilized to encourage self-assembly of the sheets and creating excellent alignment within the droplet-jetting printed ink lines.[111]

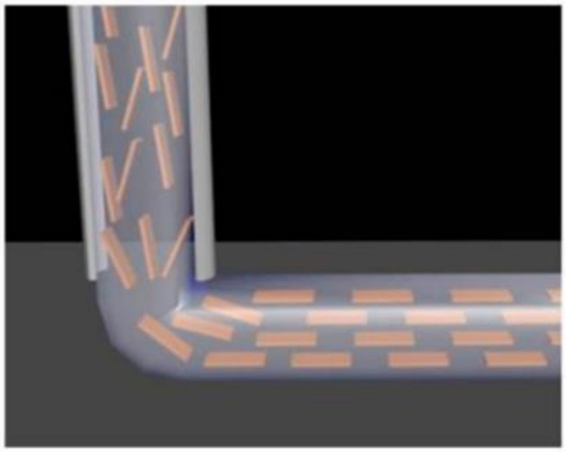

Figure 2.20. Illustration of 2D nanomaterials undergoing the continuous filament DIW printing process.[111] Reprinted with permission from Li, W.; Li, F.; Li, H.; Su, M.; Gao, M.; Li, Y.; Su, D.; Zhang, X.; Song, Y., Flexible Circuits and Soft Actuators by Printing Assembly of Graphene. *ACS Applied Materials & Interfaces* **2016**, 8 (19), 12369-12376. Copyright 2016 American Chemical Society.

In the case of DIW of electronic devices, there are a select few 2D nanomaterials that dominate the field. Graphene and its derivatives are currently the most widely used nanosheets in DIW, due to their flexibility, high light transmittance, high Young's modulus, large surface area, and also their highly tunable properties such as aspect ratios and surface chemistries.[112] This tunability leads these materials to be used in a wider range of possible ink formulations and thus more applications. More recent work has utilized MXenes in conductive inks for printed electronics. Much of this research is novel in that the inks are composed with no additives. While additives can help with the tunability of an ink, they can also cause complications in the printing and manufacturing processes.[23] Therefore, fabricating inks without the use of additives is extremely helpful in the improvement of printing high performing electronics.

2.4.2 Fiber-Spinning

The use of lyotropic liquid crystals in wet fiber-spinning was most notably popularized with the commercialization of Kevlar, a high-strength fiber produced through wet-spinning *p*-polyphenylene terephthalamide (PPTA) dispersed in sulfuric acid.[2] Decades later, organic 1D nanomaterials experienced a similar surge in recognition when carbon nanotubes in acids were successfully wet-spun into fibers.[49, 113] In recent years, attention has turned to the ability to utilize 2D nanomaterials with outstanding properties to produce advanced materials through fiber spinning methods.

Due to their carbon-based structure and high electrical and electrochemical properties, graphene and its derivatives have been heavily investigated as source materials for fiber spinning. Graphene fibers were first developed by Gao and Xu in 2011 from wet spinning aqueous graphene oxide liquid crystals.[114] These fibers are a relatively new type of carbonaceous fiber that are expected to transcend traditional carbon fibers due to their excellent mechanical and transport properties.[115] In the past decade, research and publications involving graphene fibers have steadily increased, with potential applications in smart devices and flexible electronics. Despite increasing research in the field, challenges still abound. Potentially hazardous exposure for humans in the process of wet-spinning graphene and scaling up the process to industry expectations lead the concerns for applicability purposes, with limited fundamental understanding of dispersion rheological behavior and structure-property-processing relationships still impeding the research.[115] However, the excellent electrical and thermal conductivity and high strength of graphene fibers maintain the promise of future success.

More recently, MXenes have garnered attention as 2D candidates for wet fiber spinning. Less than a decade after their discovery, Zhang et al. successfully spun additive-free liquid crystalline MXene dispersions into freestanding fibers (**Figure 2.21**).[23] These fibers exhibited electrical properties that surpassed any existing nanomaterial-based fibers at that time, highlighting the potential of MXene-based devices such as supercapacitors and sensors. It was also found that by tuning the properties of the liquid crystalline MXene dispersions, final properties and morphology of the spun fibers could be adjusted. This provided insight into various avenues by which MXene-based devices can be improved through adjustments at the nanoscale. Though MXenes typically lack the high strength found in graphene, the electrical properties make them a more desirable candidate for the production of devices in energy storage and heating.[2, 23]

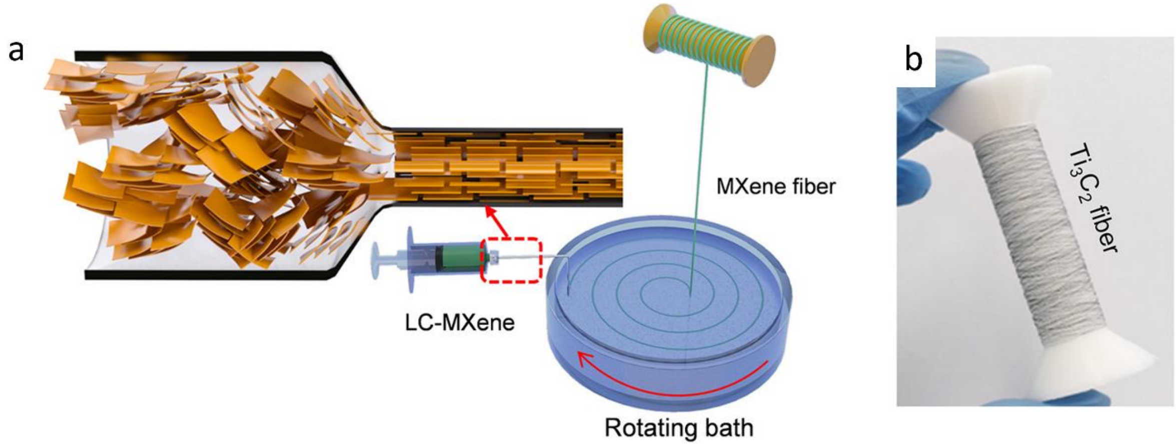

Figure 2.21. a) Schematic of the wet-spinning process for MXene fibers used by Zhang et al. b) Photograph of a 5 m MXene fiber produced from the wet-spinning process.[23] Reprinted with permission from Zhang, J.; Uzun, S.; Seyedin, S.; Lynch, P. A.; Akuzum, B.; Wang, Z.; Qin, S.; Alhabeb, M.; Shuck, C. E.; Lei, W.; Kumbur, E. C.; Yang, W.; Wang, X.; Dion, G.; Razal, J. M.; Gogotsi, Y., Additive-Free MXene Liquid Crystals and Fibers. *ACS Central Science* **2020**, 6 (2), 254-265. Copyright 2020 American Chemical Society.

2.5 Fundamentals of Charged Materials

As MXenes are charged 2D nanomaterials, understanding the fundamentals of charged particle behavior and interparticle interactions is vital to elucidating the phase behavior of MXenes. Investigating the effects of salt addition to aqueous MXene dispersions, as is the focus of Chapter 5, increases the need to understand the foundational theories focused on ionic strength and the forces that influence charged particle behavior. Though interesting from a fundamental standpoint, these concepts also directly affect applied research in materials chemistry, physics, and a number of engineering disciplines.[116]

2.5.1 Electric Double Layer (EDL)

The accumulation of ions surrounding a charged particle in a solution is conventionally known as the electric double layer (EDL). The concept of the EDL was first proposed by Helmholtz in 1853 and consists of two parallel planes with equal but opposite electrical charges at solid-liquid interfaces (**Figure 2.21**). If a particle, including 2D sheets, has negatively charged surfaces, then once dispersed in a solvent, a layer of positively charged ions (cations) will begin to form nearest the sheet surface. This layer is known as the Stern layer. Parallel to this is the diffuse layer that contains less concentrated counterions and co-ions, which are oppositely charged to the counterions (anions in this scenario). Beyond the diffuse layer is the bulk liquid solution. The counterions are attracted to the oppositely charged surface of the particle but tend to diffuse away to the less concentrated bulk liquid. Along with a deficiency of co-ions near the particle surface due to electrostatic repulsion, this results in an exponential decay of the electrical potential of the solution.[88] The potential of the dispersion can therefore be measured from the surface to any point in the dispersion, as shown in **Figure 2.22**.

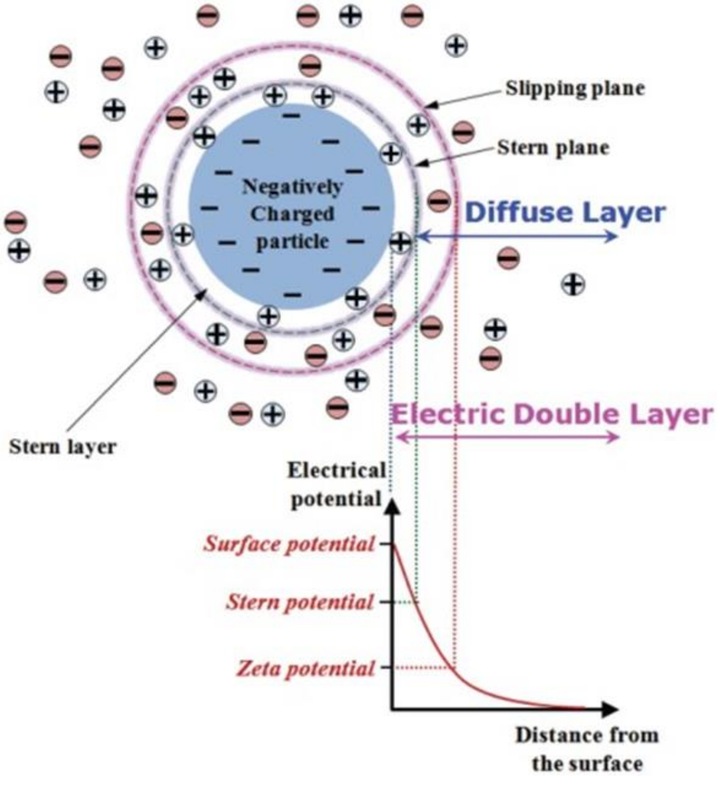

Figure 2.22. Schematic representation of the electrical double layer (EDL) surrounding a charged particle.[117] Reprinted from Park, S.-J.; Seo, M.-K., Chapter 1 - Intermolecular Force. In *Interface Science and Technology*, Park, S.-J.; Seo, M.-K., Eds. Elsevier: **2011**; Vol. 18, pp 1-57, with permission from Elsevier.

Charged particles in dispersions remain stable due to mutual repulsion from the interactions between intersecting diffuse EDLs.[88] Knowing the thickness of the EDL can aid in theoretical predictions or understanding observed behavior of charged particles. The EDL thickness is also known as the Debye screening length (κ^{-1}) and is proportional to the inverse of the ionic strength. It can be calculated through the following equation:

$$\kappa^{-1} = \sqrt{\frac{\varepsilon_r \varepsilon_0 k_B T}{\sum_i \rho_{\infty i} e^2 z_i^2}} \tag{8}$$

where ε_r is dielectric constant (78.4 for water), ε_0 is permittivity of free space, k_B is Boltzmann constant, T is temperature, e is electric charge, z_i is ion valency, and $\rho_{\infty i}$ is number density of ion i.[118] This is dependent on the properties of the solution in which the charged particles are dispersed. Therefore, the ionic strength of the dispersion is also key to charged particle behavior. The ionic strength of a salt solution can be calculated through the following equation:

$$I = \sum_{i=1}^{n} \frac{1}{2} c_i z_i^2 \tag{9}$$

where c_i is the concentration of ion i and z_i is again the ion valecy. For monovalent ions in which $z_i = 1$, the ionic strength is equivalent to the molarity of the solution. Increasing the ionic strength of a dispersion or the valency of the ion will result in a decreased Debye length.

2.5.2 Electroviscous Effect

The viscosity enhancement that occurs in electrolyte solutions is known as the electroviscous (EV) effect.[119] Early theoretical discussions of this effect emerged from Eyring's rate theory and Einstein's derived equation. Using the basis of Eyring, the viscosity of a colloidal suspension (η_s) could be calculated from the summation equation:[119]

$$\eta_s = \eta_m + \eta_\phi + \eta_p \tag{10}$$

where η_m is the viscosity of the dispersing medium, η_ϕ is the viscosity caused by crowding of colloidal particles, and η_p is the viscosity contribution of electrostatic interaction between charged particles. Einstein's derivation resulted in the following equation:[120]

$$\eta_s = \eta_m(1 + 2.5\phi) \tag{11}$$

where ϕ is the volume fraction of the colloid. It should be noted, though, that this equation only applies to dispersions where $\phi < 1\%$.

In the following years, the EV effect was then further divided into three classes: primary EV, secondary EV, and tertiary EV. Primary EV referred to distortion of the EDL around colloidal particles. This distortion originates from changes in the flow field caused by the electrostatic forces exerted by the particle on the fluid. This distortion increases both energy dissipation and viscosity of the dispersion. Smoluchowski first considered this effect and proposed the following equation based on Einstein's own derivation:[121]

$$\eta_s = \eta_m(1 + 2.5(1 + p)\phi) \tag{12}$$

where p is the primary EV coefficient. This coefficient is a function of both the zeta potential and the size of the colloidal particle radius relative to the EDL.[122] The secondary EV effect referred to interactions between EDLs of separate particles, while the tertiary EV effect described rheological behaviors under an electric field.[119] Onsager also commented on the increased viscosity of electrolyte solutions through similar considerations, and it was from this that the concept of ion atmospheres originated.[123] This theory stated that the distortion of this ion atmosphere caused by the atmospheres overlapping with one another resulted in more drag force, and therefore, increased viscosity.

Research of monodisperse polystyrene dispersions by Sone-Masui and Watillon first demonstrated the primary EV in a quantifiable experimental method.[124] The results from their work were further studied and expanded through various theoretical methods.[125, 126] In more recent years, studies of EV effects have focused primarily on the lowering of viscosity as a result of salt addition in dispersions of polymers, proteins, and colloids.[122, 127, 128] Though some attention has been focused on universal viscosity equations to account for EV effects, research focused on individual systems continues to provide insight into charged particle behavior.[119]

2.5.3 Derjaguin-Landau-Verwey-Overbeek (DLVO) Theory

The overall force between particles is the sum of attractive van der Waals (vdW) forces and repulsive EDL forces. Developed by Derjaguin and Landau in 1941 and expounded upon by Verwey and Overbeek in 1948, this classical theory of interparticle interactions is now collectively known as the DLVO theory. The equation for this theory can simply be portrayed as:

$$W_{total}(D) = W_{vdW}(D) + W_{EDL}(D) \tag{13}$$

where W_{total} is the total interaction energy, W_{vdW} is interaction energy from the attractive van der Waals forces, and W_{EDL} is the interaction energy from the repulsive EDL forces. This theory particularly helps understand colloidal stability and aggregation tendencies of specific systems. Attractive van der Waals forces are almost always present in colloidal systems though their scaling depends on shape. These forces result from the interactions between dipoles of atoms and molecules.[129] They can be most simply approximated through the following equation:[129]

$$W_{vdW}(D) = -\frac{H}{12\pi D^2} \tag{14}$$

where *H* is the Hamaker constant and *D* is the distance between the surfaces.

Repulsive electrostatic interactions, or the EDL forces, are especially important to consider in charged particle system. The ionic strength of a dispersion will directly affect the repulsive interparticle forces. When two charged particles approach one another, their EDLs will begin to overlap, resulting in repulsive forces. As discussed above, increased salt concentration will shrink the EDL of a charged particle; therefore, the salt concentration will affect the magnitude of the repulsive forces between two approaching particles.[130] For 2D materials, the repulsive forces can be approximated by two identical planar surfaces and calculated using the following equation:[130]

$$W_{EDL}(D) \approx 2A\varepsilon_r\varepsilon_0\kappa\xi^2 e^{-\kappa D} \tag{15}$$

where *A* is the surface area of the 2D materials, ε_r is the dielectric constant, ε_0 is the permittivity of vacuum, ξ is the zeta potential, κ is the inverse of the Debye length, and *D* is the distance between the surfaces.

When these two competing forces are summed together, the total interaction energy can be plotted as a function of separation distance (**Figure 2.23a**).[129] At very short separation distances, there exists a primary minimum due to increased attractive van der Waals forces inducing aggregation of particles. As separation distance increases, the total DLVO energy progresses through a maximum as EDL forces dominate. Upon further increase in separation distance, van der Waals forces increase in magnitude and cause the total energy to go through a shallow minimum, referred to as a secondary minimum.[129] Due to the effect of salt addition on EDL repulsive forces, the salt concentration of a dispersion will also effect the DLVO energy profile (**Figure 2.23b**). High salt concentration result in dominating attractive van der Waals forces while low salt concentrations result in repulsive particles and increased EDL forces.[129]

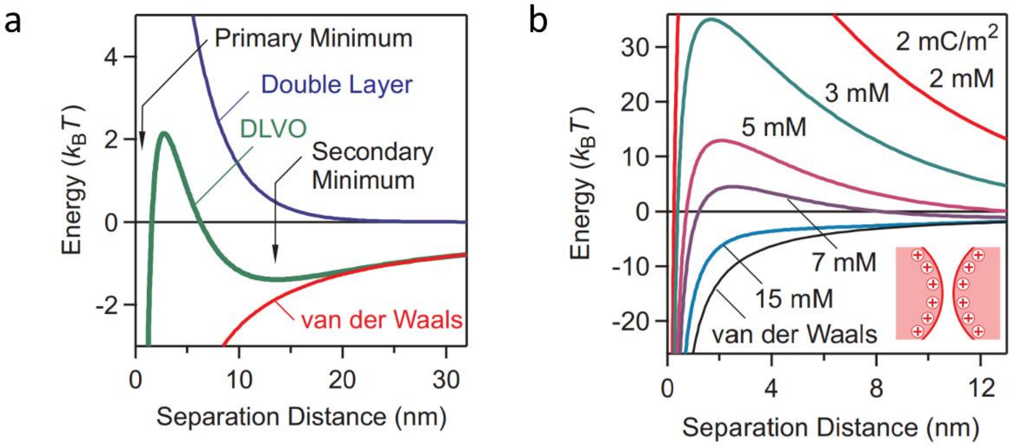

Figure 2.23. a) Total DLVO energy profile as a function of particle separation distance. b) Effect of salt concentration on the total DLVO energy profile.[129] Reprinted with permission from Trefalt, G.; Borkovec, M., Overview of DLVO theory. *Laboratory of Colloid and Surface Chemistry*, University of Geneva, Switzerland **2014**, 304.

2.6 Concluding Remarks

The investigation into lyotropic liquid crystalline behavior of anisotropic materials has been ongoing for over a century. The earliest work was predominantly focused on 1D nanomaterials, such as V_2O_5 and TMV. Despite this, most of the current knowledge of 1D systems has been gained fairly recently when considering the long history of liquid crystal research. Fundamental research involving 2D nanomaterials has been far less developed than their 1D counterparts thus far. With the extent of 1D nanomaterial research that is still required to obtain comprehensive understanding of phase behavior and relationship to properties, it can be easily understood how 2D materials will require substantially more for an equivalent understanding.

The sheer number of parameters that can affect phase behavior complicates the development of a unifying method for predicting the behavior of more recently discovered materials. Even materials that have been extensively studied for decades, such as laponite, sometimes require reinvestigation into phase behavior and associated properties when new experimental methods produce discrepant results to those observed prior.[85] The shape and size polydispersity of 2D materials, as well as the scaling effects of interparticle interactions between 2D materials, creates a field of study with high complexity. Just as experimental investigations have been vital to the progression of the 1D nanomaterial field in recent past, the 2D nanomaterial field is in a similar state presently. Experimental results are necessary to create a deeper understanding of the effects of a variety of parameters on phase transition and properties and to develop the structure-property-processing relationships of complex materials.

Chapter 3 – Materials & Methods

This research focuses on the understanding of fluid-phase nanomaterial dispersion behavior and properties. To achieve the dispersions studied in this work, the nanomaterial of interest must first be synthesized and dispersed in the solvent of choice. This chapter details the synthesis process for MXenes, manganese oxide nanowires, and copper nanowires. The methods to produce size fractionated MXenes for the study of size effects and MXene-NaCl dispersions for the study of ionic strength effects are also discussed. Characterization methods and experimental protocols are included in this chapter.

3.1 MXene Preparation

3.1.1 Synthesis from MAX Phase

Parental MAX phase (Ti_3AlC_2) was provided by Dr. Beidaghi's research group through the extent of this work. The minimally intensive layer delamination (MILD) process[78] was used to synthesize the $Ti_3C_2T_x$ MXenes. Aluminum was selectively etched from the parental MAX phase, Ti_3AlC_2, using in situ HF-forming etchant. All amounts detailed below are based on using 3.0 g of parental MAX phase. To make the etching solution, DI water was added to a 12.0 M hydrochloric acid solution (HCl, ACS grade, purchased from BDH) to obtain a 9.0 M HCl solution (60 ml total). 4.8 g of lithium fluoride (LiF, 98+% purity, purchased from Alfa Aesar) was then added to the solution and stirred with a Teflon coated magnetic stir bar for 20 min at 35 °C until the salt was completely dissolved. The solution was then moved to an ice bath to prevent overheating. Over 10 min, 3.0 g of Ti_3AlC_2 was slowly added to the solution. The resulting solution was moved to a 35 °C oil bath to maintain constant temperature throughout the entire reaction time. The reaction underwent constant stirring for 24 hrs. The solution was then divided equally into 50 mL centrifuge tubes, with each tube containing no more than ~30 mL. DI water was then added to fill up the tubes to 40 mL and vigorously shaken. The solution was then washed through centrifugation at 2300 xg for 5 min. The acidic supernatant was decanted, DI water added to about 40 mL total volume in each tube, and washing repeated until the pH of the supernatant reached 6. The solution was then centrifuged at 2300 xg for 1 hr to separate the single-layer MXene sheets from multilayer sheets and unreacted MAX phase. From this, the supernatant was collected and used as the initial dispersion. The sediments were properly disposed.

3.1.2 MXene Size Fractionation

The resulting single-layer MXene sheets ranged in size from 0.1 µm – 8 µm. Centrifugation was used to fractionate the dispersion by size. The delaminated MXene sheets were centrifuged at 1200 xg for 1 hr in 50 mL tubes. The sediment was collected and then redispersed in DI water through vigorous shaking to form a colloidal dispersion. This was labeled as large MXenes. The supernatant remaining after the removal of the large MXene sheets was then centrifuged for a second time at 2300 xg for 1 hr. The supernatant from this centrifugation was gathered and labeled as small MXene sheets. The sediment from this centrifugation run contained medium-sized MXene sheets, though these were not used in this work.

To produce bimodal MXenes, the produced large and small MXene sheets were added together in a 1:1 volume ratio. To ensure precise ratios were always achieved, the concentration of the size fractionated large and small MXenes were determined through thermal gravimetric analysis (TGA). Using basic mathematical equations, the large and small MXenes were added together in amounts to produce equal volume fractions of each. Once mixed, these dispersions were allowed to stir with a magnetic stir bar for ~1 hr at room temperature before use or storage.

3.1.3 Preparation of MXene Dispersions

Dispersions with three MXene size distributions were prepared: large MXenes (denoted as L-MXenes) with an average lateral dimension of ~3 µm, small MXenes (denoted as S-MXenes) with an average lateral dimension of ~0.3 µm, and a bimodal mixture of 50% L-MXene and 50% S-MXene by volume (denoted as B-MXenes). To understand the phase behavior of the three types of MXene dispersions, a series of dispersions of each size fraction were prepared with a range of sheet concentrations. The dispersions were all concentrated using a combination of a pressurized stir cell and superabsorbent polymer beads.[131, 132] To accurately determine the concentration of all dispersions investigated in this work, thermal gravimetric analysis (TGA) was used. The weight fraction w obtained from this was converted to volume fraction ϕ via Eq.4 and Eq.5:

$$\phi = \frac{w\rho_{rel}}{1+(\rho_{rel}-1)w} \tag{4}$$

$$\rho_{rel} = \frac{\rho_s}{\rho_p} \tag{5}$$

where ρ_{rel} is the relative density, ρ_s is the aqueous solvent density, and ρ_p is the particle density of the MXene sheets (5.2 g/mL).[133, 134] The dispersion concentration c can also be converted into units of mg/mL from the determined weight fraction through Eq.6:

$$c = \frac{w}{w+(\rho_{solvent}-w\rho_{rel})} \tag{6}$$

3.1.4 Preparation of MXene/NaCl Dispersions

Aqueous NaCl salt solutions were prepared separately at various ionic strengths. Once sufficiently mixed, these solutions were added to MXene dispersions to achieve desired sheet concentrations and ionic strengths. The MXene/NaCl dispersions were allowed to stir for ~1 hr before proceeding with use or refrigerated storage. NaCl is a monovalent salt; therefore, the ionic strengths of the NaCl solutions are equivalent to the molarity of the salt solutions. The dispersion ionic strengths used in this work are 0.01, 0.05, 0.1, and 0.5 M NaCl. Furthermore, the Debye length (κ^{-1}) is calculated as the total length of the electrical double layer and is only a function of the properties of the salt solution by the following equation:

$$\kappa^{-1} = \sqrt{\frac{\varepsilon_r \varepsilon_0 k_B T}{\sum_i \rho_{\infty i} e^2 z_i^2}} \tag{4}$$

where ε_r is dielectric constant (78.4 for water), ε_0 is permittivity of free space, k_B is Boltzmann constant, T is temperature, e is electric charge, z_i is ion valency, and $\rho_{\infty i}$ is number density of ion i.[118] For 0.01, 0.05, 0.1, and 0.5 M NaCl, the Debye lengths are 3.04, 1.36, 0.96, and 0.43 nm, respectively.

3.2 Nanowire Synthesis

3.2.1 Manganese Dioxide Nanowires

Manganese dioxide nanowires were synthesized via a facile, double-solvent approach as shown in **Figure 3.1** and previously reported by Chen et al.[103] When performed as described below, 1D α-MnO_2 with wire-like morphology is produced. 450 mg of $MnCl_2 \cdot 4H_2O$ is placed in a three-neck round bottom flask with 80 mL of isopropanol and sonicated for twenty minutes, or until the manganese salt is completely dissolved. 250 mg of crystalline $KMnO_4$ is placed into a vial with 8 mL of deionized water and sonicated for no more than five minutes. The three-neck flask was then attached to a reflux condenser, and the solution is allowed to reach reflux conditions at ~80 °C, as monitored with a thermocouple, while maintaining a vigorous stir rate. Once refluxing began, the $KMnO_4$ solution is swiftly injected into the refluxing manganese salt solution. The reaction takes thirty minutes to synthesize the MnO_2 nanowires with the desired aspect ratio of ~50. Less reaction time would lead to shorter nanowires formed, thus decreasing the aspect ratio of the nanowires. The reaction temperature must not surpass 83 °C or else the MnO_2 will over-react. Once the reaction is complete, the nanowires can be seen as the black precipitate formed in the flask.

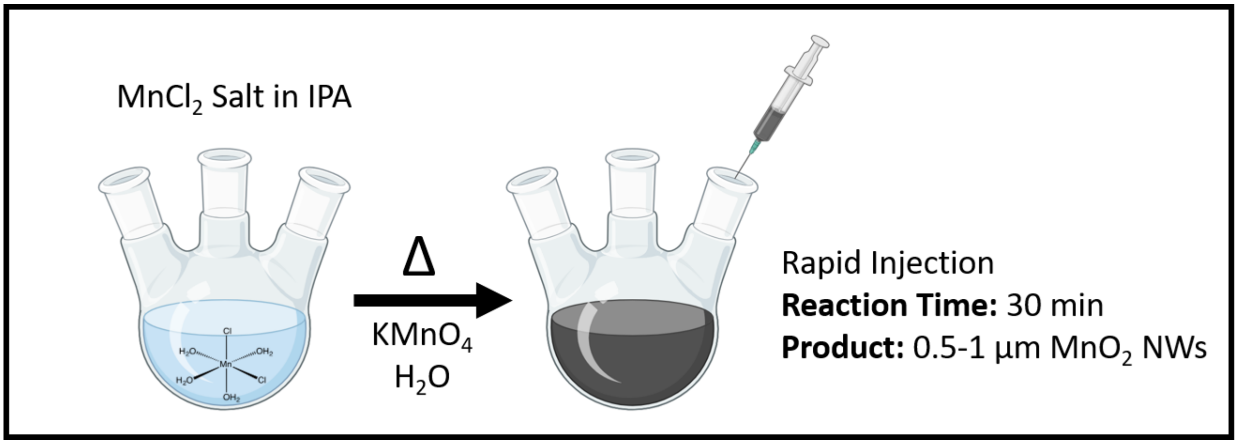

Figure 3.1 Reaction scheme for synthesizing MnO_2 NWs

The described synthesis scheme is a precipitation method following a dissolution-crystallization mechanism. In this process, disordered precursors disappear followed by the development of the primary nanorods. Simultaneously, oriented attachment along the lateral faces occurs to complete the crystal growth process of the NWs. Specifically in this reaction, the Mn^{2+} ions from manganese salt dissolves in isopropanol. When the $KMnO_4$ is introduced into the system, a redox reaction between the Mn^{2+} and Mn^{7+} cations occurs, spurring on nucleation. The injection and concentration of the $KMnO_4$ solution is critical during crystal growth as it affects the formation and stacking behavior of the nuclei. To obtain wire-like morphology with greater length and smaller diameter than nanorods, the injection must be done quickly in a continuous stream at the concentration stated above. Previous studies show that the nanowire crystal growth is complete within 5 minutes.[103] Further reaction time is used to increase the nanowire length and resultingly the aspect ratio.

The ratio of deionized water to isopropanol also affects the crystal growth and therefore the product morphology. The ratio was maintained at 1:10 (8mL:80mL) to ensure that the product has a wire-like morphology. The alkyl groups in isopropanol cause higher electron density around the oxygen atom, resulting in weaker hydrogen bonding. The water molecules will react more favorably with the structural MnO_6 octahedrons and bind more easily with their oxygen atoms. This will occur along the longitudinal direction, or the (001) crystal face, due to higher energy levels. This is the only preferred direction of growth when small amounts of water are used, as in the 1:10 ratio. When greater amounts of water are used and that ratio is increased, the increased number of water molecules available for binding causes aggregation of the molecules as well as allowing for growth in other directions in the octahedral plane, both leading to a spindle-like morphology.

The MnO_2 NWs were purified via a two-stage centrifugation technique that also serves as a method to reduce aggregates in the final product, which can be seen in **Figure 3.2**. The precipitate obtained in the synthesis was distributed into conical centrifuge tubes and centrifuged at 5000 rpm (4700 g) for 20 min. The supernatant was decanted and discarded, and the bottoms were dispersed in ethanol within the centrifuge tubes. The tubes were centrifuged at 1000 rpm (188 g) for 5 min. This centrifuge run, having a low rate and short time, is considered a “knockout run” where only the large aggregates settle to the bottom of the tubes. The supernatant contains the desired product, so it is decanted into fresh conical centrifuge tubes to be further purified. The aggregated bottoms are discarded. Polarized optical microscopy (POM) of the supernatant and the bottoms was used to determine the appropriate removal of aggregates qualitatively, as described by Murali et al.[135] The new centrifuge tubes were centrifuged at 5000 rpm for 20 minutes, thus completing the first ethanol wash. The supernatant from this wash was decanted and discarded, while the bottoms were dispersed in ethanol once again. The tubes were centrifuged for 5000 rpm for 20 minutes. This completed the second ethanol wash. A third ethanol wash was performed by the same method as the second ethanol wash. Ethanol was used as the solvent of choice for purifying the MnO_2 NWs because the NWs disperse easily in ethanol, as well as its ability to solubilize any unreacted $MnCl_2$ and the reaction by-product, potassium chloride. After the three ethanol washes were complete, the bottoms were dispersed in deionized water. Six water washes were completed at 5000 rpm for 1 hour each. The bottoms were then dispersed in the solvent of choice for study and underwent one wash in that solvent at 5000 rpm for 20 minutes. The final product was then dispersed in the chosen solvent at the desired concentration.

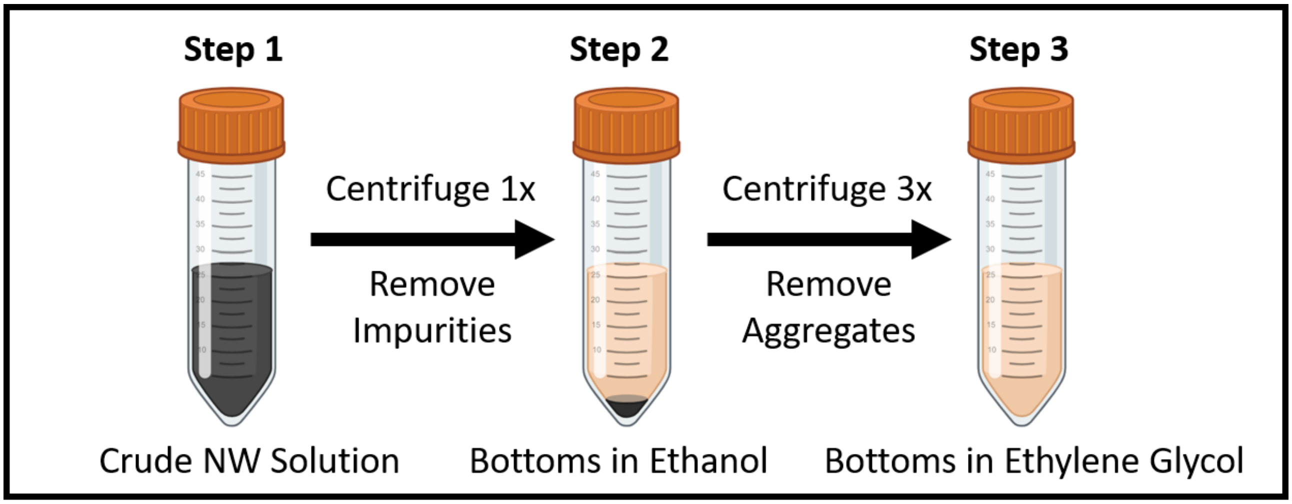

Figure 3.2 Purification scheme for MnO_2 NWs

3.2.2 Copper Nanowires

Copper nanowires were synthesized via a large-scale procedure utilizing a pressure cooker and mild reaction conditions as displayed in **Figure 3.3** and as previously reported by Li et al.[136] In this synthesis, 6.8 g of $CuCl_2 \cdot 2H_2O$ and 7.9 g of glucose were combined in a beaker containing 800 mL of DI water under magnetic stirring. In another beaker, 80 mL of oleylamine and 0.8 mL of oleic acid were combined with 140 mL of ethanol under magnetic stirring. Once mixed, these two solutions were combined in a large beaker and diluted with DI water to a total volume of 4000 mL. This bright blue solution was then stirred for 12 hours over 50 °C. Once this was complete, the now murky blue solution was transferred to a pressure cooker where the solution reacted under high pressure and temperature for 2-12 hours. The reaction conditions and reaction time varied based on the setting chosen on the pressure cooker. Li et al. found that a 6-hour reaction time resulted in long but untangled Cu NWs. In total, two batches of Cu NWs were synthesized in the Davis lab. The first batch was reacted under the "Slow Cook" setting with a temperature of 98 °C for 4.5 hours. The second batch was reacted under the "Ultra" setting with a temperature of 98 °C for 6 hours. Pressure levels were not controllable on either of these settings. This reaction resulted in 4000 mL of a reddish-brown solution containing about 2.1 g of Cu NWs.

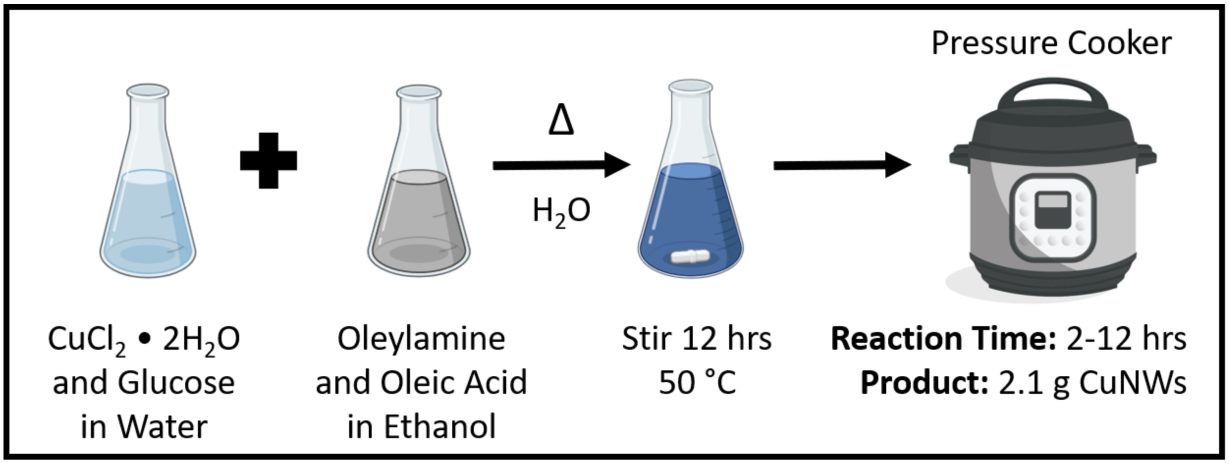

Figure 3.3 Synthesis scheme for Cu NWs

In this reaction scheme, $CuCl_2 \cdot 2H_2O$ serves as the copper precursor and glucose as the reducing agent. This reaction results in the copper ions that will grow into the Cu NWs. The oleylamine and oleic acid serve as dual capping agents that encourage the unilateral growth of the nanowires in the preferred direction of [110]. The use of dual capping agents is necessary for increased dispersibility of the Cu NWs. When only oleylamine is used as a capping agent, the nanowires are poorly dispersed; however, by adding oleic acid as a second capping agent, the synthesized Cu NWs are well-dispersed. Li et al.[136] found that the optimal volume ratio of oleylamine/oleic acid is 100 for nanowire growth and dispersibility.

The Cu NWs were purified in a similar manner as described for the MnO_2 NWs. The total post-synthesis solution is equally separated into centrifuge tubes. These were centrifuged at 10,000 rpm (10,500 g) for 30 minutes. The supernatants were decanted and discarded, and the bottoms were well dispersed in ethanol. The tubes are centrifuged again at 10,000 rpm for 20 minutes, followed by the decanting and discarding of the supernatants. The bottoms are again dispersed in ethanol. This is repeated three times for a total of four 20-minute ethanol washes. The bottoms were then dispersed in ethanol at the concentration of choice.

3.3 Experimental Techniques

3.3.1 Polarized Optical Microscopy

A Nikon Eclipse 80i optical microscope was used with a Nikon DS-Ri2 camera and Nikon Elements software to observe the MXene dispersions and microstructural changes as an effect of phase transitions. Cross-polarized images were taken with 20X/0.45 NA LU Plan Fluor and 60X/1.40 NA oil immersion objectives. All samples were prepared by using a glass rod to transfer a drop of the dispersion to a glass slide before placing a coverslip on top of the dispersion. Due to the opacity of MXene samples, no spacers were used. The edges of the coverslip were sealed with nail polish to prevent evaporation. In order to simultaneously see regions with perpendicular alignment the majority of images were taken with the analyzer at 5° relative to the polarizer.

3.3.2 Rheology

An Anton Paar Physica MCR 301 strain-controlled rotational rheometer was used to perform both steady shear and small amplitude oscillatory shear (SAOS) rheology. Most rheology was performed on either 25 mm diameter or 50 mm diameter parallel plate (PP) or cone-and-plate (CP) fixtures. Cone angles (θ) were 0.032 rad and 0.035 rad for 25 mm and 50 mm diameter plates, respectively (**Figure 3.4**). For more dilute dispersions, a concentric cylinder (ME21) fixture was used. Select dispersions were also repeated on various fixtures to confirm no gap dependency or other artifacts in the rheological data.

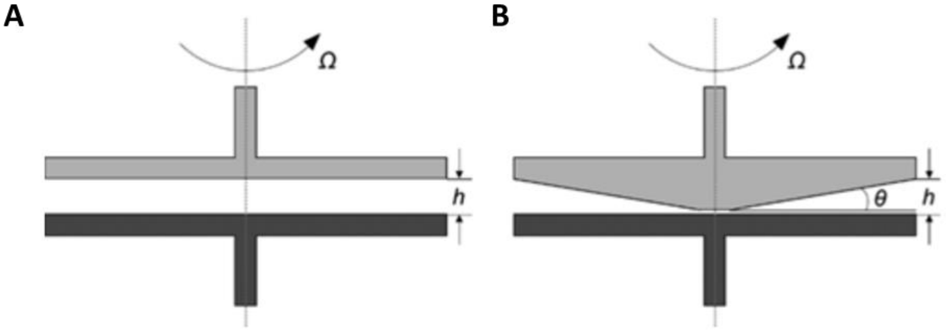

Figure 3.4. a) Parallel plate and b) cone-and-plate geometries.[137] Reprinted with permission from Song, H. Y.; Salehiyan, R.; Li, X.; Lee, S. H.; Hyun, K., A comparative study of the effects of cone-plate and parallel-plate geometries on rheological properties under oscillatory shear flow. *Korea-Australia Rheology Journal* **2017**, 29 (4), 281-294.

All MXene samples were kept refrigerated when not in use to reduce the potential for oxidation and hydrolysis; it is noted that these processes occur more slowly in concentrated dispersions.[138] The samples were taken out of the refrigerator two hours prior to rheological testing to allow for the sample to equilibrate to room temperature. Before loading, all MXene samples were vortex mixed for ~10 seconds. All rheological tests were carried out at 25 °C. To reduce any shear history effects, all samples were allowed to rest for one hour after loading. This was followed by a pre-shear protocol of 1 hr of steady shear at 0.01 s^{-1} for all samples. Step rate tests were used to determine the time required to obtain reliable data for flow curves. Due to the long rotational relaxation times for the large sheets and high concentration dispersions, samples could be on the rheometer for up to 15 hours. Silicone oil was used on the edges of fixtures, along with a combined evaporation blocker and deionized water trap, to prevent evaporation during these long testing times. No changes in the sample edge were detected at the conclusion of the test protocol. In addition, repeated amplitude sweeps in the linear viscoelastic region were run on representative samples to verify the dispersions remained stable throughout the testing time.

3.3.3 Thermogravimetric Analysis (TGA)

Understanding the phase behavior of MXenes requires a highly accurate method for concentration measurement. Once the MXene dispersions were produced, a TA Instruments Q50 thermogravimetric analyzer (TGA) was used to determine the concentration. By using a precise balance and a furnace, a TGA can measure the amount of MXene mass lost as a function of temperature. All samples were run under argon gas. A 10 °C/min ramp to 120 °C was used followed by a 30 min hold to evaporate all water within the dispersion. By using the Thermal Analysis (TA) software, the weight fraction of MXenes in the dispersion could be determined, which was then converted to volume percent for this work.

3.3.4 Atomic Force Microscopy

An Anton Paar Tosca 400 atomic force microscope (AFM) within an active vibration isolation and acoustic enclosure was used to determine lateral size and thickness of the MXene sheets. AFM samples were prepared by drop casting diluted MXene samples onto thermally oxidized silicon wafers or mica sheets. To minimize distortion of MXene sheets and the coffee-ring drying effect, the MXene samples were airdried on the lab benchtop overnight. Samples were placed in a storage container with the lid slightly lifted to allow air flow and minimize dust collection. When not in use, the AFM samples were kept in a desiccator to keep the sample surface dry. The MXene sheet dimensions were measured in tapping mode. Images were analyzed with both the Tosca Analysis and Gwyddion software to obtain height and lateral dimensions. MXene sheets are irregularly shaped, so the longest distance across the sheet surface was taken as the lateral dimension.

3.4 Theoretical Calculations and Modeling

3.4.1 Theoretical Phase Transition Calculations

Onsager's theory[40] is often used to calculate the theoretical lyotropic liquid crystalline phase transitions in dispersions of hard rods. Following this theory, the aspect ratio (length/diameter) of the rod is the main contributor to these calculations. However, Onsager's theory does not account for polydispersity, irregular shapes, or charged surfaces, leading to the development of multiple modifications to improve the accuracy of theoretical calculations for more complex dispersions.

The equations detailed by Tkacz et al.[139] in their phase transition calculations of graphene oxide dispersions are applied to the MXene dispersions in this work. These equations are based on modifications for 25% polydisperse infinitely thin hard platelet dispersions made through Monte Carlo simulations by Bates and Frenkel.[140] As determined through their simulations, dimensionless densities, ρ, for the isotropic-nematic phase transitions were found to be

$$\rho_I = n_I < L^3 > \approx 3.5 \tag{16}$$

$$\rho_{LC} = n_{LC} < L^3 > \approx 5.0 \tag{17}$$

where n_I and n_{LC} are the number densities of the isotropic and liquid crystal phases, respectively, and L is the platelet's longest lateral dimension.

Though MXenes are irregularly shaped, we used the following volume fraction equation assuming disk-like shape:

$$\phi = \frac{\pi}{4} n L^2 D \tag{18}$$

where ϕ is MXene volume fraction, L is the longest lateral dimension of the MXene sheet, and D is the thickness of the MXene sheet.

From this, the dimensionless density is:

$$\rho = \frac{4}{\pi} \phi \frac{L}{D} \tag{19}$$

Through rearrangement and utilization of Bates and Frenkel's dimensionless densities, isotropic and nematic phase transition volume fractions were solved for using the equations:

$$\phi_I = 2.7 \frac{D}{L} \tag{20}$$

$$\phi_{LC} = 3.9 \frac{D}{L} \tag{21}$$

To convert the concentration from volume fraction to mg/mL, we used:

$$C = \phi d * 1000 \tag{22}$$

where d is the density of MXenes. In this work, 5.2 g/mL was used based on Naguib et al. and Eom et al.'s experimental MXene research.[133, 134] However, it is noted that other authors use other densities for $Ti_3C_2T_x$ MXenes, such as 3.6 g/mL.

3.4.2 Herschel-Bulkley Model

The Herschel-Bulkley model was chosen to fit all rheological data in this research due to its widespread use as a benchmark for processability, particularly in direct-ink-writing. It is noted that in the absence of a significant yield stress the Herschel-Bulkley model reduces to a power-law model. The viscosity data for each dispersion was fitted to Eq.23:

$$\tau = \tau_0 + K\dot{\gamma}^n \tag{23}$$

where τ is shear stress, τ_0 is yield stress, K is flow consistency index, $\dot{\gamma}$ is shear rate, and n is flow behavior index. When fitted to rheological data, $n < 1$ signifies shear-thinning dispersions. When $n > 1$, the dispersion is shear-thickening, and if $n = 0$, the dispersion is yielding. In all steady-shear rheology plots in this work, data is represented by symbols and the Herschel-Bulkley Model fit is represented by a line of the color of the corresponding symbol.

Chapter 4 - Investigation of the Synthesis and Self-Assembly of Nanowire Systems

4.1 Motivation

The research endeavors described in this chapter stem from the need to gain initial understanding of the self-assembly of anisotropic colloidal systems before delving into research of the much lesser understood and more recently discovered 2D nanomaterial MXene. The phase behavior of 1D nanomaterials generally tends to be less complex than that of charged 2D nanomaterials due to less shape polydispersity and lack of electrostatic interactions when dispersed in non-electrolyte solutions. By initially studying 1D nanomaterials, a basic understanding of phase behavior and the role of synthesis parameters can be more easily obtained.

A general fundamental understanding of the self-assembly and tunability of one-dimensional (1D) nanomaterial dispersions was obtained through synthesizing and characterizing two nanowire systems: manganese dioxide nanowires (MnO_2 NWs) and copper nanowires (Cu NWs). 1D nanomaterials, including materials with the classifications of nanorods, nanowires, and nanotubes, have been extensively studied for decades. Despite this, much of the knowledge of 1D colloid behavior has been relatively recent, and the reopening of some previous phase behavior investigations indicates that the field is still heavily evolving in the face of new experimental and theoretical techniques.

Characterization methods, such as various forms of microscopy, are required to investigate colloidal self-assembly and stability. In this chapter, two microscopy methods were used for preliminary investigation into the self-assembly and phase behavior of the nanowire dispersions: polarized optical microscopy (POM) and atomic force microscopy (AFM). From this initial work, this chapter provides a succinct overview of MnO_2 NW dispersion microstructural changes as a function of concentration and describes future directions for continuing this research.

4.2 Manganese Dioxide Nanowires

Once the MnO_2 NWs were synthesized and purified, the nanowire dispersions were characterized using POM and AFM. Beginning with the initial concentration of the bottoms obtained from the centrifuge tubes post-purification, the dispersion was incrementally diluted to lower concentrations with each dilution step imaged through POM. This step-wise process results in progressive images of the MnO_2 NWs dispersed in EG at different concentrations that can then be studied for specific phase behavior and self-assembly signatures. Thermogravimetric analysis (TGA) was used to determine the concentration of the centrifuge bottoms, which was found to be 0.95 vol% (4.18 wt %). **Figure 4.1** displays possible birefringence seen in a sample of the 0.95 vol % MnO_2 NW dispersion. The stage was rotated 15° with each image, with the light portion along the lower edge slowly darkening before brightening. Accurately determining the presence of birefringence in these MnO_2 NW dispersion samples is difficult due to the opacity of the sample, especially when viewed through cross-polarizers. Additionally, while birefringence is indicative of the liquid crystal phase, observation of this signature alone does not confirm this phase. Rheological characterization or light scattering methods are required to confirm liquid crystallinity.

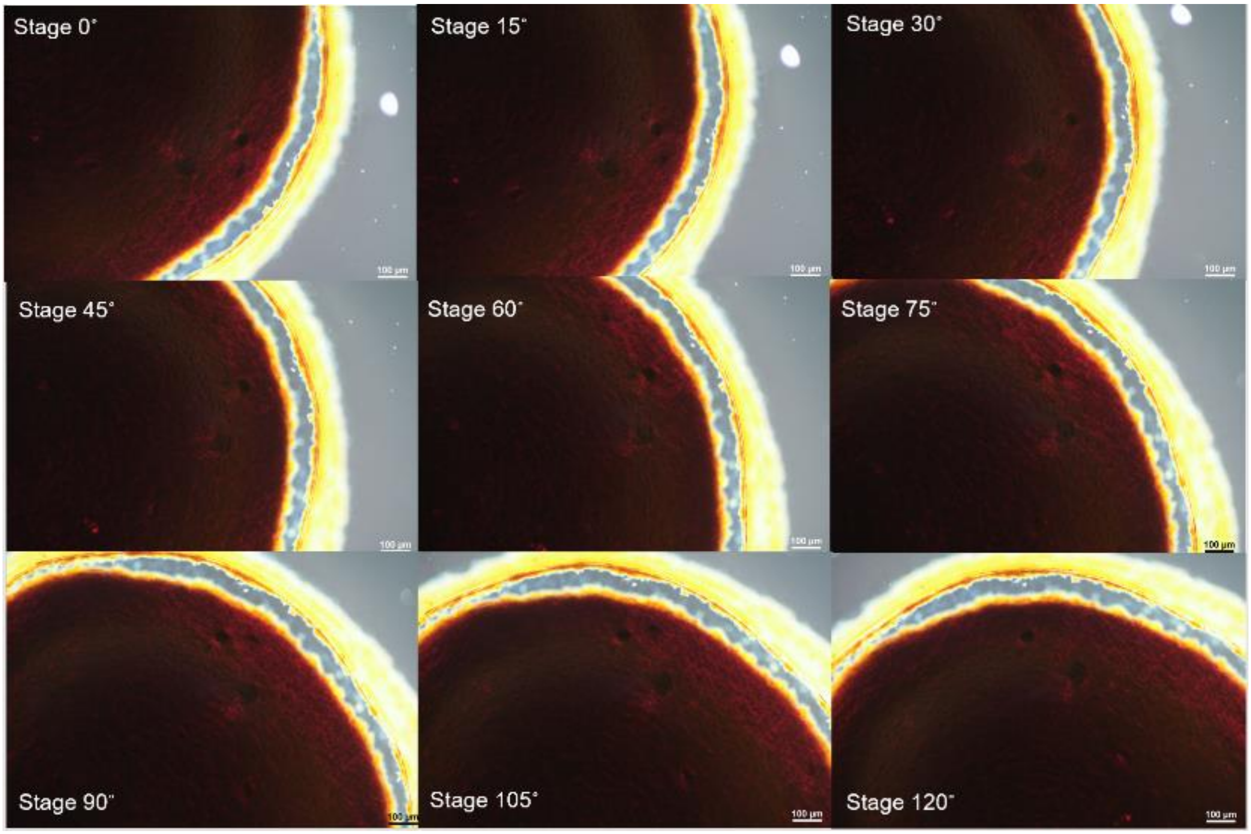

Figure 4.1. Cross-polarized microscopy of 0.95 vol % MnO_2 NW dispersion with 15° stage rotations. Scale bars are 100 µm.

The sample was diluted to 0.68 vol% (3 wt %), seen in **Figure 4.2**. The birefringence is still observed at this concentration as the stage of the microscope was rotated at 15° increments, shown in **Figure 4.2a**. The birefringence is more visible in this sample, though this could be due to the decreased opacity of a lower concentration dispersion. At first observation, the POM images also suggest the appearance of a nematic Schlieren texture, an optical indicator of the liquid crystalline phase, by the light and dark brush-like strokes radiating from the two dark masses within the sample. However, microscopy images without the use of cross-polarization of the same sample, seen in **Figure 4.2b**, shows that these masses are large aggregates within the sample and not part of the texture. Despite this, it is still hypothesized that liquid crystalline regions could be forming around these aggregates due to the birefringent textures. Further work with this dispersion should be conducted to investigate the birefringence observations, as the possibility of liquid crystalline regions tending to form around aggregates in a dispersion would be enlightening to the overall phase behavior of MnO_2 NWs.

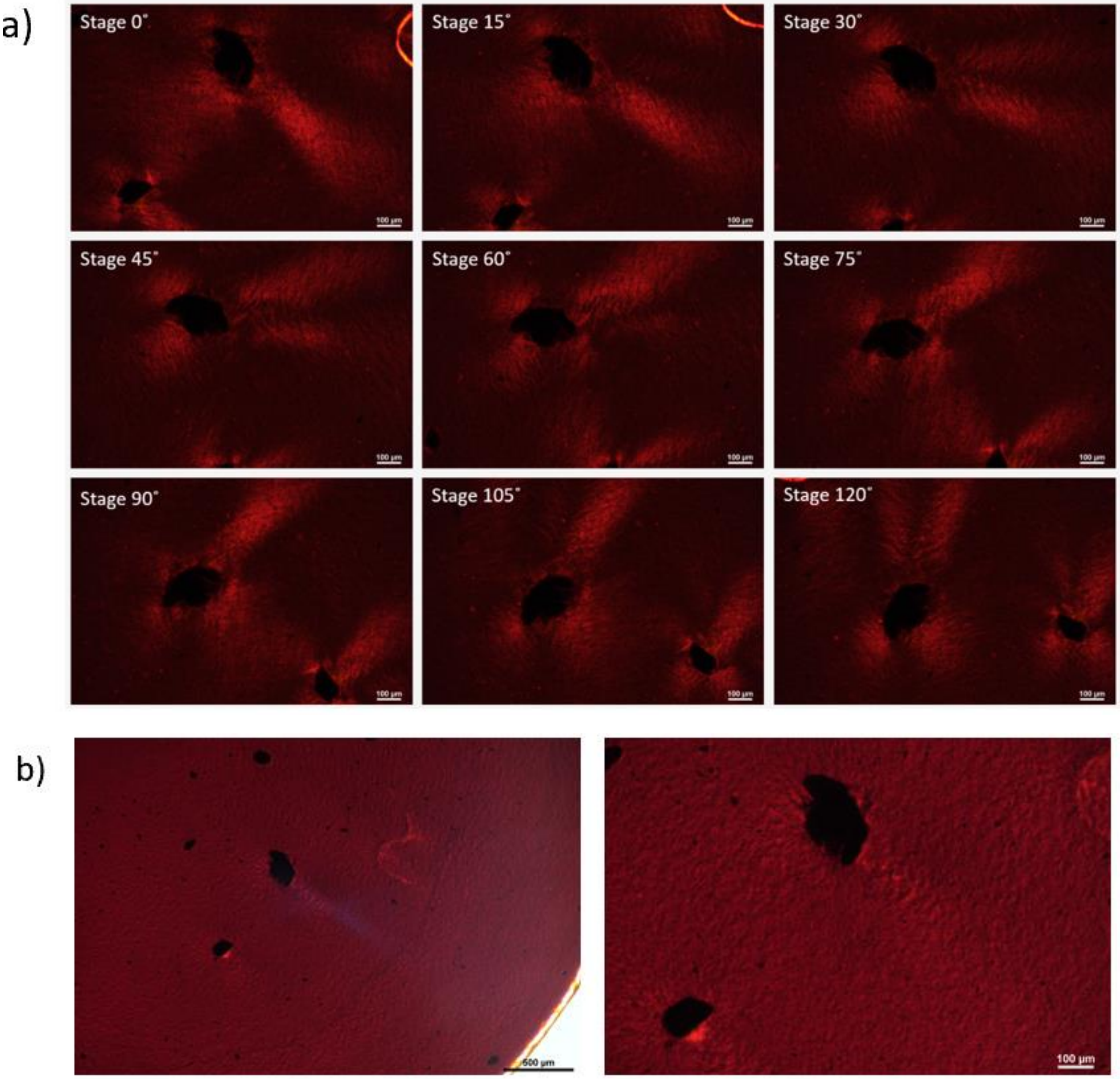

Figure 4.2. a) Rotational microscope images of MnO_2 NW dispersion at a concentration 0.68 vol% using a 10x lens with cross-polarizers. b) Microscopy images without cross-polarization of the 0.68 vol % dispersion using a 4x lens and a 10x lens, respectively.

Figure 4.3 shows a set of 15° stage rotation images of the sample further diluted to 0.45 vol % (2 wt %). Traces of birefringence can still be seen in this sample, though it is not as visible as in the previous sample. This likely indicates that the long-range ordering that birefringence suggests is becoming less pronounced with further dilution, as expected from typical lyotropic liquid crystalline phase behavior.

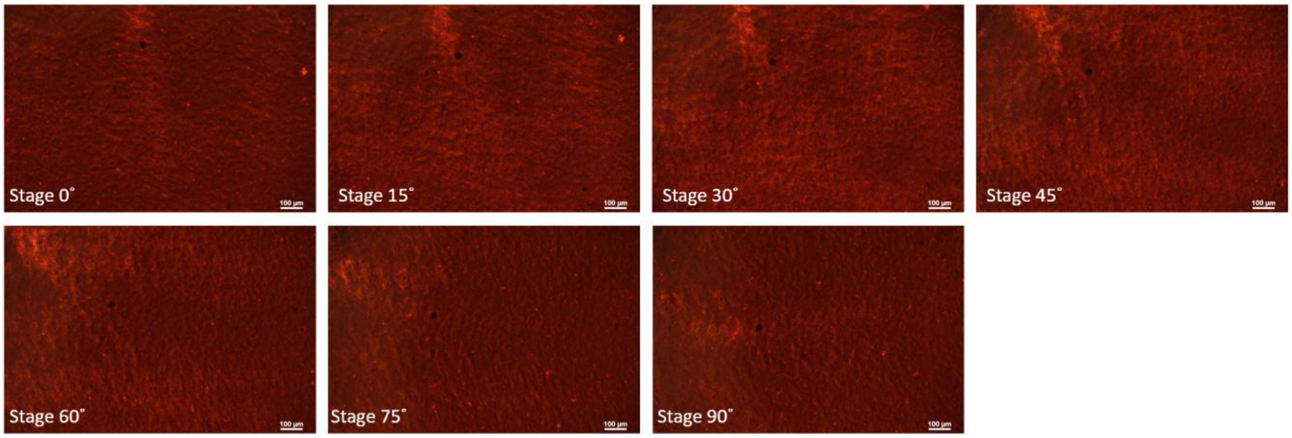

Figure 4.3. MnO_2 NW dispersion with a concentration of 0.45 vol % (2 wt %) imaged as the microscope stage is rotated and using a 10x lens with cross-polarizers.

At the next dilution of the MnO_2 NW dispersion of 0.20 vol% (1 wt %), no traces of birefringence are observed. As the stage rotates, the sample brightness appears unchanged, as seen in **Figure 4.4**. If the previous samples had indeed reached the liquid crystal phase, it appears through POM that at this concentration of MnO_2 NWs in EG, no regions of liquid crystallinity remain.

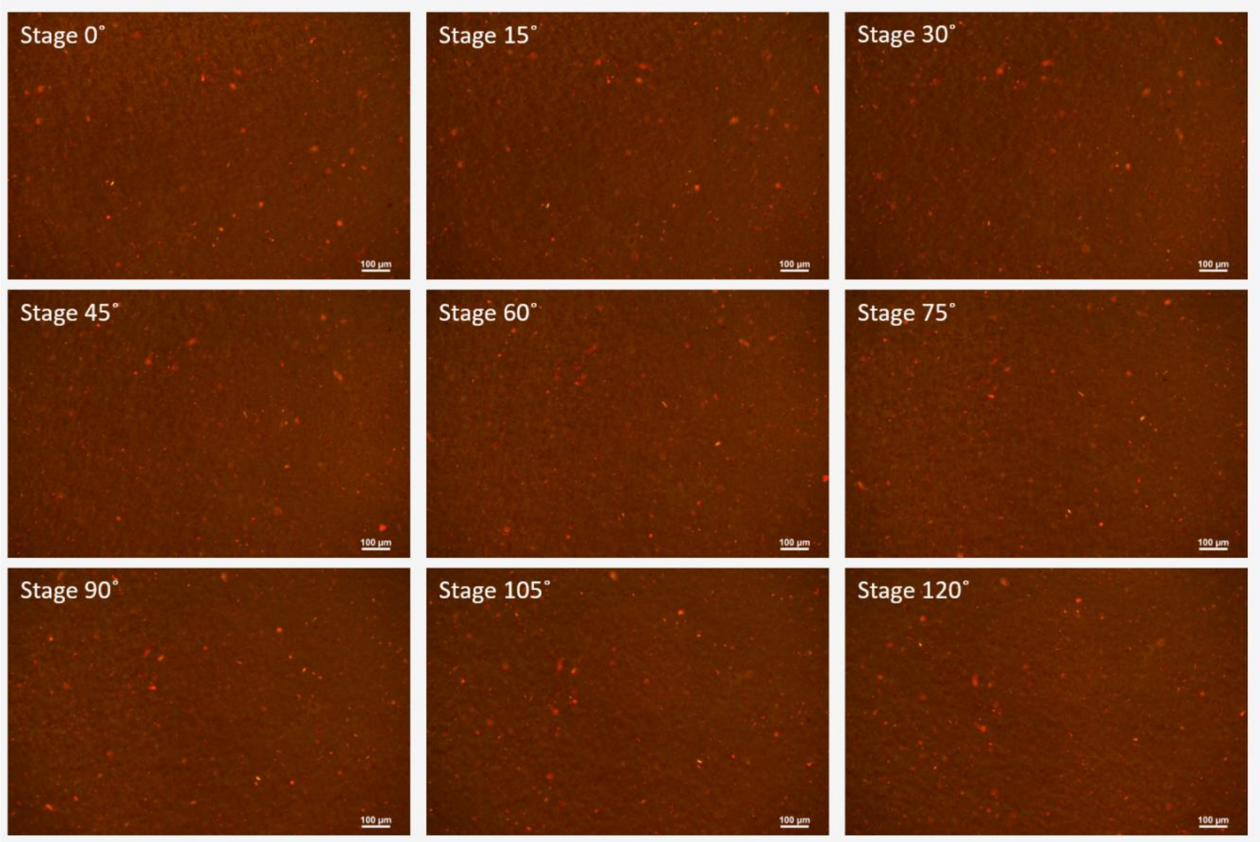

Figure 4.4. MnO_2 NW dispersion with a concentration of 0.22 vol % (1 wt %), imaged as the microscope stage is rotated and using a 10x lens with cross-polarizers.

The sample was then diluted by an order of magnitude to a concentration of 0.02 vol% (0.1 wt %). At this low of a concentration, high magnification images can capture individual bundles of the nanowires, as seen in **Figure 4.5**. A DIC filter was used for these images to better capture the microstructure of the nanowire dispersion. At this concentration, no self-assembly of the nanowires is observed as they appear to be floating bundles in a sea of EG, likely indicating that this is an isotropic dispersion.

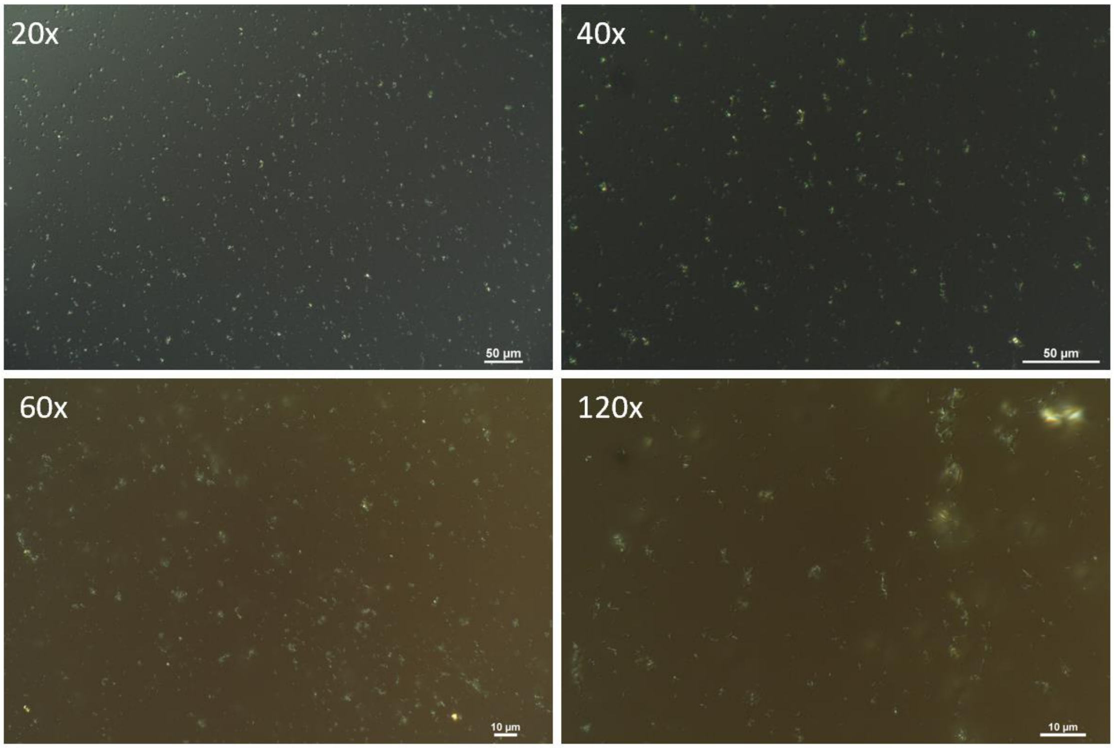

Figure 4.5 MnO_2 NW dispersion with a concentration of 0.02 vol % (0.1 wt %) imaged with cross-polarizers and DIC filter at varying magnifications.

Atomic force microscopy (AFM) was used as another characterization tool for the MnO_2 NW dispersions. AFM images of the MnO_2 NWs showed heavily aggregated samples, as seen in **Figure 4.6**. This degree of aggregation prevented accurate measurements. This aggregation could be due to an “overcooking” of the nanowires during synthesis or due to sample preparation.

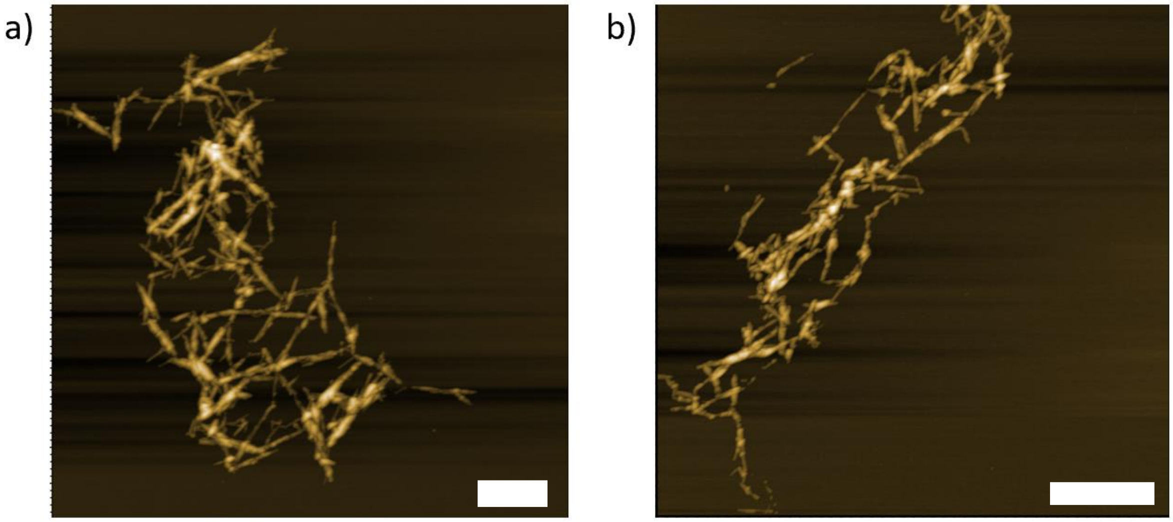

Figure 4.6. AFM measurements of MnO_2 NW dispersion. Scale bars represent 1 nm.

4.3 Copper Nanowires

The main goal of experimental work with Cu NWs was to gain experience with a large-scale synthesis of a nanomaterial under relatively mild conditions. Due to this, only POM was used for the batches of Cu NWs synthesized. **Figure 4.7** displays the results of a synthesized and purified batch of Cu NWs following the reaction parameters of Li et al.[136] Unlike with the MnO_2 NWs, these nanowires can be seen at lower magnification levels. This is due to the predicted longer length of Cu NWs; however, AFM was not used to confirm these dimensions due to the remaining contaminants in the dispersion. A stepwise dilution process to study the phase behavior of the Cu NWs was not used as it was for the MnO_2 NWs since the dispersions appeared to be contaminated with reactant remnants. In **Figure 4.7**, these contaminants are seen as a cloudy material covering the field of view. Underneath this contaminant cloud, some Cu NWs can be seen dispersed throughout the sample. However, better purification techniques are needed in order to more closely observe the self-assembly and phase behavior of these nanowires through POM and other characterization methods.

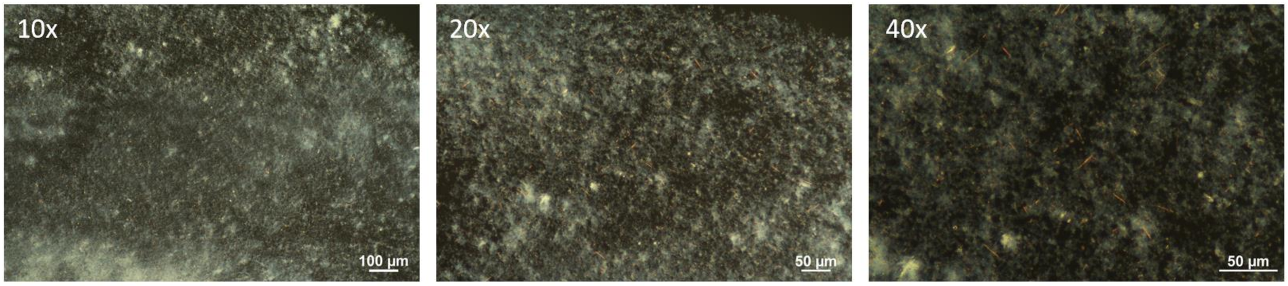

Figure 4.7. POM images of Cu NWs after attempted purification.

4.4 Conclusions

This initial work with MnO_2 NWs has provided the early groundwork necessary for future strategic study to determine the quantitative measures required to experimentally determine the phase behavior of the nanowires in ethylene glycol. By developing a phase diagram of this nanowire system, processability of the nanowires would be enhanced through the knowledge of rheological properties and phase behavior progression as a function of MnO_2 NW concentration. As of the time of writing, MnO_2 NW dispersions have not been experimentally observed to achieve a fully liquid crystalline phase, but it is in the hopes of the future directions of this work that a MnO_2 NW liquid crystal can be achieved.

The research completed in this section provided the necessary experimental skills and introduction into anisotropic self-assembly that are required to progress into investigating a lesser understood and more complex 2D nanomaterial. Synthesis experience with different colloid systems provides a deeper level of understanding into the effects of synthesis parameters, such as reaction temperatures and reactant ratios, on the produced nanomaterial and its properties. Characterization skills, such as polarized optical microscopy, are vital to observing lyotropic liquid crystalline phase transitions. Gaining experience with 1D nanomaterial systems serves to increase understanding of qualitative observations that may not be explicitly clear upon introduction to field of colloid science.

Chapter 5 - Sheet Size Effects on the Rheology and Phase Behavior of Aqueous MXene ($Ti_3C_2T_x$) Dispersions

5.1 Motivation

The aspect ratio of a rigid nanomaterial is a key determinant in the dispersion phase behavior. In Onsager's 1949 seminal theory of hard rod interactions and lyotropic liquid crystalline formation, the critical phase transition calculations were dependent only on excluded volume interactions.[40] According to this theory, rigid anisotropic nanomaterials (or mesogens) with smaller aspect ratios require higher concentrations to reach aligned liquid crystalline phases. Aspect ratio for a 1D (or cylindrical) mesogen is defined as the length of the mesogen divided by the diameter. In the field of 2D nanomaterials, this ratio is typically defined as the longest lateral dimension of the sheet (L) divided by the thickness of the sheet (D). Though the effects of adjusting aspect ratio have been studied for many systems of rod-like mesogens, there are limited similar studies in the field of 2D nanomaterials. Jalili et al.'s investigation of size effects on the phase behavior and rheology of aqueous GO dispersions is one of the most notable to date.[14] Their results provided insight into the formation of liquid crystalline dispersions consisting of large 2D sheets, as well as the utilization of selective polydispersity to induce liquid crystallinity at lower concentrations. Recently, Zhang et al.[23] confirmed that aqueous $Ti_3C_2T_x$ MXenes could form lyotropic liquid crystalline phases and that the phase boundaries were dependent on the sheet size. It was also shown that these liquid crystalline phases could be spun into highly aligned additive free fibers. The fiber properties could be then tuned through the tailoring of MXene dispersion properties.

This research expands upon the current understanding of size effects on the phase behavior and associated rheological properties of 2D nanomaterials by investigating three types of size fractionated $Ti_3C_2T_x$ MXene dispersions: 1) Large MXene dispersions (denoted as L-MXenes), with average sheet sizes of 3 μm, 2) small MXene dispersions (denoted as S-MXenes), with average sheet sizes of 0.3 μm, and 3) bimodal dispersions (denoted as B-MXenes) consisting of large and small MXene sheets in a 1:1 volume ratio. Steady shear and small amplitude oscillatory shear (SAOS) rheology were used in conjunction with polarized optical microscopy (POM) to investigate changes in rheological properties, viscoelasticity, and microstructure as a function of MXene concentration. This work highlights the impacts of sheet size on dispersion microstructure, aggregation tendency, and rheological properties. The knowledge gained from this work can be directly translated into improvements in MXene processability and overall performance of MXene-based devices.

5.2 Results

5.2.1 MXene Characterization

Like many other 2D colloids, MXenes are polydisperse. After the synthesis and etching process, individual MXene sheets can range from nanometers to microns in length. Additionally, the synthesized MXene sheets display severe shape irregularity. The focus of this work was to separate the MXene sheets by largest lateral dimension to study the effects that size fractionation might have on dispersion properties. AFM was used to confirm the size separation of large MXene sheets from small MXene sheets. **Figure 4.1** shows AFM measurements and size distributions for both large and small MXene sheets. Measurements on MXene sheets from each batch used in this work, for a total of 150 large and 50 small sheets, found that average lateral dimension was $\langle L \rangle$ = 2.86 ± 1.16 μm and $\langle L \rangle$ = 0.33 ± 0.19 μm, respectively, with error reported as standard error. For all samples the average sheet thickness was $\langle D \rangle$ = 2.05 ± 0.41 nm.

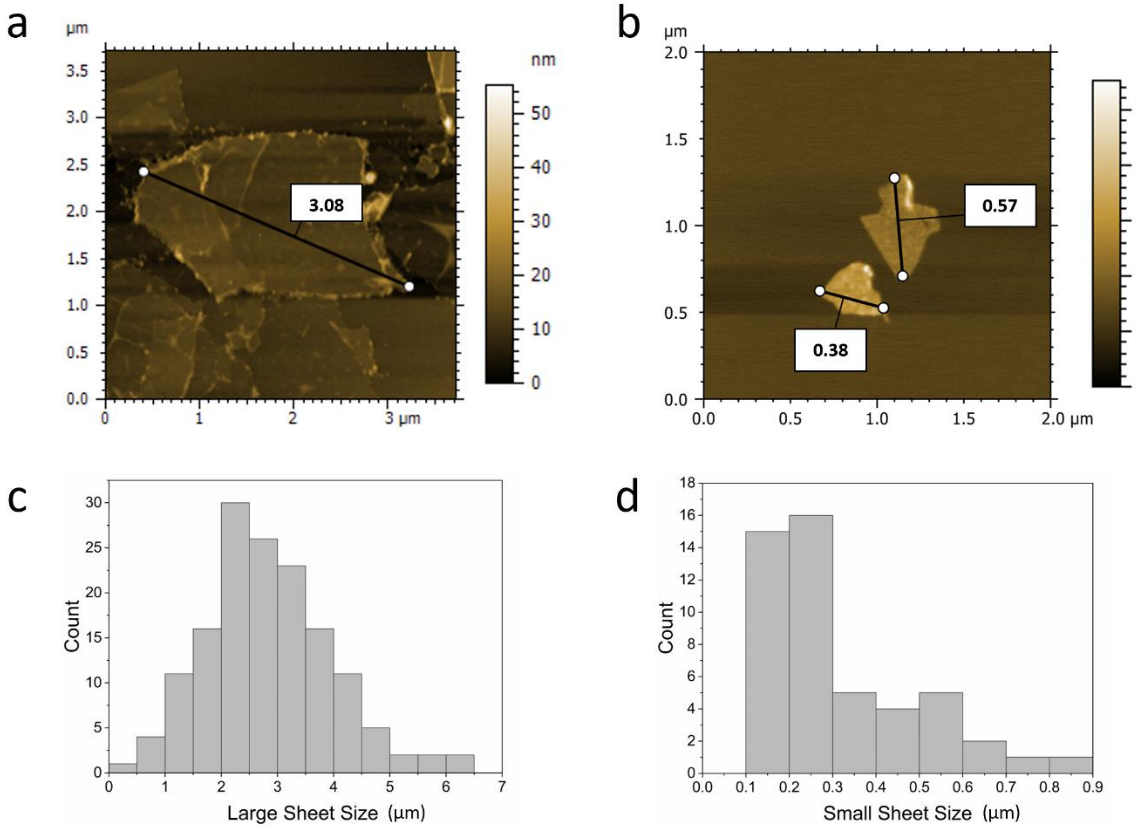

Figure 5.1. Atomic force microscopy (AFM) images of (a) large MXenes and (b) small MXenes, and size distribution of (c) large MXene sheets and (d) small MXene sheets.

5.2.2 Large MXenes

Previous reports of 2D nanomaterial phase behavior state that size fractionated large sheets, or platelets, will readily form liquid crystalline alignment at relatively low concentrations.[14, 23] Due to the complexity of MXenes, with their irregular shape and charged surfaces, experimental investigation of size fractionated large MXenes (L-MXenes) extended across a range of concentrations from 0.05 vol % - 1.75 vol %. Opacity of the L-MXene samples prevented use of optical microscopy at concentrations greater than 1.75 vol %. **Figure 5.2** depicts the steady shear and oscillatory shear for all L-MXene dispersions in this work – these comprehensive plots allow for an overview of changes in rheological properties as L-MXene concentration was increased. Detailed discussion and rheological plots of specific concentrations follows.

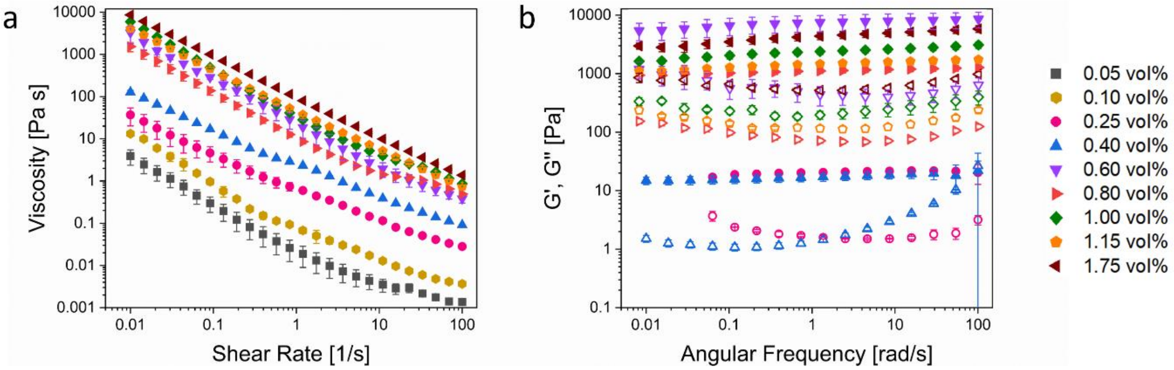

Figure 5.2. a) Steady shear rheology and b) oscillatory rheology of all L-MXene dispersions investigated in this work. Filled symbols in b) represent G' and hollow symbols represent G''. Error bars represent standard error of three to four runs.

Utilizing modifications to Onsager theory[40] to account for polydisperse sheets the theoretical biphasic ϕ_I and liquid crystalline ϕ_{LC} phase boundaries were calculated using:[139]

$$\phi_I = 2.7\frac{D}{L} \tag{20}$$

$$\phi_{LC} = 3.9\frac{D}{L} \tag{21}$$

where D is the thickness of the sheets and L is their lateral length. A more detailed discussion of the theoretical calculations can be found in Chapter 3. The theoretical transitions for large MXene sheets were calculated to be Φ_I = 0.20 vol % (10.2 mg/mL) and Φ_{LC} = 0.29 vol % (14.7 mg/mL). Based on this, two L-MXene dispersions in the predicted isotropic phase were investigated: 0.05 vol % and 0.10 vol %.

Cross-polarized optical microscopy using a 60x objective oil immersion objective and 2x magnification in front of the camera showed scattered birefringent structures in the 0.05 vol % L-

MXene (**Figure 5.3a**), indicating that this dispersion contained regions of alignment. At the slightly higher concentration of 0.10 vol %, the diffuse birefringent domains seen in the 0.05 vol % dispersions increased in concentration and evolved to form more extended structures that appeared to weave in and out of the focal plane (**Figure 5.3b**). Based on these observations, the aqueous L-MXene dispersions transitioned from isotropic to biphasic at a concentration slightly less than 0.05 vol %, approximately 4x lower than the theoretical value. Similar discrepancies are common throughout the literature on lyotropic liquid crystals comprised of anisotropic nanomaterial mesogens. Theoretical models for mesogens with continuous size distributions were not even developed until 2003 and are still evolving.[40] In the case of 2D nanomaterials, efforts to capture polydispersity effects typically rely on measurements of each sheet's longest lateral dimension and fail to account for account for shape irregularity or shape wrinkling.[2, 53] Moreover, phase behavior is also heavily influenced by nanomaterial-nanomaterial and nanomaterial-solvent interactions. In the case of charged 2D nanomaterials such as MXenes, the role of thermodynamic interactions is particularly complex since size distribution can affect the potential for edge-edge, face-face, and face-edge electrostatic interactions.

Steady shear rheology of these two dispersions resulted in poor fits to the Herschel-Bulkley Model (**Figure 5.3c**). It is noted that in the absence of a significant yield stress the Herschel-Bulkley model reduces to a power-law model. **Table 5.1** shows the Herschel-Bulkley parameters of all L-MXene dispersions in this work. Viscosity of the 0.05 vol % dispersion approached that of the solvent at high shear. The yield stress (**Figure 5.3d**) of both of these dispersions were near 0, indicating that these dispersions approached the behavior of a power-law fluid; however, their shear thinning behavior from 0.01 – 100 s-1 prevented true power law behavior. These two dispersions lacked measurable G’ and G” within the instrument limitations, making accurate oscillatory measurements impractical to obtain.

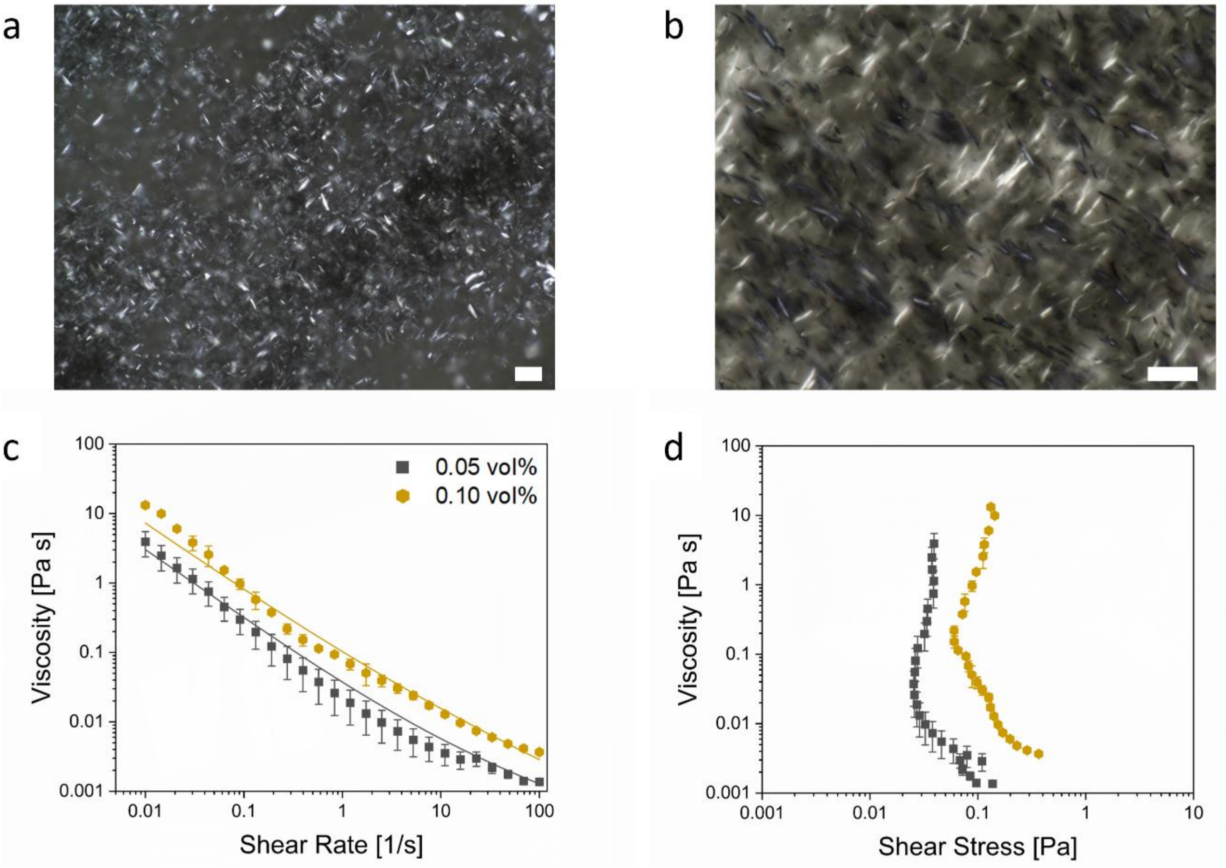

Figure 5.3. POM of a) 0.05 vol % and b) 0.10 vol % L-MXenes. Scale bars represent 10 μm. c) Flow curves and d) yield stresses of 0.05 vol % (black squares) and 0.10 vol % (gold hexagons). Error bars represent standard error of three to four runs.

At 0.25 vol % and 0.40 vol %, the flow curves exhibited a narrow plateau hesitation point between two regions with different slopes resulting in a three region flow curve (**Figure 5.4**). Similar behavior has been observed in biphasic and liquid crystalline dispersions of several 1D nanomaterials[49, 68, 141, 142] and is believed to be analogous to the three region behavior first identified by Onogi and Asada for lyotropic liquid crystalline polymers.[64] Frequently, the extended Region II viscosity plateau observed in lyotropic liquid crystalline polymers is not seen in nanomaterial liquid crystalline dispersions. Rather, in these dispersions Region II is often limited to a very short plateau or even a hesitation point, as observed in dispersions of single walled carbon nanotubes in sulfuric acid, cellulose nanocrystals in water, and silver nanowires in ethylene glycol.[49, 68, 141] When fitting the rheology data of this concentration to the Herschel-Bulkley model, the data was fitted in two sections: the low shear region before the viscosity hesitation (denoted as Region 1) and the high shear region after (denoted as Region 3, to maintain consistency with three-region behavior). The results of this divided model fitting showed that there were slight changes in the Herschel-Bulkley parameters (**Table 5.1**), indicating different flow behavior before and after the Region II viscosity hesitation.

	Region 1			**Region 3**		
L-MXene vol %	Yield Stress (Pa)	K (Pa s^n)	n	Yield Stress (Pa)	K (Pa s^n)	n
0.05	0.03	0.008	0.55	-	-	-
0.10	0.07	0.04	0.39	-	-	-
0.25	0.36	0.29	0.73	0.66	0.11	0.64
0.40	1.22	0.94	0.51	2.13	0.58	0.54
0.60	24.19	0.12	1.00	-	-	-
0.80	11.39	1.13	0.79	-	-	-
1.00	42.24	0.63	0.96	-	-	-
1.15	38.73	6.95	0.36	-	-	-
1.75	85.84	0.99	0.50	-	-	-

Table 5.1. Herschel-Bulkley parameters of all L-MXene dispersions investigated through rheology.

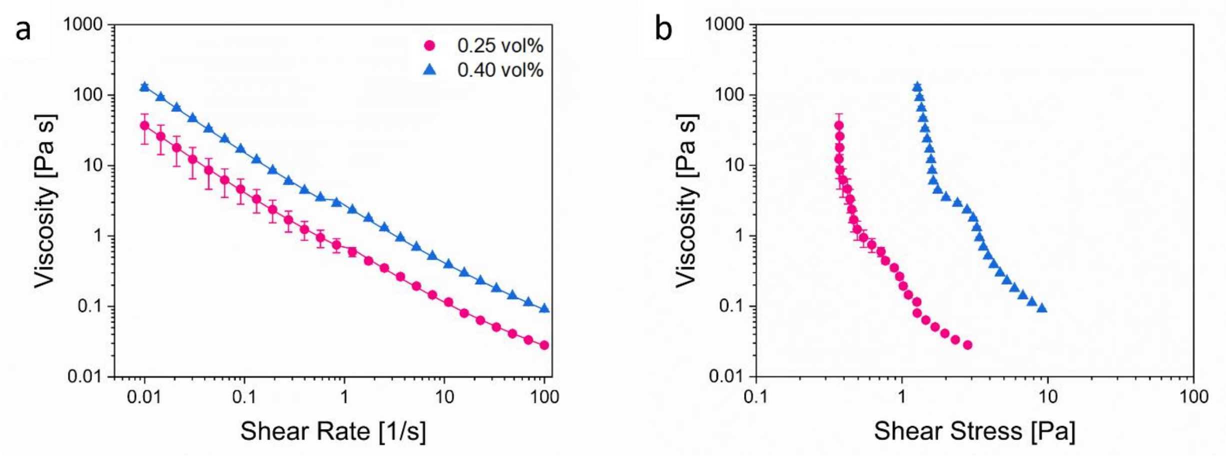

Figure 5.4. a) Flow curves and b) yield stresses of 0.25 vol % (pink circles) and 0.40 vol% (blue triangles) L-MXenes.

POM of 0.25 vol % (**Figure 5.5**) showed extended, woven birefringent textures and small isotropic regions that were only visible at 120x magnification. **Figure 5.5a** shows dark domains of a purple-blue color stretched from the top left corner of the field of view to the bottom right corner. When the stage was rotated to 90°, seen in **Figure 5.5b**, these dark woven regions became brighter domains with a brush-like structure in the opposite direction to the dark threads. In addition, brush-like Schlieren textures appeared – confirming nematic liquid crystalline phase formation.[143] The presence of Schlieren textures and the observable birefringence that extends across the dispersion confirmed that the aqueous L-MXenes dispersions were a nearly complete liquid crystalline at 0.25 vol %, which is slightly lower than the theoretical calculation of Φ_{LC} = 0.29 vol % (14.7 mg/mL). Isotropic regions persisted as the L-MXene concentration increased to 0.40 vol %, with dispersion microstructure remaining relatively unchanged (**Figure 5.5c,d**). Non-cross-polarized images of these two dispersions clearly show the similarities in microstructure (**Figure 5.5e,f**).

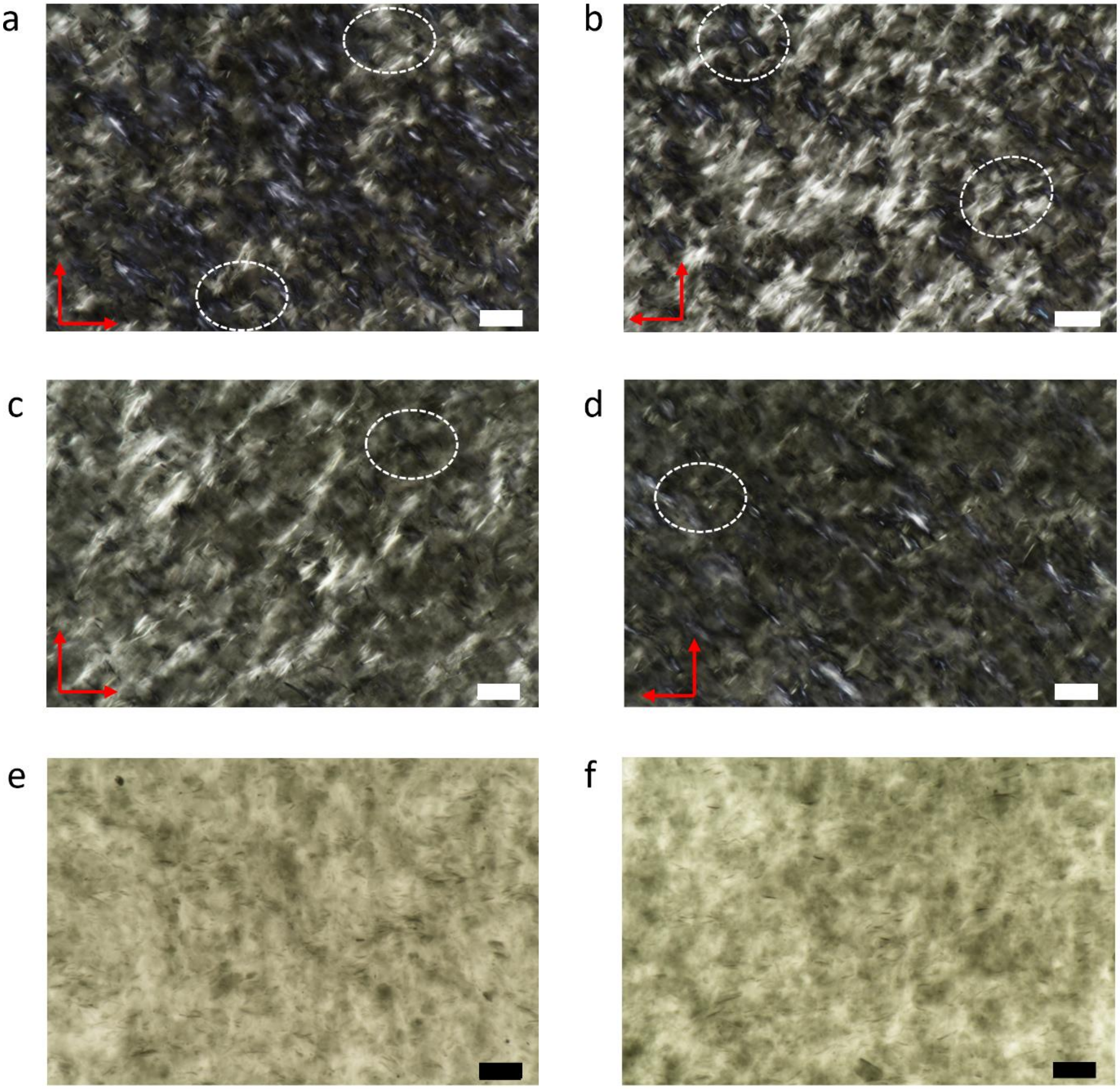

Figure 5.5. POM of 0.25 vol % L-MXenes at a) 0° stage rotation and b) 90° stage rotation. POM of 0.40 vol % L-MXenes at c) 0° stage rotation and d) 90° stage rotation. Non-cross-polarized images of e) 0.25 vol % and f) 0.40 vol % L-MXenes. Scale bars represent 10 µm.

Oscillatory rheology of 0.25 vol % and 0.40 vol % L-MXenes resulted in similar viscoelastic properties (**Figure 5.6**). It should be noted that torque limitations on the instrument prevented obtaining measurements of the 0.25 vol % dispersion at low angular frequencies. The storage modulus (G', represented with filled symbols in **Figure 5.6a**) of both dispersions was relatively independent of angular frequency. This behavior suggested that a percolated, or continuous, network had formed in the dispersion. The non-cross-polarized images in **Figure 5.5** support that this is likely the case. Though some isotropic regions remained, the network of MXenes was homogeneously dispersed and a continuous microstructure extended across the field of view. Despite the low volume fractions of these two dispersions, the large size of the MXene sheets aided in the formation of an extended colloidal network. From oscillatory measurements, tanδ can be obtained. This is the ratio of the G'' to G' and provides insight into how viscous or elastic a dispersion is. At tanδ < 1, the dispersion is more elastic, which is desirable in many forms of fluid-phase processing. In **Figure 5.6b**, it can be seen that tanδ of the 0.40 vol % L-MXene dispersion approached 1 at higher angular frequencies, indicating an increase in viscous behavior. This can also be seen in the steady increase in G'' at higher frequencies. Though error was significant in the 0.40 vol % measurements at 100 rad/s, a crossover point (in which G'' became greater than G') was observed. This suggests that at high frequencies, or short timescales, the MXenes within the dispersion have more mobility and behavior becomes more liquid-like.

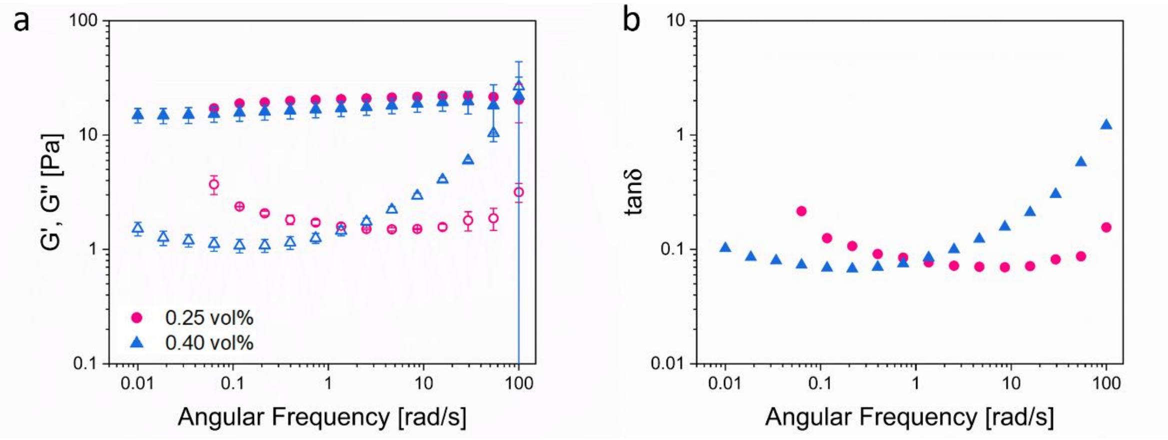

Figure 5.6. a) Storage and loss moduli and b) tanδ of 0.25 vol % (pink circles) and 0.40 vol % (blue triangles) L-MXenes. Filled symbols represent G' and hollow symbols represent G''. Error bars are standard error of three to four runs.

Increasing the L-MXene concentration to 0.60 vol % did not result in a complete liquid crystal; rather, dense flocs or aggregates began to form throughout the dispersion resulting in a two-phase, highly defected polydomain structure (**Figure 5.7a,b**). Cross-polarized microscopy showed this dispersion consisted of a birefringent network surrounding dense flocs or aggregates which we denoted as a nematic gel-aggregate phase. **Figure5.7b** shows the size of the flocs/aggregates in the 0.60 vol % L-MXenes under non-cross-polarized light, where some aggregates reached nearly 10 μm in diameter. The presence of these large structures highlights the importance of performing rheological testing and imaging samples in parallel. Increasing the concentration to 0.80 vol %, 1.00 vol %, and 1.15 vol % resulted in large aggregates in closer packing alignment (**Figure 5.7c-f**). Isotropic regions that had drastically increased with the appearance of the large aggregates decreased in size with increasing MXene content. Birefringent textures and scattered thread-like domains remained in these dispersions, suggesting nematic ordering.

Studying the steady shear viscosity behavior and the viscoelastic properties of the dispersions assisted in determining the progression from the liquid crystalline phase to a gel phase. Three main rheological signatures were used to determine this transition: (1) the viscosity of the dispersions does not increase as dramatically as it does when in and transitioning between the isotropic, biphasic, and liquid crystal regions; therefore, viscosity versus concentration curves show a plateauing of the viscosity once the gel phase has been reached, (2) the storage modulus (G') tends to become independent of frequency once the dispersion has entered the gel phase,[102] and (3) once a gel, the aligned dispersion forms smaller monodomains which results in a drastic increase in the storage modulus and complete distinction between the storage and loss moduli.[102]

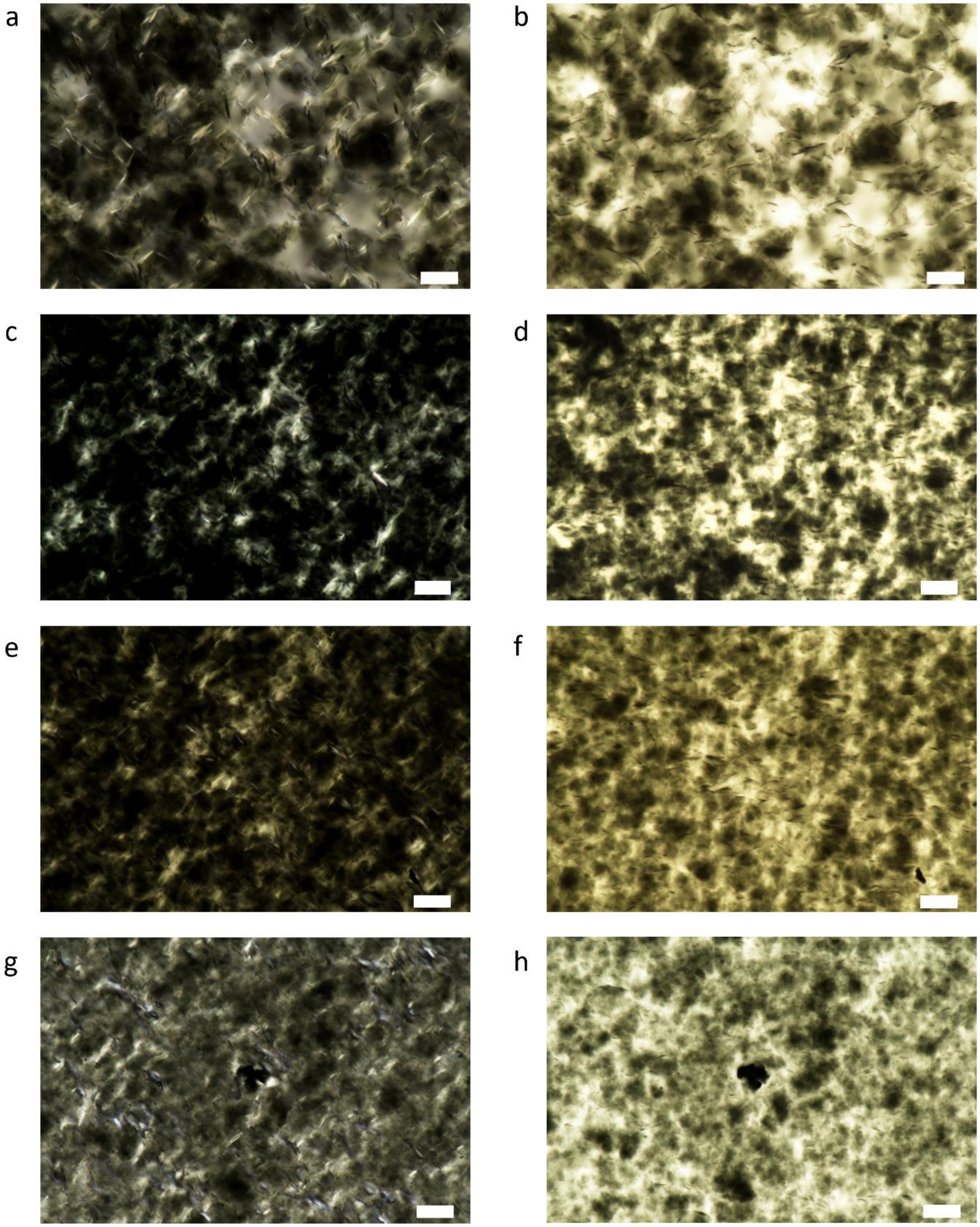

Figure 5.7. a) Cross-polarized and b) non-cross-polarized microscopy of 0.60 vol % L-MXenes. c) Cross-polarized and d) non-cross-polarized microscopy of 0.80 vol % L-MXenes. e) Cross-polarized and f) non-cross-polarized microscopy of 1.00 vol % L-MXenes. g) Cross-polarized and h) non-cross-polarized microscopy of 1.15 vol % L-MXenes. Scale bars represent 10 μm.

Figure 5.8 depicts the rheology data for the more highly concentrated L-MXene dispersions. For all these dispersions, G’ was greater than G” with G’ having little dependence on frequency. This indicates the behavior was dominated by a percolated network of L-MXenes. A significant increase in viscosity and G’ occurred at 0.60 vol% compared to the lower concentrations in **Figure 5.4** and **Figure 5.6**, suggesting that a gel phase was achieved at this concentration of L-MXenes. Interestingly, this was also the concentration threshold for large flocs or aggregates in L-MXene dispersions. Due to the continued presence of birefringent domains in the aggregated dispersions, the gel contains nematic ordering and so is classified as a two-phase nematic gel. Aggregation was also observed through higher concentrations of L-MXenes, suggesting that the nematic gel-aggregate phase persisted. The aggregates did not appear to dramatically alter the apparent rheological behavior in terms of the shapes of the flow curves and moduli versus frequency curves.

Figure 5.8c shows the change in low shear viscosity and low frequency G’ as a function of MXene concentration. As expected for a gel, the degree to which viscosity increased with MXene concentration lessened. Though G’ significantly increased at 0.60 vol %, as expected once the gel phase was reached, the following G’ values decreased to a variable plateau at higher volume percents. This is notable since low shear viscosity and yield stress showed similar albeit less pronounced behavior. In lyotropic systems such non-monotonic behavior is often attributed to the fraction of the aligned liquid crystalline phase increasing with concentration. However, in this case it may be due to the interplay between nematic alignment and floc formation. The partially cross-polarized and non-cross-polarized image, respectively, of a 0.80 vol % (3.99 wt %) L-MXene dispersion in **Figure 5.7c,d** shows there is a more continuous structure with less aggregation and more birefringent domains than in the 0.60 vol % dispersion. This suggests the decrease in storage modulus of L-MXene dispersions above 0.60 vol % could be attributed to a gain in nematic ordering over aggregation within the nematic gel-aggregate phase.

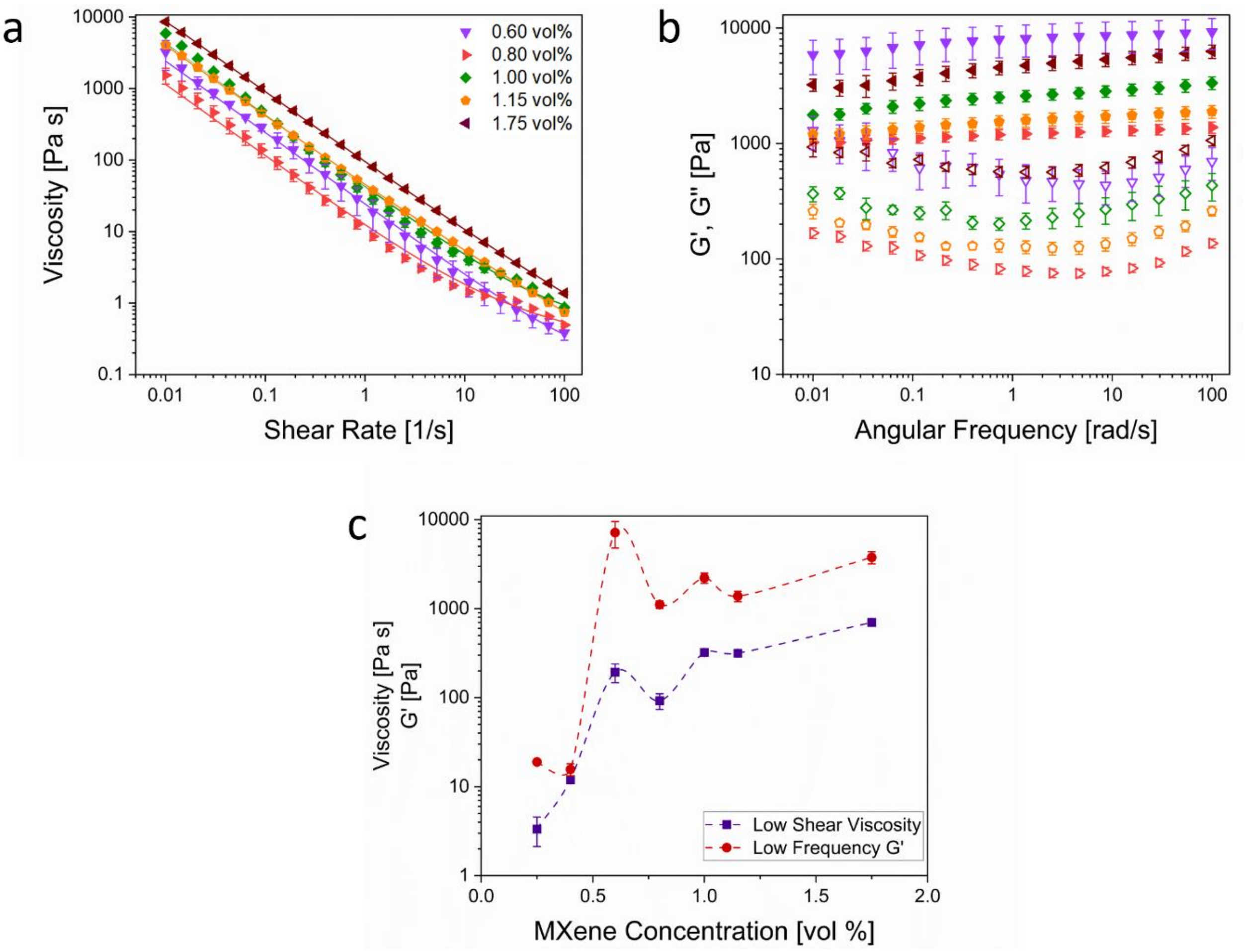

Figure 5.8. a) Steady shear rheology of L-MXene dispersions at 0.60 vol % (purple upside-down triangles), 0.80 vol % (red right triangles), 1.00 vol % (green diamonds), 1.15 vol % (orange pentagons), and 1.75 vol % (maroon left triangles). b) Oscillatory rheology of L-MXenes, with filled symbols representing G' and hollow symbols representing G''. Legend following that of a). c) Low shear viscosity and low frequency G' as a function of MXene concentration. Error bars represent standard error of three to four runs.

5.2.3 Small MXenes

Based on fundamental colloid science, it is expected that 2D nanomaterials with smaller aspect ratios will require much greater concentrations to reach a liquid crystalline phase. This has been observed experimentally in preliminary size fractionated MXene studies.[23] Other literature on size fractionated 2D nanomaterials suggests that sheets with smaller lateral dimensions may remain in an isotropic phase even at high volume fractions.[14] Theoretical calculations of critical phase transitions of the small MXene sheets used in this work resulted in Φ_I = 2.00 vol % (89.2 mg/ml) and Φ_{LC} = 3.13vol % (128.9 mg/ml) from Equations 9-10. These predicted phase transition concentrations were an order of magnitude greater than those for the large MXenes in this work, which is similar to the results of early MXene phase behavior research by Zhang et al.[23] For this work, S-MXene dispersions ranging from 0.05 vol % - 2.00 vol % were investigated. **Figure 5.9** depicts the steady shear and oscillatory rheology of all S-MXene dispersions investigated in this work.

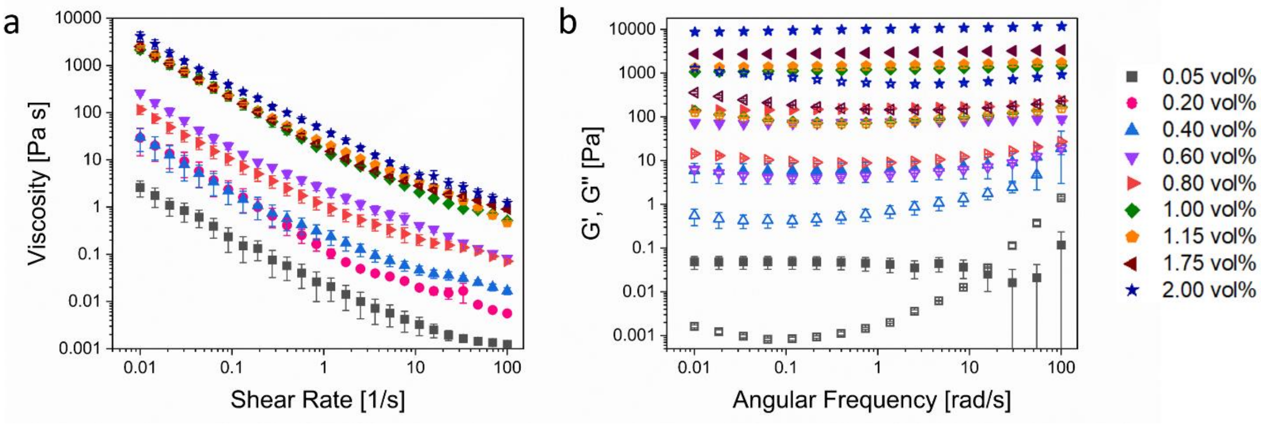

Figure 5.9. a) Steady shear and b) oscillatory rheology of all S-MXene dispersions studied in this work. Filled symbols in b) represent G' and hollow symbols represent G''. Error bars represent standard error of three to four runs.

At 0.05 vol %, the high shear viscosity approached that of the solvent beginning around 50 s^{-1}, due in part to the low MXene content of this dispersion (**Figure 5.10a**). When fitted to the Herschel-Bulkley model, the yield stress of the dispersion was near 0 (**Table 5.2**). Cross-polarized microscopy revealed that the image was completely dark and no structure was observed; this indicates the dispersion was fully isotropic. At a concentration of 0.20 vol %, the high shear viscosity was still over a magnitude greater than that of water. The birefringence in the partially cross-polarized microscopy images of the 0.20 vol % dispersion showed that the S-MXenes had progressed into the biphasic region (**Figure 5.10b**); this concentration is an order of magnitude lower than the theoretical prediction of $\Phi_I = 2.00$ vol % (9.55 wt %, 88.7 mg/ml). This is attributed to both the irregular shapes of the S-MXenes as well as thermodynamic interactions. Compared to the microstructure of the L-MXene dispersions, the S-MXene dispersions displayed a much finer morphology, and no extended woven textures were observed. However, close inspection of the microstructure revealed slight birefringence. Further increase in S-MXene concentration to 0.40 vol % resulted in an increase in high shear viscosity from ~0.05 Pa s to ~0.1 Pa s, though low shear behavior remained similar to that of the 0.20 vol % dispersion. Cross-polarized microscopy revealed an increase in birefringence in anisotropic regions, though long-range domain alignment was still not observed (**Figure 5.10c,d** with sample birefringent regions highlighted). Large areas of isotropic phase extended throughout the dispersion, indicating the S-MXenes remained in a biphasic region with a high fraction of isotropic phase.

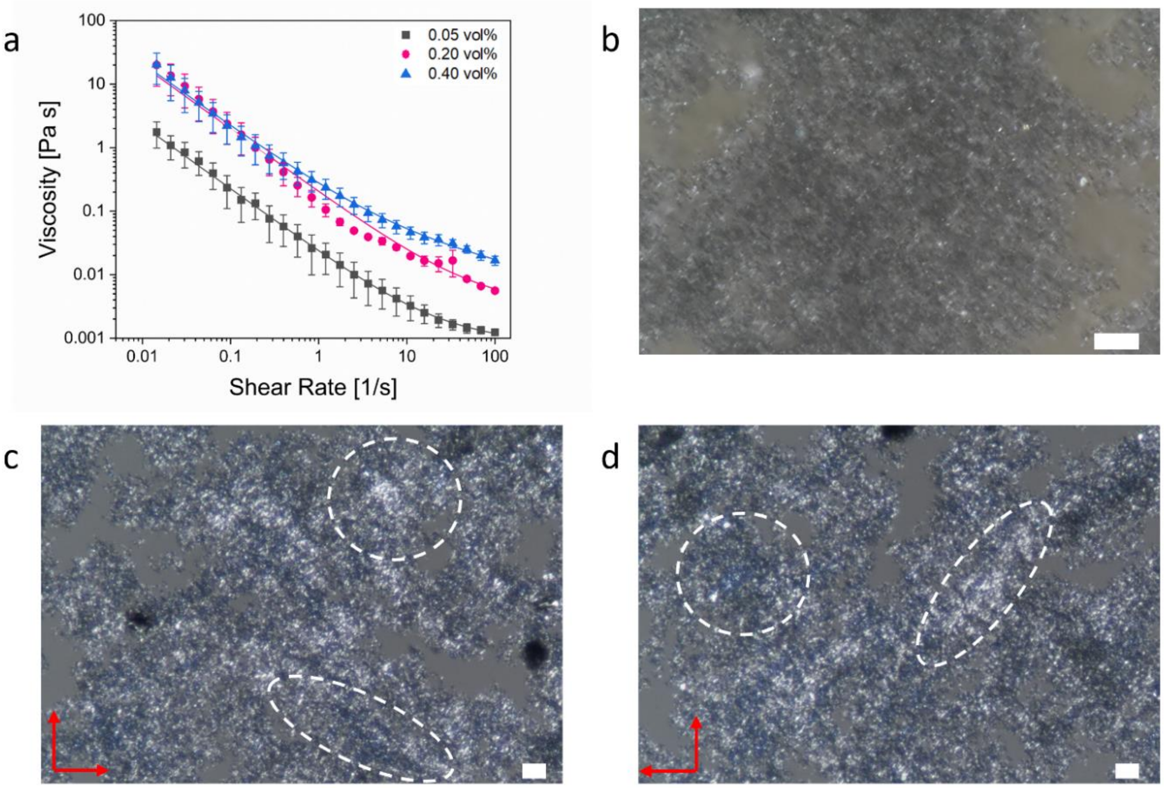

Figure 5.10. a) Flow curves of S-MXene dispersions at 0.05 vol % (black squares), 0.20 vol % (pink circles), and 0.40 vol % (blue triangles). Error bars represent standard error of three to four runs. b) Cross-polarized microscopy of 0.20 vol % S-MXenes. c) Cross-polarized microscopy of 0.40 vol % at 0° stage rotation and d) 90° stage rotation. Dashed circles high regions of birefringence. Scale bars represent 10 µm.

Beyond the clear transition from isotropic to biphasic due to the emergence of observable aligned domains, the change in phase of S-MXene dispersions was more difficult to detect than with the L-MXene dispersions. In the viscosity versus shear rate graph (**Figure 5.11a**), S-MXenes only exhibited a possible viscosity hesitation at intermediate shear rates for 0.60 vol %. POM of this dispersion suggests the formation of a highly defective liquid crystal; again, the phase transition occurred at a much lower concentration than the theoretical prediction of at a much lower concentration than theoretical prediction of Φ_{LC} = 3.13vol % (14.3 wt %, 128.0 mg/ml). This is again likely due to a combination of irregular size and shape along with thermodynamic interactions. The higher concentration needed for liquid crystal phase formation of S-MXenes compared to L-MXenes is consistent with both theory and investigations of size fractionated

MXenes by Zhang et al.[23] Partially cross-polarized microscopy of the 0.60 vol % and 0.80 vol % dispersions showed that S-MXenes displayed a significantly different microstructure from the L-MXenes (**Figure 5.11b-f**). Although the difference in microstructure compared to L-MXenes is not fully understood, studies of size fractionated graphene oxide dispersions found that this finer microstructure occurred only in small sheet dispersions.[144] Interestingly, a woven structure similar to that seen in multiple L-MXene dispersions was observed in the 0.80 vol % S-MXene dispersion but not at any other concentration. Rotation of the microscope stage underneath the partially polarized light revealed that the woven domains were birefringent (**Figure 5.11c,d**), though the Schlieren textures of the liquid crystalline L-MXene dispersions were not observed. Additional research using methods such as Rheo-SAXS would better clarify the origin of the microstructures observed in the S-MXene dispersions.

	Region 1			**Region 3**		
S-MXene vol %	Yield Stress (Pa)	K (Pa s^n)	n	Yield Stress (Pa)	K (Pa s^n)	n
0.05	0.02	0.002	0.91	-	-	-
0.20	0.20	0.008	0.85	-	-	-
0.40	0.21	0.07	0.68	-	-	-
0.60	1.99	0.32	0.99	3.03	0.49	0.51
0.80	0.85	0.36	0.64	-	-	-
1.00	19.13	0.44	0.96	-	-	-
1.15	18.64	6.95	0.34	-	-	-
1.75	19.35	1.91	0.80	-	-	-
2.00	36.77	4.77	0.64	-	-	-

Table 5.2. Herschel-Bulkley parameters of all S-MXene dispersions investigated through rheology.

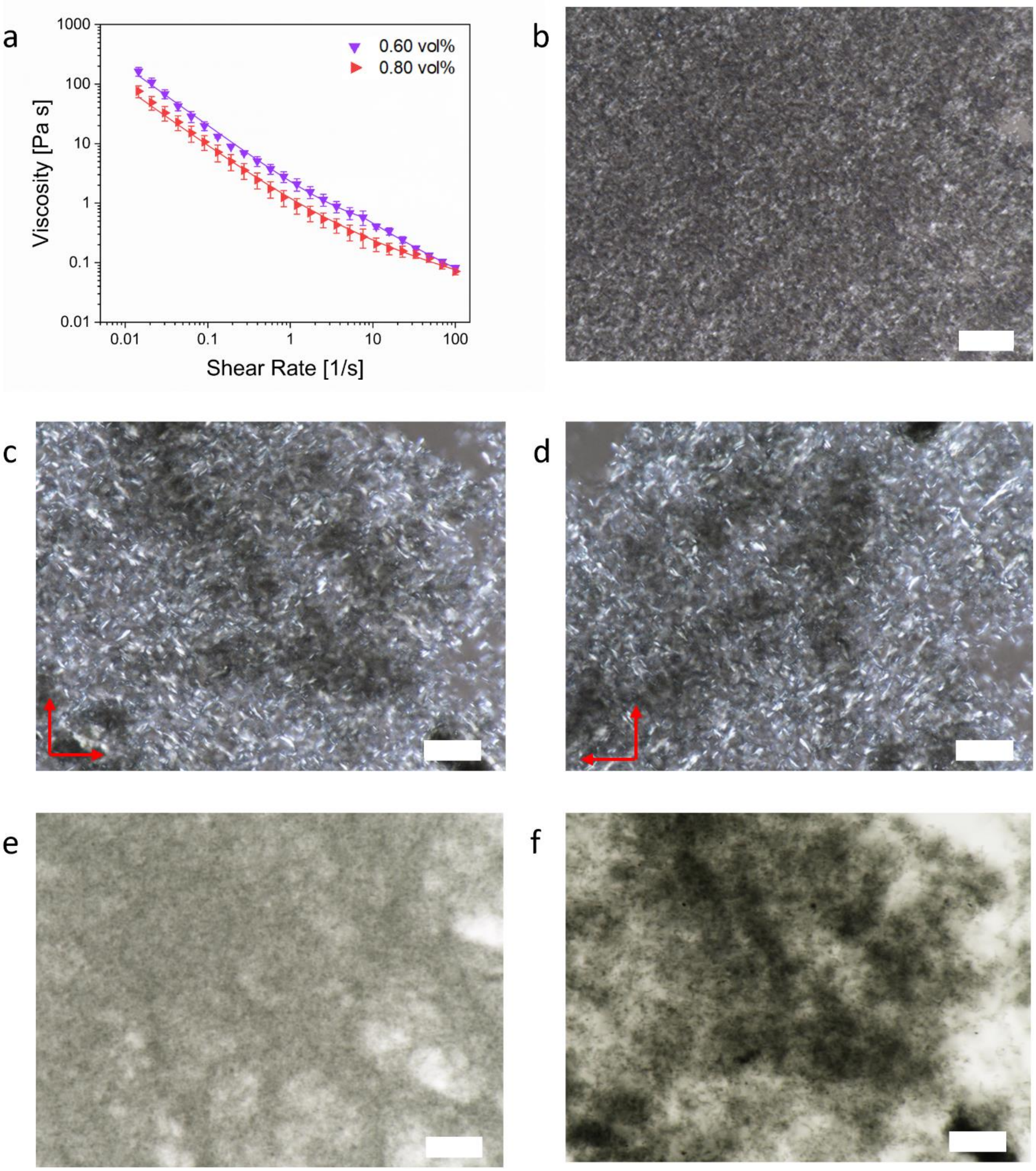

Figure 5.11. a) Flow curves of S-MXene dispersions at 0.60 vol % (purple upside-down triangles) and 0.80 vol % (red right triangles). Error bars represent standard error of three to four runs. b) Cross-polarized microscopy of 0.60 vol %. c) Cross-polarized microscopy of 0.80 vol % at 0° stage rotation and d) 90° stage rotation. e) Non-cross-polarized microscopy of 0.60 vol %. f) Non-cross-polarized microscopy of 0.80 vol %. Scale bars represent 10μm.

Viscosity increased by about an order of magnitude when S-MXene concentration was increased to 1.00 vol %, with little variation as concentration was increased further up to 2.00 vol % (**Figure 5.12a**). For example, low shear viscosity increased from ~250 Pa s to ~2500 Pa s to ~4000 Pa s with concentration increases from 0.60 vol % to 1.00 vol % to 2.00 vol %, respectively. The progression of viscoelastic properties was not as evident in the S-MXenes as it was for the L-MXenes. The storage modulus increased by about an order of magnitude from 0.40 vol % to 0.60 vol % with another order of magnitude increase from 0.80 vol % to 1.00 vol % (**Figure 5.12b**). All dispersions with 0.60 vol % S-MXenes or greater exhibited G' behavior of a percolated network, due to the frequency independence (**Figure 5.12c**). However, it was a concentration of 1.00 vol % S-MXenes that the low shear viscosity, yield stress, and storage modulus of the S-MXenes all plateaued (**Figures 5.12d**), indicating the gel phase transition. Partially cross-polarized images showed that the S-MXenes remained slightly birefringent at 1.00 vol % and 1.75 vol %, suggesting a nematic liquid crystal gel phase (**Figure 5.12e,f**). Opacity of the 2.00 vol % S-MXene dispersion prevented obtaining cross-polarized microscopy images of the samples; however, due to the similarity in rheological properties with concentrations of 1.00 vol % - 1.75 vol %, it is likely that a nematic gel phase persists. As with the prior phases of the S-MXenes, the gel-phase microstructure differed greatly from the L-MXenes with no apparent long-range alignment or positional ordering. The visible aligned domains in the polarized images of the flocculated or aggregated nematic gel L-MXenes were not observed in the nematic gel S-MXenes, though notably, little to no flocculation was observed.

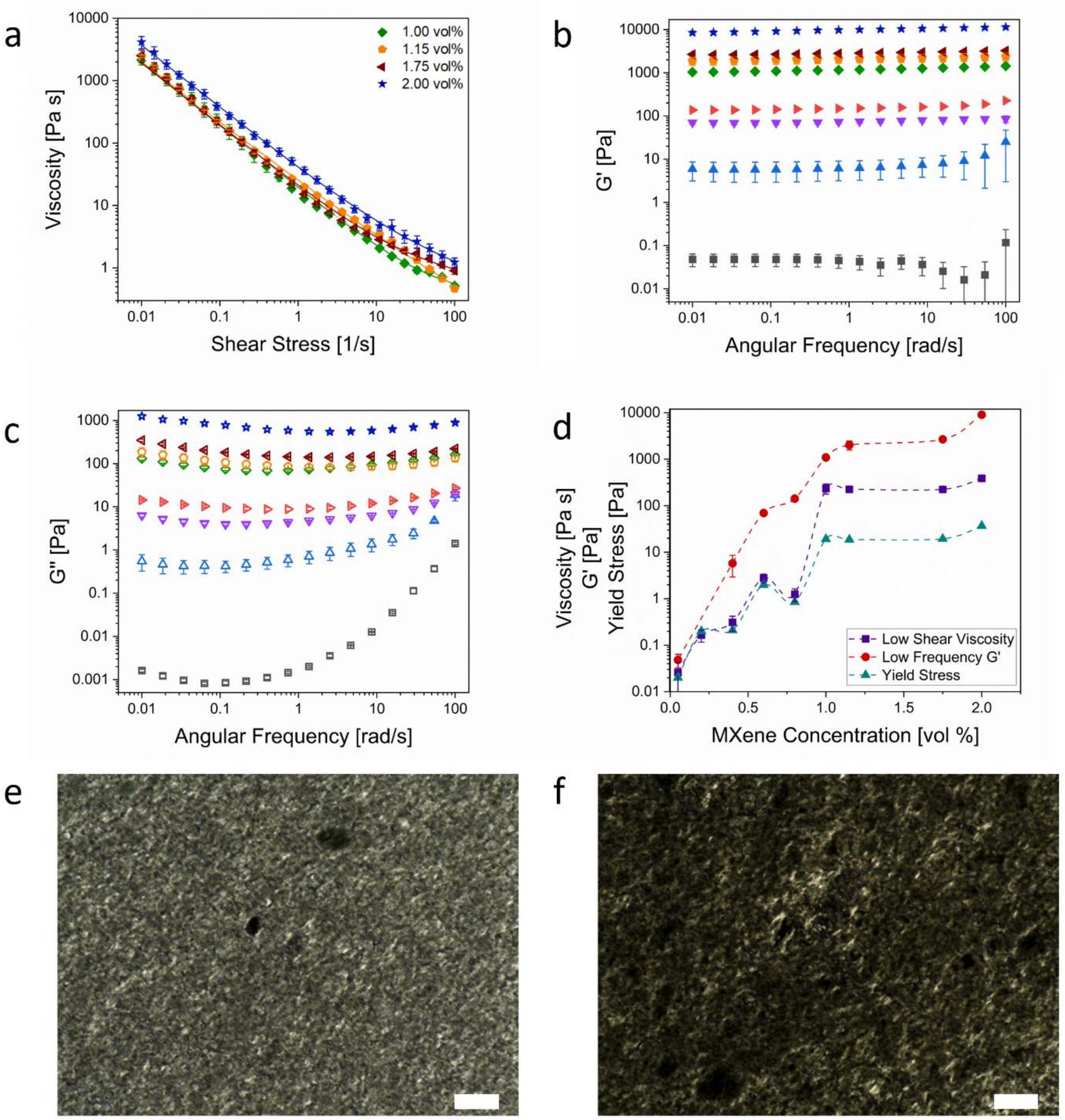

Figure 5.12. a) Flow curves of S-MXenes at 1.00 vol % (green diamonds), 1.15 vol % (orange pentagons), 1.75 vol % (maroon left triangles), and 2.00 vol % (dark blue stars). b) G' of S-MXenes at 0.05 vol % (black squares) 0.40 vol % (blue triangles), 0.60 vol % (purple upside-down triangles), 0.80 vol % (red right triangles), 1.00 vol % (green diamonds), 1.15 vol % (orange pentagons), 1.75 vol % (maroon left triangles), and 2.00 vol % (dark blue stars). c) G'' of S-MXenes, with legend following that of G'. d) Low shear viscosity, low frequency G', and yield stress of S-MXenes as a function of concentration. Error bars represent standard error of three to four runs. e) Cross-polarized microscopy of 1.00 vol % and f) 1.75 vol % S-MXenes. Scale bars represent 10 μm.

5.2.4 Bimodal MXenes

In the last ten years, a growing number of nanomaterial researchers have begun to view size polydispersity as a tool to tune dispersion phase behavior and the properties of solid nanomaterial assemblies.[44] For example, Kayali et al. showed that mixing large and small MXene sheets enabled the fabrication of electrodes with both high electronic and ionic conductivities.[145] However, they did not study the effects of polydispersity on dispersion phase behavior. Jalili et al.'s studied the effects of mixing graphene oxide (GO) size distribution on the phase behavior, rheological properties, and spinnability of aqueous GO dispersions.[14] They found that small GO sheets (L ~ 0.2 μm) did not undergo liquid crystal phase formation due to their low excluded volume. However, the addition of amount of ultra-large GO sheets (L ~ 37 μm) reduced the excluded volume available to the small sheets and induced nematic liquid crystal phase formation. Interestingly, they found that liquid crystalline phase formation occurred even upon mixing fully isotropic dispersions of ultra-large and small GO sheets. It should be noted that while polydispersity is generally viewed as widening the biphasic region, predicting the effects of polydispersity on the rheology and phase behavior of charged two dimensional mesogens is an ongoing theoretical challenge due to the combined effects of fractionation of larger aspect ratio mesogens to the liquid crystalline phase, the potential for isotropic-nematic-columnar phase coexistence, complex electrostatic interactions, and sedimentation of mesogens denser than the solvent.[44, 146, 147] Inspired by these previous works, it is hypothesized that a bimodal mixture (by volume) of small and large MXene sheets (B-MXenes) would reduce the tendency of the large MXenes to form dense flocs and enable alignment of the small sheets via the same excluded volume mechanism described by Jalili et al.[14]

The B-MXene dispersion steady shear data was divided into three distinct groups (**Figure 5.13**). The bottom grouping displayed low shear viscosities near 0.5-1.0 Pa s and high shear viscosities approaching that of the solvent. This was followed by a second grouping of data within an order of magnitude of each other, all showing slight viscosity hesitations indicating potential liquid crystalline phase behavior. The third group included the highest concentrations of B-MXene dispersions studied, with steady shear viscosities that nearly overlapped. These distinct groups suggested clear phase transition boundaries; this is further supported by POM and oscillatory rheology measurements.

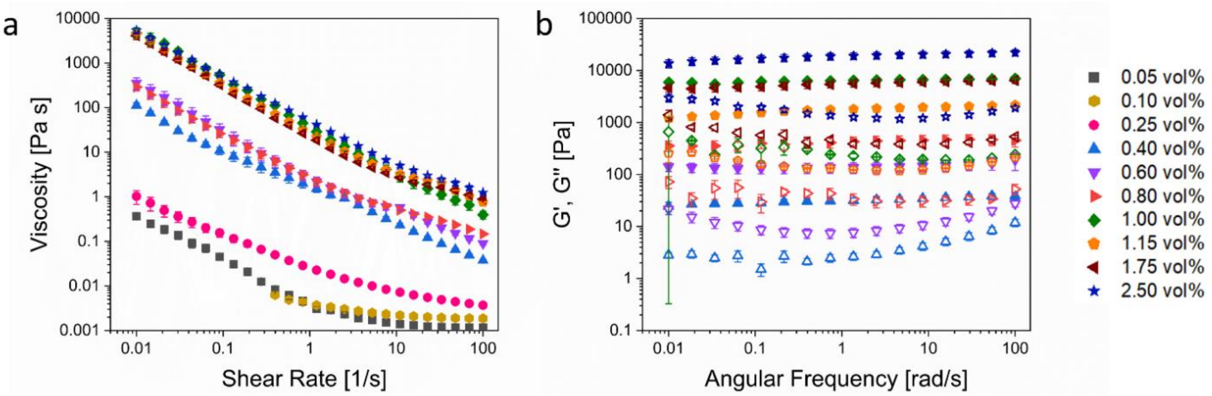

Figure 5.13. a) Steady shear and b) oscillatory rheology of all B-MXene dispersions studied in this work. Filled symbols in b) represent G' and hollow symbols represent G". Error bars represent standard error of three to four runs.

The lowest concentration of B-MXene dispersions investigated was 0.01 vol %, though torque limitations on the rheometer prevented any reliable measurements of this dispersion. Cross-polarized microscopy of the dispersion showed small birefringent domains with some apparent long-range ordering, despite the low B-MXene content (**Figure 5.14a**). This observation indicated that bimodal MXenes readily formed aligned polydomains in an isotropic sea, and so were in the biphasic region. When the B-MXene concentration was increased to 0.05 vol %, rheological measurements could be taken. Compared to the previous two size fractions of MXenes studied at this concentration, the onset of the high shear viscosity plateau occurred at shear rates as low as 20 s^{-1} (fitted to the Herschel-Bulkley model in **Figure 5.14b**). Cross-polarized microscopy showed a microstructure similar to that of the 0.05 vol % L-MXenes with small domains. However, the 0.05 vol % B-MXenes exhibited a more aligned structure with brightly lit domains extending in one diagonal direction and darker domains extending in the opposing diagonal direction (**Figure 5.14c**). This increased alignment over the L-MXenes of the same concentration was likely due to the excluded volume effects caused by using both large and small MXene sheets. At 0.10 vol %, the aligned domains extended in length and began to resemble more a woven texture, similar to the observed texture in L-MXenes of the same concentration (**Figure 5.14d**). The transition to the woven structure of the slightly increased concentrations suggested a more extended alignment than that observed in 0.05 vol % B-MXenes.

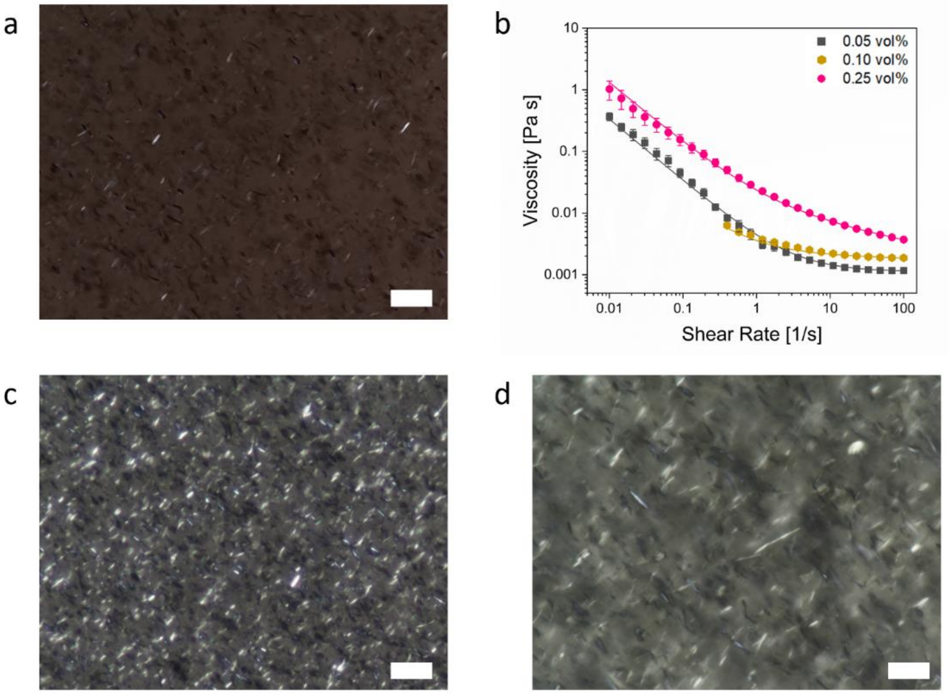

Figure 5.14. a) Cross-polarized microscopy of 0.01 vol % B-MXenes. b) Flow curves fitted to the Herschel-Bulkley model of B-MXenes at 0.05 vol % (black squares), 0.10 vol % (gold hexagons), and 0.25 vol % (pink circles). Error bars represent standard error of three to four runs. c) Cross-polarized microscopy of 0.05 vol % B-MXenes. d) Cross-polarized microscopy of 0.1 vol % B-MXenes. Scale bars are 10 μm.

Cross-polarized microscopy of 0.25 vol % B-MXenes (**Figure 5.15a**) revealed a similar microstructure to 0.10 vol %. The existence of non-birefringent isotropic regions in the background of the 0.25 vol % B-MXenes at 120x indicated that these dispersions remained in a mostly isotropic, though biphasic region. This was an unexpected observation, due to the nearly complete liquid crystalline phase that was observed in L-MXene dispersions of the same concentration. As previously stated, based on GO literature of similar bimodal dispersions,[14] it was hypothesized that liquid crystallinity would be observed in lower concentrations of B-MXenes as compared to L-MXene dispersions. However, 0.25 vol % B-MXenes remained in the biphasic region with distinction between isotropic and aligned phase visible even under non-cross polarized light (**Figure 5.15b**). This deviation from the theory of achieving liquid crystallinity at lower concentrations with a bimodal dispersion could have occurred due to the ratio of S-MXenes to L-MXenes used in this work.[53] Only a 1:1 volume ratio was investigated; further studies are required to determine how adjustment of this ratio could more easily induce the liquid crystalline phase. Steady shear rheology of this dispersion also indicated that progression into a nematic liquid crystalline phase had not been achieved. Though the high shear plateau of the lower concentrations had disappeared, the increase in value of the viscosity across all shear rates did not greatly increase (**Figure 5.14a**). For example, low shear viscosity only increased from ~0.4 to ~1.0 Pa s at concentrations of 0.05 vol % and 0.25 vol%, respectively. When fitted to the Herschel-Bulkley model, the yield stress did not increase to a significant value (**Table 5.3**).

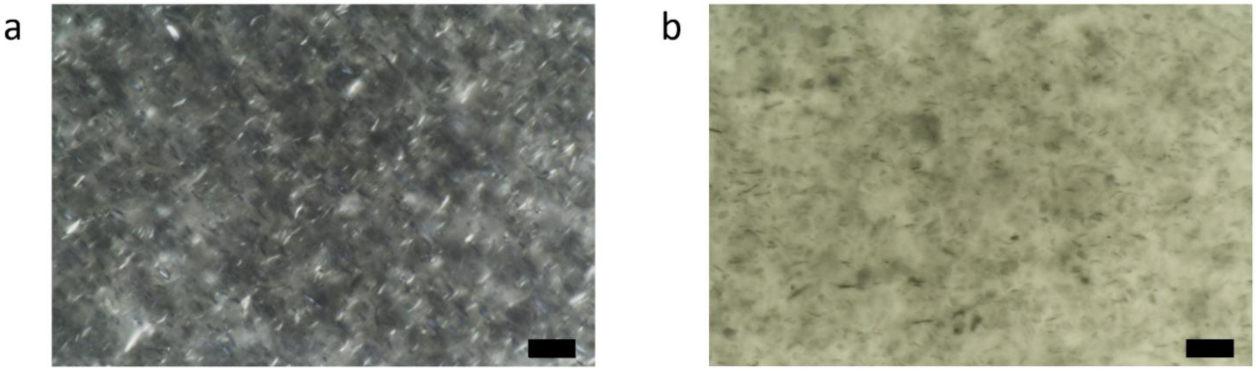

Figure 5.15. a) Cross-polarized and b) non-cross polarized microscopy 0.25 vol % B-MXenes. Scale bars represent 10 μm.

	Region 1			Region 3		
B-MXene vol %	Yield Stress (Pa)	K (Pa s^n)	n	Yield Stress (Pa)	K (Pa s^n)	n
0.05	0.003	0.001	1.00	-	-	-
0.10	0.001	0.002	0.96	-	-	-
0.25	0.01	0.01	0.76	-	-	-
0.40	0.65	1.03	0.33	2.19	0.06	0.69
0.60	2.91	0.16	1.00	5.77	0.003	1.00
0.80	2.49	0.25	1.00	0	2.04	0.43
1.00	41.18	0.01	0.00	-	-	-
1.15	31.23	1.28	0.81	-	-	-
1.75	27.50	0.67	1.00	-	-	-
2.50	49.45	0.98	0.96	-	-	-

Table 5.3. Herschel-Bulkley parameters of all B-MXene dispersions investigated through rheology. It is noted that 0.01 vol % B-MXenes did not meet torque requirements for rheology.

Within the middle grouping of B-MXene concentrations in **Figure 5.13** (0.40 vol % - 0.80 vol %), behavior similar to that of three region viscosity behavior was observed. Region II again appeared as hesitations in the dispersion viscosity at intermediate shear rates rather than extended viscosity plateaus. Each of the dispersions in this middle grouping were fitted to the Herschel-Bulkley model in two sections, with resulting fits in **Figure 5.16a**. Though three region behavior was seen in L-MXene dispersions as low as 0.25 vol %, it was at slightly higher concentrations of 0.40 vol %, 0.60 vol %, and 0.80 vol % that B-MXenes exhibited this behavior. This follows with the lack of liquid crystalline signature textures in B-MXenes at 0.25 vol %. It is noted that in the 0.80 vol % B-MXene dispersion, the Herschel-Bulkley parameters produced a yield stress of 0 in Region 3. This follows expected behavior of a nearly complete liquid crystal, in which the high shear region consists of domains aligned with the pre-established flow.[64, 148] Oscillatory rheology of this middle group of B-MXene dispersions exhibited G' nearly independent of frequency, indicating the presence of a percolated network (**Figure 5.16b**). This along with the increase of G'' at high frequencies for these dispersions further indicated a nearly complete liquid crystalline phase.

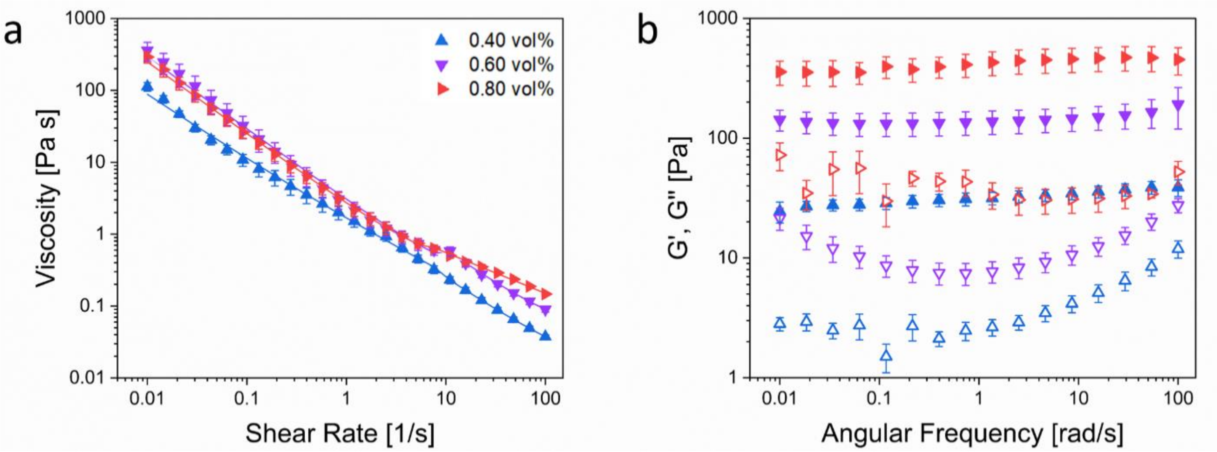

Figure 5.16. a) Flow curves and b) oscillatory rheology of B-MXenes at 0.40 vol % (blue triangles), 0.60 vol % (purple upside-down triangles), and 0.80 vol % (red right triangles). Filled symbols in b) represent G' and hollow symbols represent G''. Scale bars represent standard error of three to four runs.

Partially cross-polarized microscopy of this middle grouping of B-MXene dispersions showed that they exhibited brush-like Schlieren textures and birefringence. **Figure 5.17** depicts the birefringence observed in 0.40 vol % and 0.60 vol% B-MXenes where the sample underwent a complete change of appearance as the sample was rotated under partially cross-polarized light. However, small regions of isotropic phase remained, indicating that only a mostly liquid crystalline phase had been formed. Higher MXene concentration increased the opacity of the dispersions, making it more difficult to observe birefringence than at lower concentrations. The extended aligned structures observed in these dispersions supported the transition in rheological properties to those similar of liquid crystalline signatures as described in **Figure 5.17**.

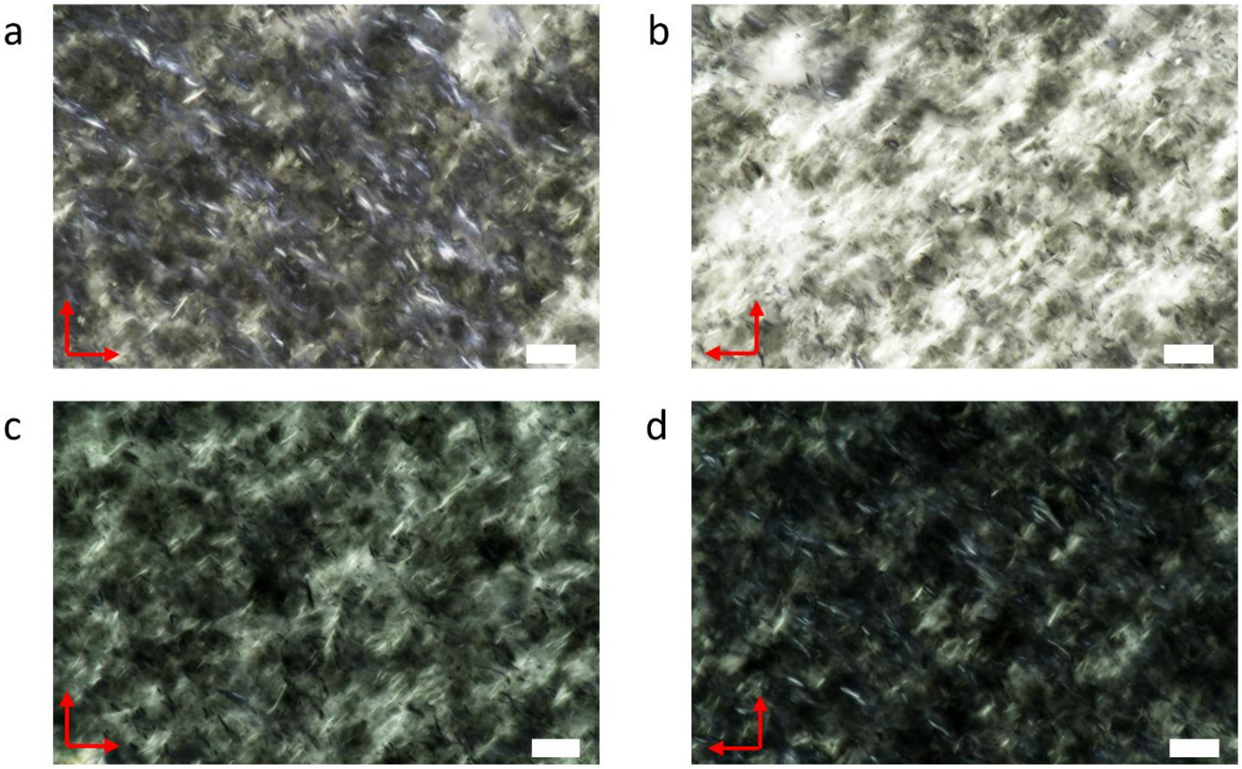

Figure 5.17. Cross-polarized microscopy of a) 0.40 vol % B-MXenes at 0° stage rotation and b) 90° stage rotation, and c) 0.60 vol % B-MXenes at 0° stage rotation and d) 90° stage rotation. Scale bars represent 10 μm.

Within the top data grouping in Figure 4.13a, B-MXene dispersions began to exhibit the rheological signatures of a gel. Flow curves exhibited more consistent shear-thinning behavior and increases in viscosity (**Figure 5.18a**). Low shear viscosity jumped from ~300 to ~5500 Pa s in

0.80 vol % and 1.00 vol % B-MXene dispersions, respectively. The storage modulus of the B-MXenes exhibited a large increase at 1.00 vol % (**Figure 5.18b**). The low shear viscosity and yield stress also plateaued at this concentration (**Figure 5.18c**). The partially cross-polarized microscopy of the 1.00 vol % B-MXene dispersion depicted a noticeable change in microstructure from the fully liquid crystalline dispersions at lower concentrations (**Figure 5.18d**). Birefringence was still observed in domains similar in structure to those observed in the aggregated nematic gel L-MXenes. Some dense flocs or aggregates were observed in the 1.00 vol % B-MXenes (**Figure 5.18e**), though they were noted to be smaller than those in the 0.60 vol % L-MXenes. This was likely due to the inclusion of S-MXenes within the dispersion. The smaller surfaces and excluded volume of the S-MXenes enabled a more stable dispersion at higher concentrations. 1.15 vol % B-MXenes exhibited similar microstructures to 1.00 vol % (**Figure 5.18f**); however, above this concentration, the samples became too opaque and could not be observed through microscopy. Due to similarity in rheological properties, it is likely that B-MXenes remained in a nematic gel phase through the highest concentration investigated of 2.50 vol %.

With the combined use of rheology and polarized optical microscopy, it was determined that the three groupings of steady shear data in **Figure 5.13a** coincided with three distinct phases: a mostly isotropic phase, a mostly liquid crystalline phase, and a nematic gel phase. The separation of phases with supporting rheological properties and microstructural changes promotes the tunability of bimodal MXene dispersions for a variety of fluid-phase processing. Due to this, B-MXene dispersions were chosen as the primary candidate for further study in dispersion-printing trials. The goal for these trials is to round out the structure-property-processing relationships of aqueous MXene dispersions. Further discussion of this future work can be found in Chapter 7.

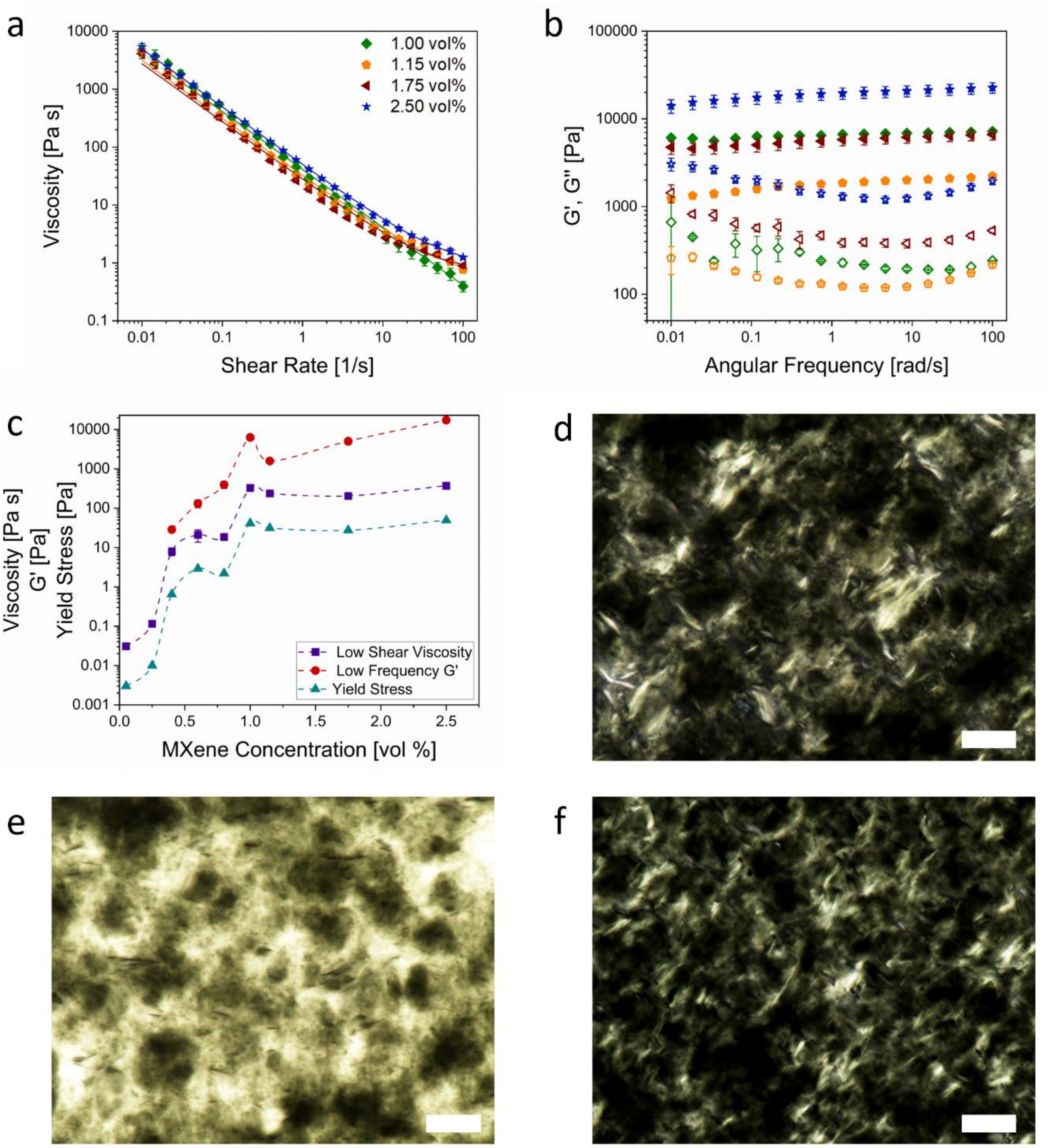

Figure 5.18. a) Flow curves of B-MXenes at 1.00 vol % (green diamonds), 1.15 vol % (orange pentagons), 1.75 vol % (maroon left triangles), and 2.50 vol % (dark blue stars). b) Oscillatory rheology of B-MXenes, with legend following that in a). Filled symbols represent G' and hollow symbols represent G''. c) Low shear viscosity, low frequency G' and yield stress of B-MXenes as a function of MXene concentration. Error bars represent standard error of three to four runs. d) Cross-polarized microscopy and e) non-cross polarized microscopy of 1.00 vol % B-MXenes. f) Cross-polarized microscopy of 1.15 vol % B-MXenes. Scale bars represent 10 µm.

Comparing the low shear viscosities and storage moduli of the small, large, and bimodal dispersions (**Figure 5.19**) highlights the complex interrelationships between sheet-size, rheological properties, and phase behavior. For isotropic dispersions, viscosity typically increases with concentration. However, for uncharged rod-like lyotropic mesogens, both viscosity and storage modulus initially increase with concentration but reach a maximum once the system becomes predominantly liquid crystalline. Increasing the concentration results in an increase in the fraction of the dispersion that is aligned resulting in a decrease in viscosity and storage modulus until a local minima is reached at Φ_{LC}. Increasing the concentration above Φ_{LC} results in a jammed structure and a sudden increase in both viscosity and storage modulus.[149] However, for charged 1D systems such as cellulose nanocrystals, halloysite, and chitin, this non-monotonic behavior becomes muted by electroviscous effects;[150] it is noted that the rheology of charged 2D mesogens has not been studied as thoroughly as that of 1D mesogens. In this work, all three dispersions showed a slight decrease in viscosity between 0.60 vol% and 0.80 vol% where the dispersions were predominantly liquid crystalline but still possessed isotropic regions. Above this concentration, the viscosities of the S-MXenes and B-MXenes initially increased and then plateaued in the gel region. The viscosity of the L-MXenes continued to increase but not as sharply as they did initially; the different behavior of the L-MXenes may be the result of large floc formation. In terms of storage modulus, the values of G' for the S-MXene and B-MXenes increased sharply until 1.00 vol% and then appeared to plateau as the dispersions formed kinetically arrested gels. Interestingly, the value of G' for the B-MXenes was only slightly higher than for the S-MXenes for all concentrations except for 1.00 vol% where it was nearly an order of magnitude greater and then decreased at higher concentrations. The L-MXenes reached a similarly high value of G', but at the lower concentration of 0.60 vol%. Above 0.60 vol%, the storage modulus of the

L-MXene dispersions decreased and then slowly increased again. The mechanism behind these variations is unclear, however POM images suggest it may be related to the floc formation exhibited by the B-MXene and L-MXene dispersions.

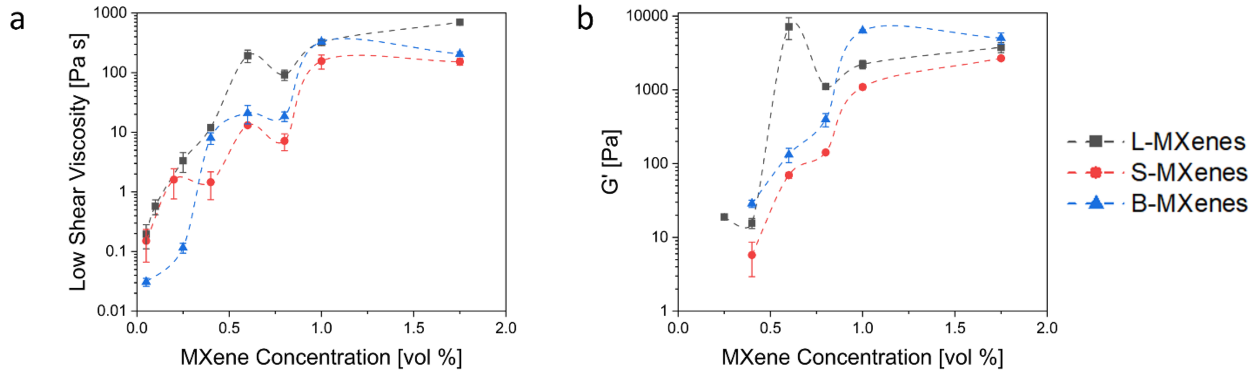

Figure 5.19. a) Low shear viscosity (at 0.1 1/s) and b) low frequency storage modulus (at 0.1 rad/s) of size fractionated MXenes as a function of MXene concentration.

5.3 Conclusions

This research highlights that, similar to other charged 2D nanomaterials, such as nanoclays and GO, aqueous dispersions of MXene sheets exhibit complex rheology and phase behavior. The following lyotropic phase diagram summarizes the results of this work based on the critical transitions determined for three MXene size fractions through the combined use of rheology and polarized optical microscopy (**Figure 5.20**). This is the first phase diagram developed for size fractionated aqueous MXene dispersions. The size of the sheets influenced the concentration at which aligned domains were formed as well as the microstructures. Nearly complete liquid crystallinity with regions of extended alignment was achieved for the large and bimodal MXenes. Short range, liquid crystal-like ordering was achieved in the small MXenes. Results from this work suggest that the drastic difference in microstructure for the small MXenes and their inability to develop an extended structure are likely attributed to the more compact arrangement of the smaller sized sheets. Based on previous 2D colloidal studies, this finer morphology of the S-MXenes may result in low levels of processability. At sufficiently high concentrations, all the MXene dispersions displayed gel-like phase behavior. Through microscopy, these gel phases were observed to be nematic, though the L-MXenes displayed a two-phase system containing significant large flocs or aggregates. The B-MXenes also exhibited signs of flocculation or aggregation in the gel phase, though to a much lesser degree than the L-MXenes. Using a bimodal mixture of large and small MXenes provided insight into how controlling the polydispersity of MXenes could enable more precise tunability and increased stability for various fluid-phase processing methods. The ability of B-MXenes to reach the biphasic and near liquid crystalline regions at low concentrations while simultaneously preventing severe aggregation shows excellent potential for methods such as direct-ink-writing and fiber spinning.

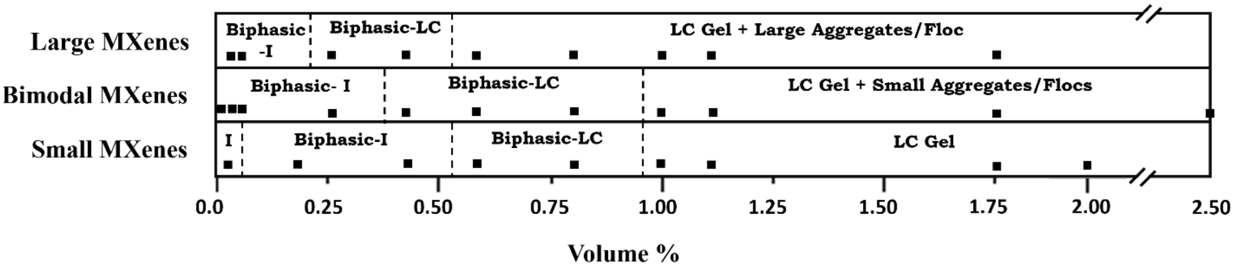

Figure 5.20. Aqueous phase behavior of each of the three size fractions of MXene studied, where I indicates a fully isotropic phase, Biphasic-I indicates the biphasic, mostly isotropic phase, Biphasic-LC indicates a mostly liquid crystal phase, and LC Gel indicates the nematic gel phase. Squares represent data discussed in this investigation.

The results of these studies highlight that using mixtures of MXene size fractions to tune dispersion rheology and morphology. Exploration of additional ratios of large and small sheets are needed to understand the effects of sheet size these dispersion properties as well as the performance of assembled MXene materials and devices. In addition, neutron scattering and x-ray scattering studies would facilitate gaining more insights into the arrangement of, and spacing between, dispersed sheets. The combined use of rheology with neutron or x-ray scattering is particularly promising for understanding the effects of shear on microstructure. The phase diagram and rheology results from this research also provide a foundation for exploring the dispersion behavior of other MXene chemistries and 2D nanomaterial systems.

Chapter 6 – Effects of Salt Addition on the Phase Behavior and Rheological Properties of Bimodal MXenes

6.1 Motivation

Changes in phase behavior of MXene dispersions due to salt addition are expected due to the structural similarity of MXenes to various nanoclays. The surfaces of MXene particles are negatively charged while the edges are positively charged providing face and edge interactions that can result in network formation similar to the mechanisms for nanoclays.[30] The classical DLVO theory describes the interactions between charged surfaces in a liquid medium by a combination of the attractive van der Waals and repulsive electrostatic forces.[32] Particles in dispersions can associate due to their thermal motion and charge distribution to form various structure types, such as dispersed, aggregated, flocculated but dispersed, and flocculated and aggregated structures.[88, 151] Flocs are large clusters of particles that are loosely bound and can be broken up more readily than aggregates. Aggregates are multiple layers of particles that are attached in a dispersion, typically through face-to-face interactions.[88] In terms of the classic DLVO total interaction energy profile, flocs reside in the shallow secondary minimum whereas aggregates reside in the deep primary minimum. This indicates that aggregates have a substantially greater interparticle adhesion strength than flocs. Tuning the dispersion by changes in pH or addition of a salt or polymer can induce flocculation. Low volume fraction dispersions can form a gel if flocs or aggregates of sufficient strength associate to form space filling networks through interparticle bonds.[152, 153]

The focus for this study is to extend the results of Chapter 5 with providing insights into the effects of salt addition on MXene dispersion phase behavior and rheological properties. In this chapter, the bimodal system of selectively polydisperse large and small sheets denoted as B-MXenes are investigated in more detail. This work highlights the impact of salt concentration on lyotropic phase transitions, microstructural alignment and aggregation, and rheological properties of aqueous B-MXene dispersions. The efforts from this research will contribute to enhanced MXene processability, performance of MXene-based devices, and overall fundamental understanding of 2D colloid science.

6.2 Results

6.2.1 Bimodal MXene Characterization

AFM was used to measure the size fractionated large and small MXene sheets before selectively combining them in a 1:1 by volume ratio to prepare the B-MXene dispersions. The size and thickness of 50 large MXene sheets measured with AFM resulted in $\langle L \rangle$ = 2.47 ± 0.99 μm and thickness $\langle D \rangle$ = 2.09 ± 0.39 nm. AFM measurements of 50 small MXene sheets resulted in an average lateral dimension of $\langle L \rangle$ = 0.32 ± 0.16 μm. Representative AFM images of large and small sheets and the size distribution of each are in **Figure 6.1**. It is noted that the total sheet size distribution of the synthesized MXene batches used in this section of work was similar to the sheet size distribution of the batches used in the previous section on MXene size effects. This ensures that the dimensions of the MXenes used throughout this research remained relatively consistent and limited concerns of batch-to-batch variation.

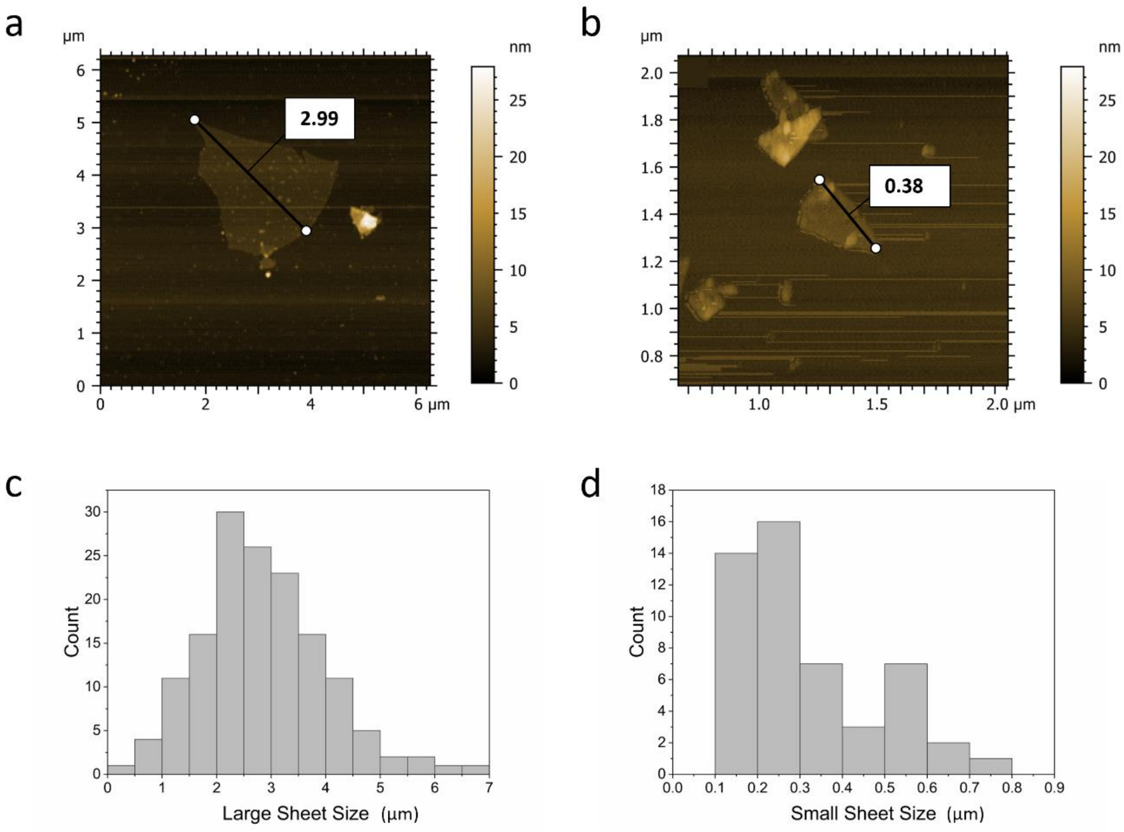

Figure 6.1. Atomic force microscopy (AFM) images of (a) large MXenes and (b) small MXenes, and size distribution of (c) large MXene sheets and (d) small MXene sheets used in this section of the research.

6.2.2 Bimodal MXenes with NaCl

In Chapter 5, bimodal dispersions of large and small MXene sheets in a 1:1 volume ratio exhibited similar microstructure and rheological properties to the dispersions containing large MXene sheets only; however, the bimodal MXenes displayed an increased resistance toward aggregation leading to a more stable and processable dispersion. To further study B-MXenes, a series of bimodal dispersions with total sheet concentrations in the range of 0.10 – 1.0 vol % (5.2 to 48 mg/mL) MXene and 0 – 0.5 M NaCl were prepared and investigated with similar optical microscopy and rheology protocols as utilized in Chapter 4.

At 0.10 vol %/0 M, the B-MXene dispersions exhibited aligned thread-like domains under partially cross-polarized light as shown in **Figure 6.2a**, where the left column is partially cross polarized images and the right column images are without cross polarization. As stated in Chapter 5, the observable aligned microstructure of this dispersion with competing isotropic regions throughout indicates the biphasic region. At salt concentrations of 0.01 – 0.1 M NaCl, the 0.10 vol % bimodal dispersions maintained a biphasic microstructure with these aligned domains arranged diagonally across the sample (**Figure 6.2b-d**). However, at 0.05 M and 0.1 M, the isotropic regions increased in size. This increase in isotropic regions likely occurred due to the compression of the electric double layer (EDL) surrounding the charged MXene sheets. According to the fundamental theories of charged particles, the compressed EDL surrounding the charged sheets would allow them to approach one another at closer distances.[118] This could lead to separation of the microstructure as the MXenes formed more closely packing structures, leaving isotropic regions throughout due to the low MXene concentration. A more significant change in microstructure occurred at the salt concentration of 0.5 M, where large flocs caused complete breakage of the structure (**Figure 6.2e**). The high NaCl concentration of the dispersion induced the flocculation due to dominating attractive van der Waals forces.[129] All optical microscopy images in the right column of **Figure 6.2** show the dispersion without cross polarization. These images accentuate the progression of microstructural separation as a result of increased NaCl concentration.

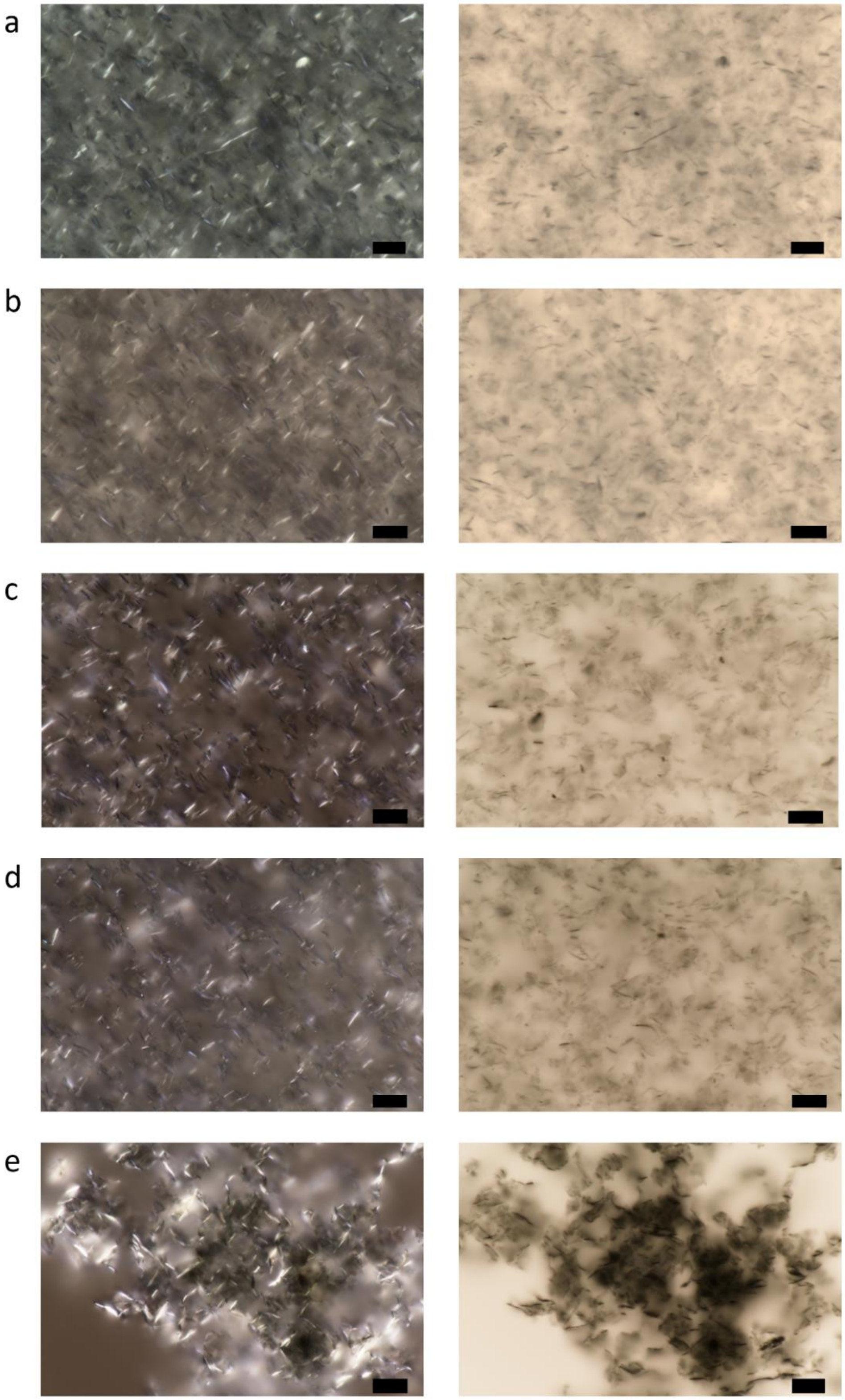

Figure 6.2. Optical microscopy images of 0.10 vol % B-MXenes at a) 0 M, b) 0.01 M, c) 0.05 M, d) 0.1 M, and e) 0.5 M. Left column images are under partially cross polarization and right column images are without cross polarization. Scale bars represent 10 μm.

Steady shear rheology of the 0.10 vol % bimodal dispersions showed small changes in viscosity as the salt concentration increases from 0 M – 0.1 M (**Figure 6.3a**). Only data within the torque limitations of the rheometer are shown. When fitted to the Herschel-Bulkley model, these dispersions had near-zero yield stresses ranging from 0.001-0.02 Pa s and *K* values of 0.002-0.005 Pa s^n, suggesting behavior more similar to a power law fluid (**Table 6.1**). However, when the data was fitted to the power law model, there were severe discrepancies between the data and the model fitting (**Figure 6.3b**). The poor fits indicated that the 0.10 vol % B-MXene dispersions could not accurately be described as power law fluids. At a salt concentration of 0.5 M NaCl, the yield stress increased to 1.20 Pa, as well as a nearly two order of magnitude increase in viscosity from ~2 Pa s to 150 Pa s. This change in rheological properties occurred alongside the formation of large flocs, reaffirming the importance of utilizing both microscopy and rheology. Similar rheological behavior as a result of aggregation in biphasic dispersions has previously been reported in which decreased repulsive forces from increased salt concentration caused dispersion instability.[154]

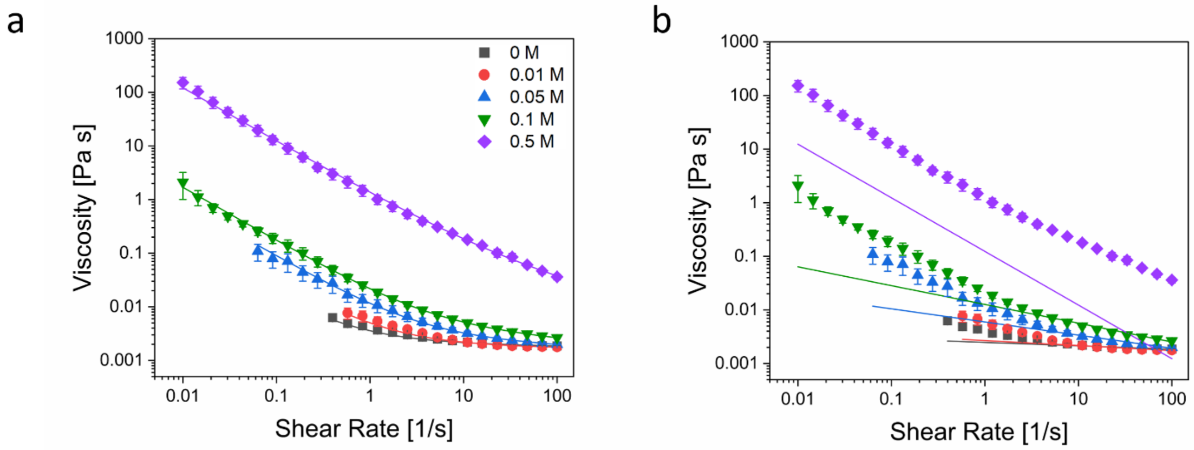

Figure 6.3. Steady shear rheology of 0.10 vol % B-MXenes at 0 M (black squares), 0.01 M (red circles), 0.05 M (blue triangles), 0.1 M (green upside-down triangles), and 0.5 M (purple diamonds) fitted to the a) Herschel-Bulkley model and b) power law model. Error bars represent standard error of three to four runs.

	Herschel-Bulkley Model			Power Law Model	
Salt Concentration (M)	Yield Stress (Pa)	K (Pa s^n)	n	K (Pa s^n)	n
0	0.001	0.002	0.96	0.002	0.94
0.01	0.003	0.002	0.96	0.003	0.90
0.05	0.01	0.003	0.90	0.006	0.75
0.1	0.02	0.005	0.85	0.01	0.65
0.5	1.20	0.17	0.59	0.12	0

Table 6.1. Model fits for steady shear behavior of 0.10 vol % B-MXenes.

In dispersions of 0.25 vol % B-MXenes, similar microstructural changes to those in 0.10 vol % dispersions were observed. As shown in the left column, at 0 M and 0.01 M, weaving domains extended across the sample and appeared birefringent when the microscope stage was rotated (**Figure 6.4a,b**). As the salt concentration was increased to 0.05 M and 0.1 M, the isotropic regions expanded and disrupted the continuous microstructure due to the compressed EDL of the MXene sheets (**Figure 6.4c,d**). The beginnings of a flocculated structure appeared at a NaCl concentration of 0.1 M, though a continuous microstructure was maintained. When the salt concentration was increased to 0.5 M NaCl, the formation of large, dense flocs resulted in complete structural breakage and a fully flocculated system (**Figure 6.4e**). The right column of **Figure 6.4** shows optical microscopy images without cross polarization to clearly depict the changing microstructure as a result of NaCl addition.

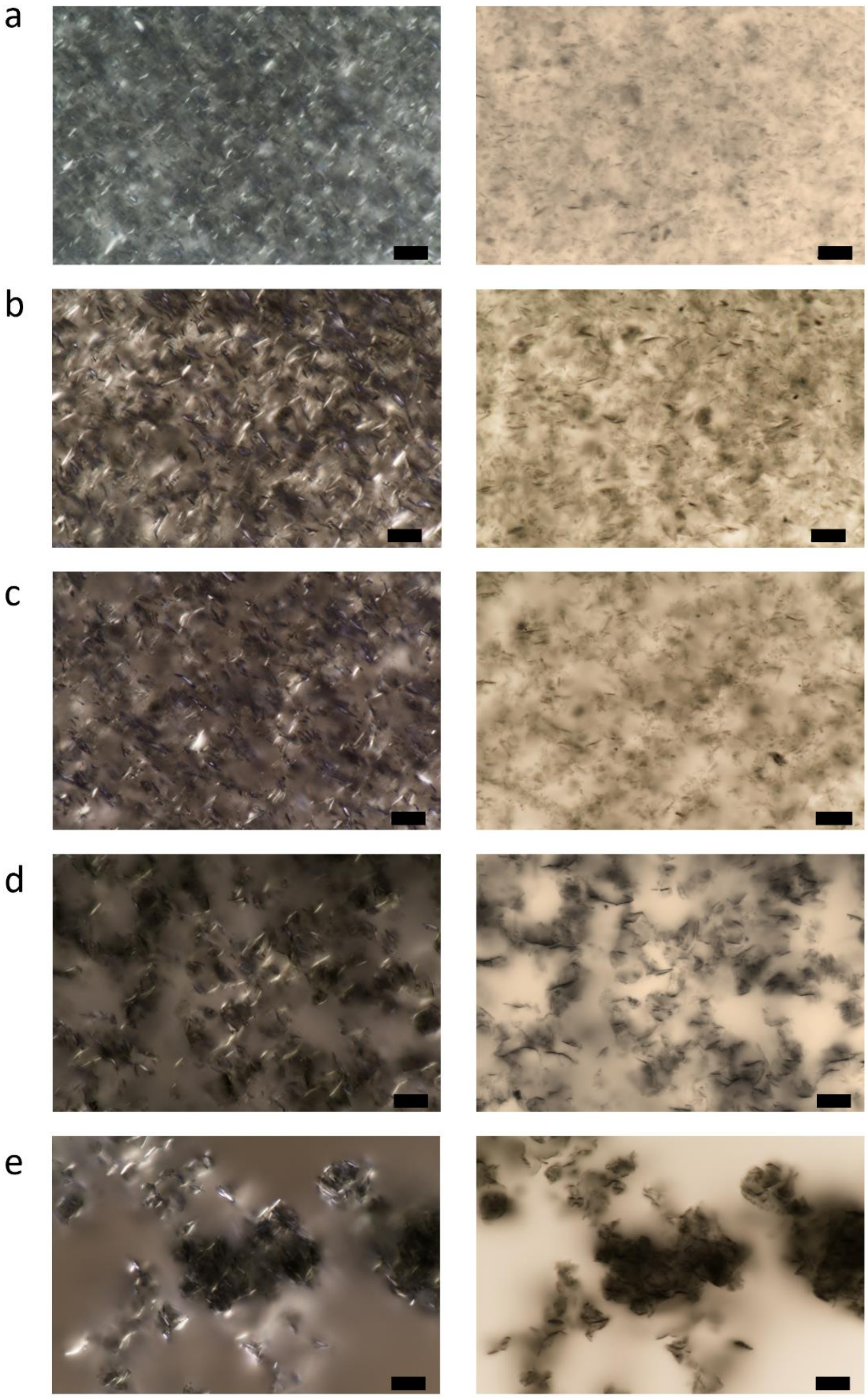

Figure 6.4. Optical microscopy images of 0.25 vol % B-MXenes at a) 0 M, b) 0.01 M, c) 0.05 M, d) 0.1 M, and e) 0.5 M. Left column images are under partially cross polarization and right column images are without cross polarization. Scale bars represent 10 μm.

The steady shear data for the 0.25 vol % B-MXene dispersions depicted a large increase in viscosity at 0.05 M (**Figure 6.5a**), and though torque requirements limited oscillatory data, a similar increase in storage modulus was observed at 0.05 M at high frequencies (**Figure 6.5b**). The 0.25 vol %/0.05 M and 0.25 vol %/0.1 M dispersions showed more consistent shear-thinning behavior with a development of a notable yield stress as compared to the 0.25 vol % dispersions with 0-0.01 M NaCl (**Figure 6.5c, Table 6.2**). This change in rheological properties at slightly increased salt concentrations exhibits the potential of NaCl as a rheological modifier. These results show that by adjusting the concentration of NaCl, the properties can be tuned to more desirable ranges for processing while maintaining the concentration of B-MXenes.

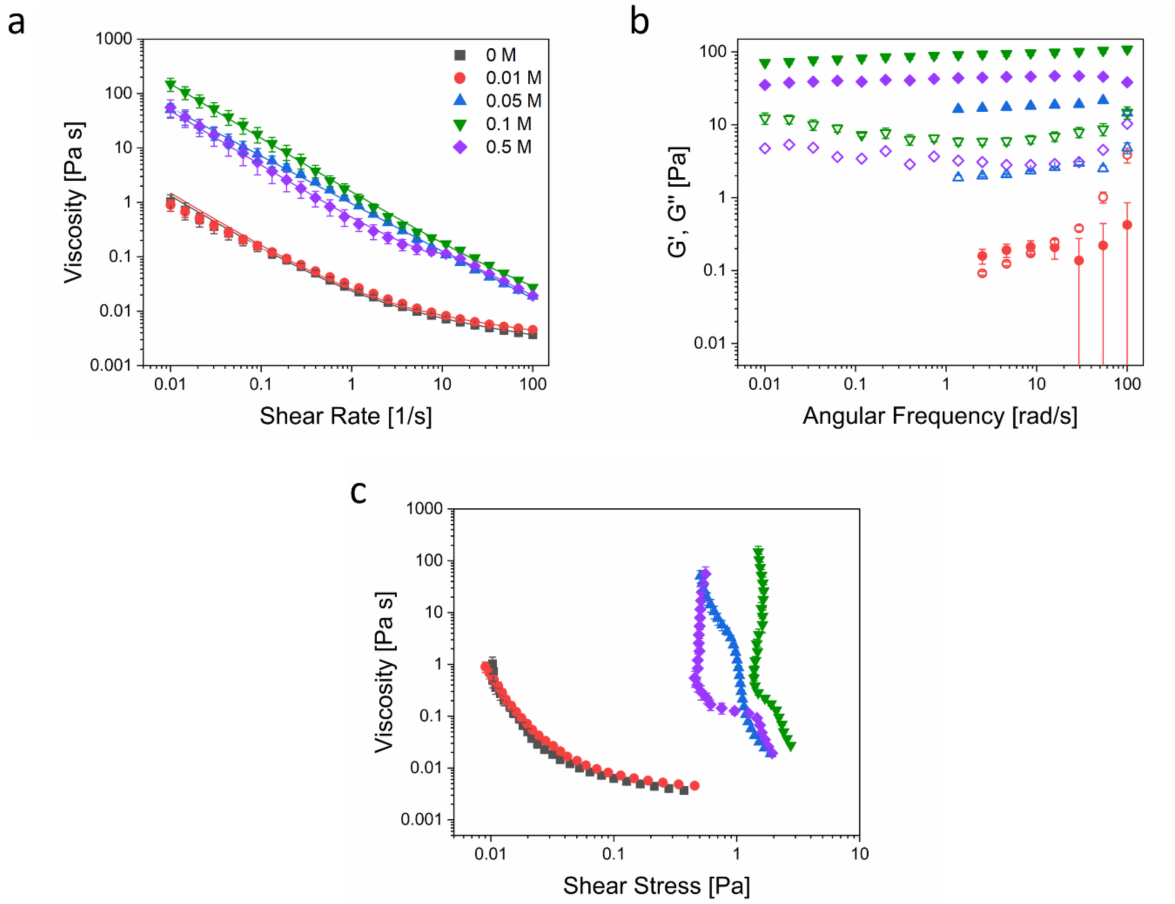

Figure 6.5. a) Steady shear rheology, b) oscillatory rheology (filled symbols represent G' and hollow symbols represent G''), and c) yield stresses of 0.25 vol % B-MXenes at 0 M (black squares), 0.01 M (red circles), 0.05 M (blue triangles), 0.1 M (green upside-down triangles), and 0.5 M (purple diamonds). Error bars represent standard error of three to four runs.

	Region 1			Region 3		
Salt Concentration (M)	Yield Stress (Pa)	K (Pa s^n)	n	Yield Stress (Pa)	K (Pa s^n)	n
0	0.01	0.01	0.76	-	-	-
0.01	0.01	0.01	0.80	-	-	-
0.05	0.10	0.85	0.14	-	-	-
0.1	1.50	0.07	0.66	-	-	-
0.5	0.48	0.05	1.00	0.001	0.87	0.17

Table 6.2. Herschel-Bulkley model fits for steady shear behavior of 0.25 vol % B-MXenes.

At 0.5 M NaCl, all rheological properties decreased. This behavior resembled that of salt-infused nanoclay dispersions in which high salt content caused network breakdown from an increase in face-face association of the 2D particles and compression of the EDL.[151] The change in dispersion microstructure from a loosely connected network of flocs to a disjointed system of dense flocs floating in an isotropic sea (**Figure 6.4e**) aligned with this description. A hesitation in the viscosity of the 0.25 vol %/0.5 M dispersion was observed at ~10 s^{-1}. In NaCl-free dispersions investigated in Chapter 5, this behavior was reminiscent of the three region behavior of liquid crystals. Though the steady shear data for 0.25 vol %/0.5 M B-MXenes was fitted according to this behavior, it should be noted that flocculated systems such as what was observed through microscopy of this dispersion may exhibit discrepancies in expected rheological behavior. The results from the Herschel-Bulkley model fitting showed that in Region 1, $n = 1$, which suggested behavior more similar to a Bingham plastic fluid. This was followed by an extremely low yield stress of 0.001 Pa s in Region 3. Rather than indication of liquid crystallinity, this viscosity hesitation likely resulted from the change from yielding behavior of the dispersion to aligned flow of the disjointed flocs dispersed throughout the fluid at shear rates greater than 10 s^{-1}.

As previously discussed in Chapter 5, increasing the B-MXene concentration to 0.40 vol % resulted in a nearly complete liquid crystalline phase. With no salt added, the 0.40 vol % bimodal dispersion exhibited a continuous microstructure that was almost completely birefringent under partially cross-polarized light (**Figure 6.6a**). The addition of 0.01 M NaCl initiated flocculation with a few observable dense flocs, though aligned birefringent domains persisted (**Figure 6.6b**). At NaCl concentrations of 0.05 M and 0.1 M, flocculation increased with more dense flocs interspersed throughout the microstructure (**Figure 6.6c,d**). The more pronounced flocculation at lower amounts of NaCl as compared to the previous MXene concentrations is likely a result of the increased packing of MXene sheets. Due to the higher MXene concentration in these dispersions, the sheets are in closer alignment to each other. In the presence of no NaCl, this resulted in a nearly complete liquid crystal; however, with NaCl added and the stability of the repulsive forces reduced, flocculation more readily occurred. At high NaCl content of 0.5 M, complete structural breakage occurred with the dispersion consisting only of disjointed, dense flocs (**Figure 6.6e**).

Steady shear rheology of these dispersions showed that from 0 M – 0.05 M NaCl, virtually no change in viscosity behavior or magnitude occurred (**Figure 6.7a**). Slight viscosity hesitations were observed in the same region, leading to a sectioned Herschel-Bulkley fitting for these dispersions (**Table 6.3**). Oscillatory rheology performed on the 0.40 vol % 0 M-0.05 M dispersions showed similar overlapping behaviors in the viscoelastic moduli as was observed with the viscosity behavior of these dispersions (**Figure 6.7b**). Their nearly frequency-independent G’ values indicated that a percolated network was achieved. At the higher salt concentrations of 0.1 M and 0.5 M NaCl, the viscosity and the viscoelastic moduli all increased by around one order of magnitude each. Herschel-Bulkley model fitting also resulted in a similar increase in yield stresses at higher salt concentrations.

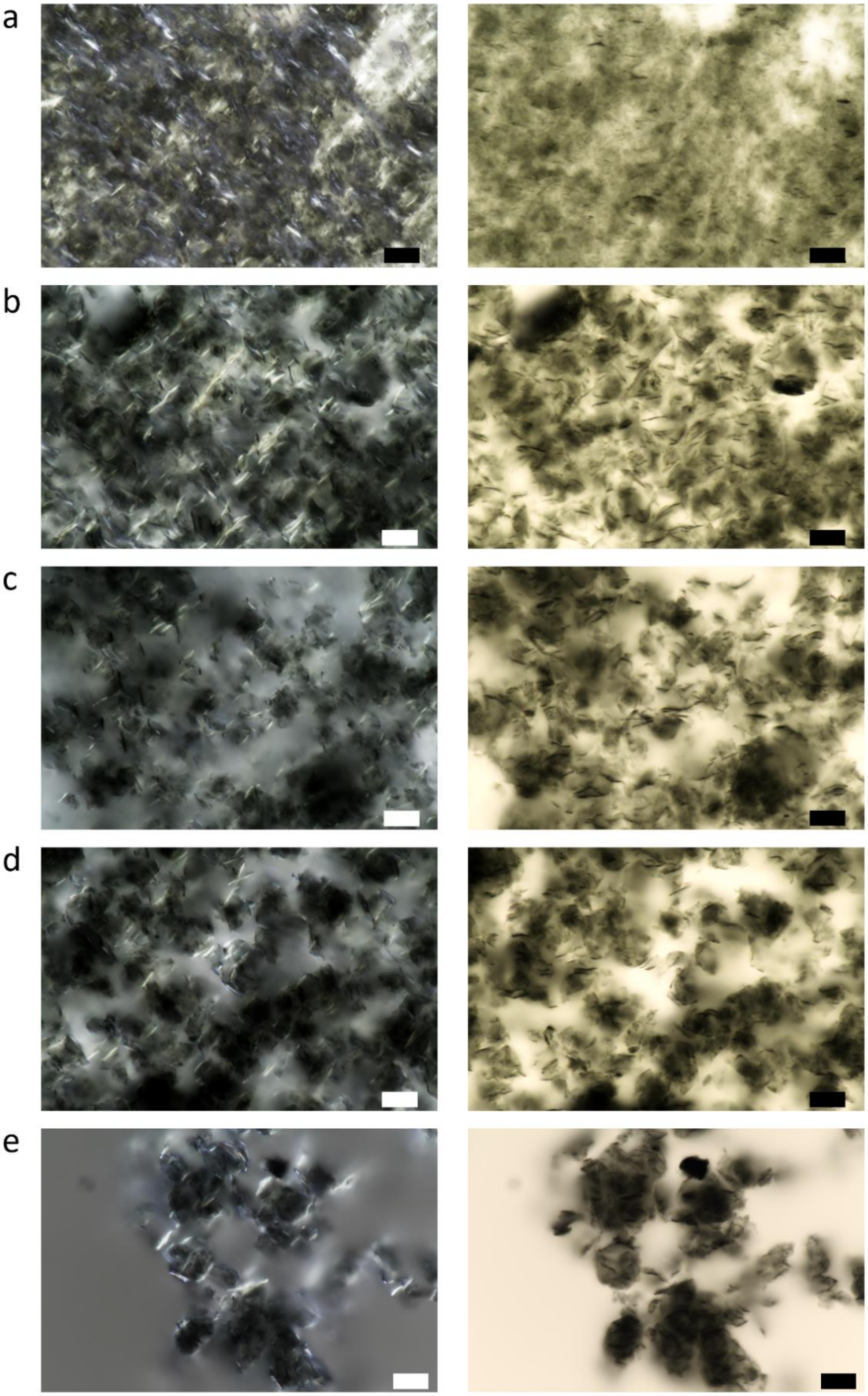

Figure 6.6. Optical microscopy images of 0.40 vol % B-MXenes at a) 0 M, b) 0.01 M, c) 0.05 M, d) 0.1 M, and e) 0.5 M. Left column images are under partially cross polarization and right column images are without cross polarization. Scale bars represent 10 μm.

At high frequencies, the G'' curve changed behavior for 0.40 vol %/0.1 M and 0.40 vol %/0.5 M. Rather than the increasing slope of G'' at high frequencies for the 0 – 0.05 M dispersions, the G" slope turned slightly negative, indicating the transition to a more gel-like behavior.[29] Based on this behavior and the increases in viscosity and viscoelastic moduli, a transition into a flocculated nematic gel phase likely occurred at 0.40 vol % /0.1 M. This again shows the potential for NaCl as a rheological modifier for MXene dispersions, though the increased flocculation observed in optical microscopy should also be considered.

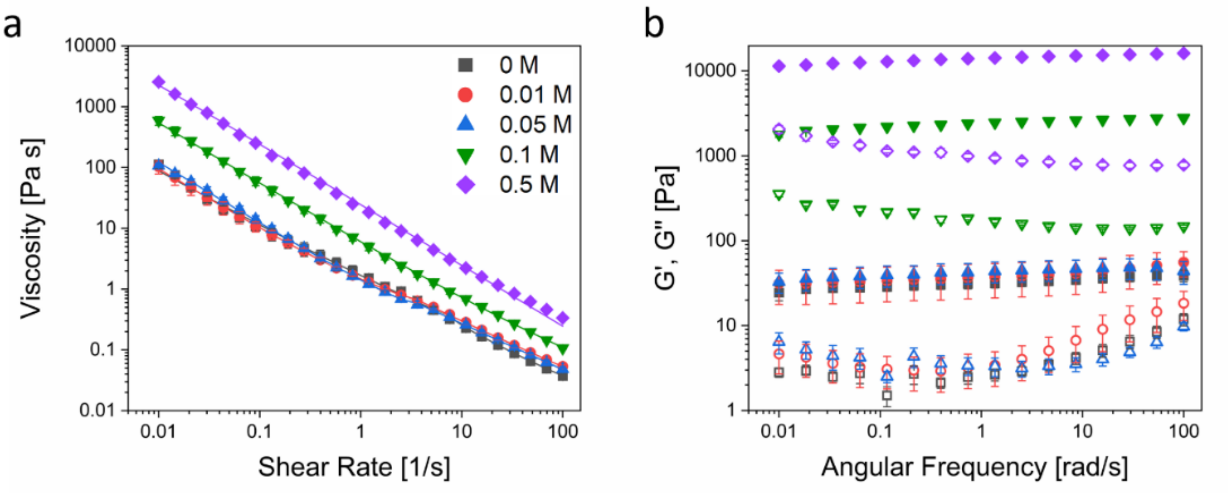

Figure 6.7. a) Steady shear rheology and b) oscillatory rheology (filled symbols represent G' and hollow symbols represent G'') of 0.40 vol % B-MXenes at 0 M (black squares), 0.01 M (red circles), 0.05 M (blue triangles), 0.1 M (green upside-down triangles), and 0.5 M (purple diamonds). Error bars represent standard error of three to four runs.

	Region 1			**Region 3**		
Salt Concentration (M)	Yield Stress (Pa)	K (Pa s^n)	n	Yield Stress (Pa)	K (Pa s^n)	n
0	0.65	1.03	0.33	2.19	0.06	0.17
0.01	0.94	0.53	0.77	0.94	0.97	0.33
0.05	1.21	0.20	0.95	0	1.55	0.24
0.1	5.34	0.68	0.46	-	-	-
0.5	21.74	0.001	0.81	-	-	-

Table 6.3. Herschel-Bulkley model fits for steady shear behavior of 0.40 vol % B-MXenes.

A nearly complete liquid crystal phase persisted as the MXene concentration was increased to 0.60 vol %. Weaving birefringent domains were still observed in the dispersion; however, the higher MXene concentration appeared to increase the packing of the dispersion, resulting in less intense birefringence than what was observed at 0.40 vol %/0 M (**Figure 6.8a**). It should also be noted that the opacity of MXene dispersions begins to limit the ability of transmitted polarized light to observe microstructural changes at higher MXene concentrations. The microscopy image of the 0.60 vol %/0 M dispersion without cross polarization shows a denser structure compared to the lower concentrations. Upon addition of NaCl to the 0.60 vol % B-MXene dispersions, flocculation was readily induced. At 0.01 M, flocs appeared with some dense structures of ~10 μm diameter throughout (**Figure 6.8b**). Aligned domains were scattered throughout the dispersion alongside these flocs. Upon increasing the salt content to 0.05 M and 0.1 M, denser and larger flocs dominated the microstructure and caused increased structural separation, though small areas contained birefringent domains (**Figure 6.8c,d**). At 0.5 M, the 0.60 vol % dispersion became fully flocculated with a broken and discontinuous structure (**Figure 6.8e**).

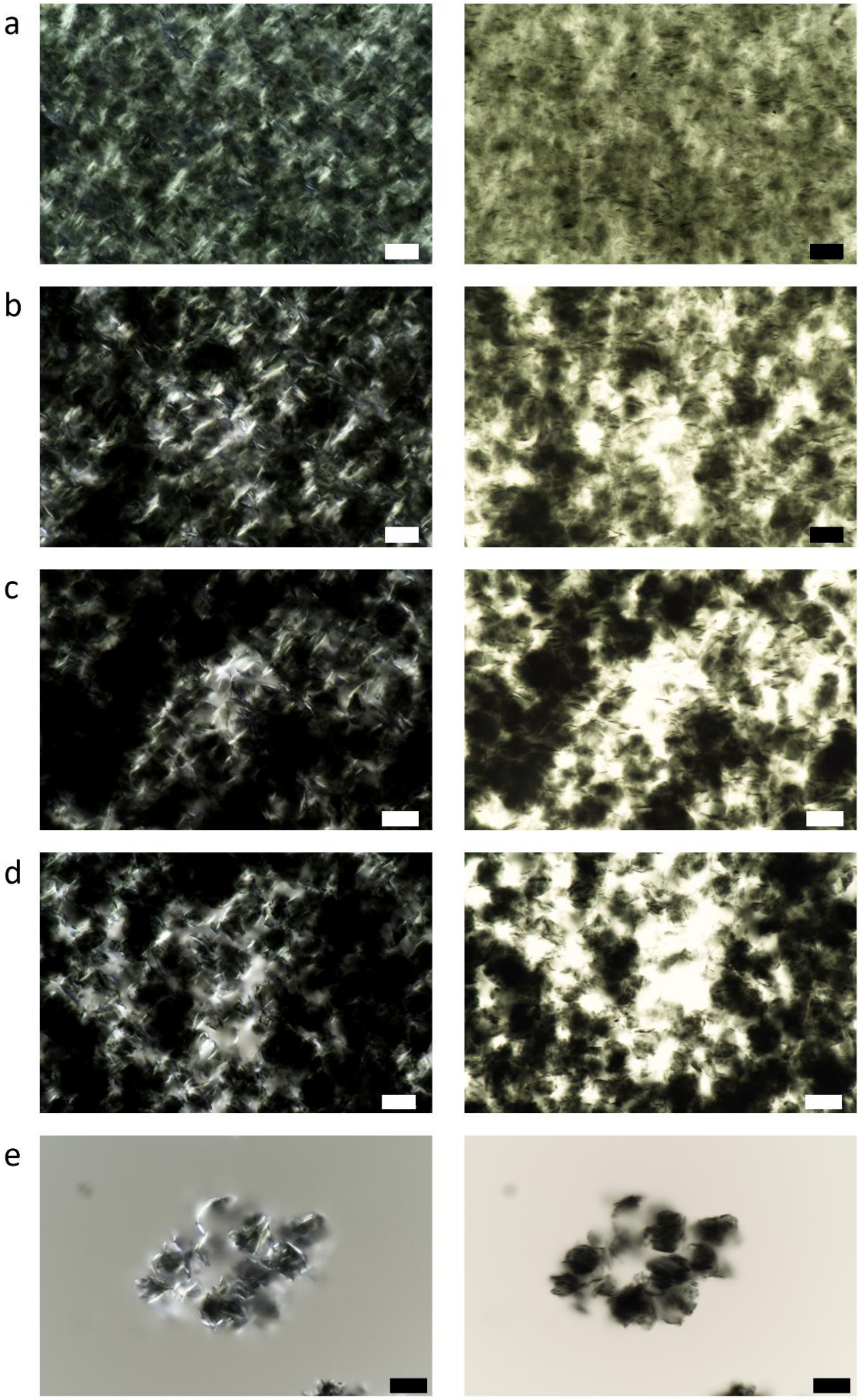

Figure 6.8. Optical microscopy images of 0.60 vol % B-MXenes at a) 0 M, b) 0.01 M, c) 0.05 M, d) 0.1 M, and e) 0.5 M. Left column images are under partially cross polarization and right column images are without cross polarization. Scale bars represent 10 μm.

The steady shear behavior of the 0.60 vol % B-MXene dispersions showed an increase in viscosity with increasing salt concentration through 0.05 M (**Figure 6.9a**). At 0.1 M, the low shear viscosity dropped slightly to ~2100 Pa s, compared to the low shear viscosity of ~3300 Pa s at 0.05 M. Viscosity further decreased at 0.5 M, with a low shear viscosity of ~330 Pa s. The high shear viscosity (at a shear rate of 100 s^{-1}) of the 0.5 M dispersion fell below that of the 0.60 vol % with no salt added. Similar to the drop in viscosity observed in high salt concentrations of 0.25 vol % B-MXenes, this change was attributed to the network breakdown and dense flocculation that occurred as a result of the compressed EDL.[151] A viscosity hesitation point was also observed in the 0.60 vol %/0.01 M. When the viscosity data for this dispersion was fitted to the Herschel-Bulkley model in separate sections corresponding to three region behavior, Region 3 resulted in a yield stress of 0 (**Table 6.4**). This dispersion also exhibited a sharp increase in shear stress in Region 3 that surpassed the yield stress of the dispersion, indicating behavior of a shear-thinning power law fluid in the high shear region (**Figure 6.9b**). This follows with expected behavior of a nearly complete liquid crystal, in which the high shear region consists of domains aligned with the pre-established flow.[64, 148]

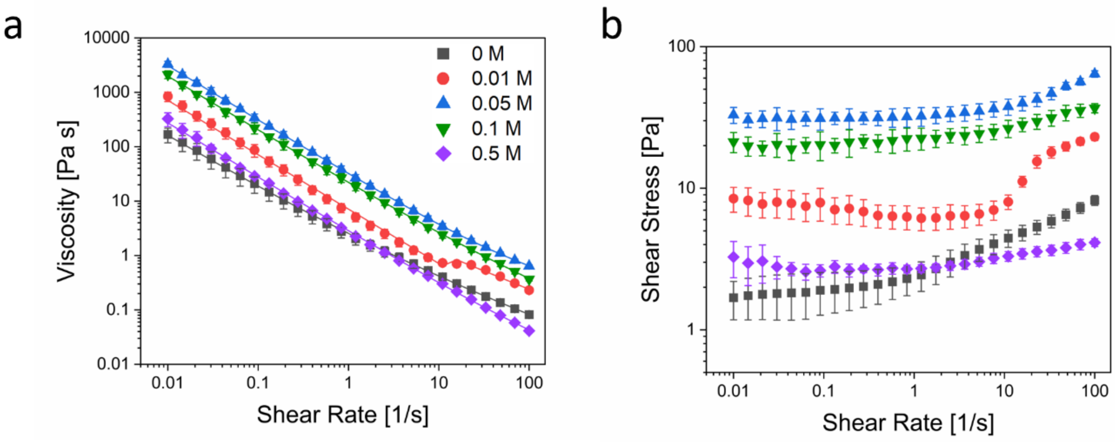

Figure 6.9 Steady shear rheology with a) viscosity as a function of shear rate and b) shear stress as a function of shear rate of 0.60 vol % B-MXenes at 0 M (black squares), 0.01 M (red circles), 0.05 M (blue triangles), 0.1 M (green upside-down triangles), and 0.5 M (purple diamonds). Error bars represent standard error of three to four runs.

	Region 1			**Region 3**		
Salt Concentration (M)	Yield Stress (Pa)	K (Pa s^n)	n	Yield Stress (Pa)	K (Pa s^n)	n
0	1.43	1.12	0.39	-	-	-
0.01	6.07	1.05	0	0	5.38	0.32
0.05	30.9	1.33	0.70	-	-	-
0.1	19.4	2.74	0.41	-	-	-
0.5	2.73	0.13	0.55	-	-	-

Table 6.4. Herschel-Bulkley model fits for steady shear behavior of 0.60 vol % B-MXenes.

Oscillatory rheology exhibited similar trends to viscosity behavior with increasing NaCl concentrations (**Figure 6.10**). Storage and loss moduli both increased through 0.05 M, with a slight decrease in both moduli at 0.1 M and a more pronounced decrease at 0.5 M. G' maintained a frequency-independent behavior throughout, with a slight exception of 0.60 vol %/0 M at low frequencies in which a step-like decrease was observed. In the 0.05 M and 0.1 M NaCl dispersions, the high frequency G'' behavior switched from a positive to a slightly negative slope, indicative of gel-like behavior. This, along with the large increase in magnitude of G', suggested that for 0.60 vol % B-MXenes, a minimum salt content of 0.05 M induced gelation.[29, 102]

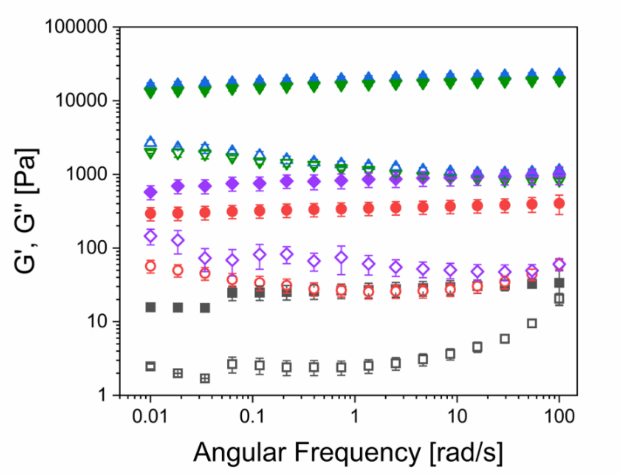

Figure 6.10. Oscillatory rheology of 0.60 vol % B-MXenes at 0 M (black squares), 0.01 M (red circles), 0.05 M (blue triangles), 0.1 M (green upside-down triangles), and 0.5 M (purple diamonds). Filled symbols represent G' and hollow symbols represent G''. Error bars represent standard error of three to four runs.

Increasing the MXene content to 0.80 vol % resulted in slight flocculation at 0 M (**Figure 6.11a**). Based on the more in-depth discussion of 0.80 vol % B-MXenes with no salt added in Chapter 4, this dispersion is classified as a nearly complete liquid crystalline phase with small flocs dispersed throughout what is otherwise a fairly continuous structure. Upon addition of 0.01 M NaCl, these flocs increased in size and density and resulted in a linked or chain-like structure of loosely connected flocs surrounding biphasic areas (**Figure 6.11b**). At 0.05 M, the density of the flocs increased and began to take on a more defined circle-like structure (**Figure 6.11c**). The increased floc density and definition caused greater opacity of the dispersion, leading to difficulty in observing the dispersion microstructure under cross polarized light. The dispersion opacity worsened at 0.1 M NaCl, though some small, scattered domains could be observed (**Figure 6.11d**). Optical microscopy without the cross polarized configuration showed similar defined, dense flocs as observed at 0.05 M, though with a more connected structure that likely contributed to the increased dispersion opacity.

The steady shear behavior of the 0.80 vol % B-MXene dispersions did not vary greatly as a result of salt addition, with the exception of 0.01 M (**Figure 6.12a**). The 0.80 vol %/0.01 M exhibited a slight decrease in viscosity compared to the 0 M dispersion, decreasing from ~1700 Pa s to ~800 Pa s. G' and G'' also saw similar behavior with an initial decrease at 0.01 M NaCl followed by increasing values at 0.05 and 0.1 M (**Figure 6.12b**). As previously discussed, this drop in rheological properties was attributed to the compression of the EDL of the MXene sheets, though notably, this was at a lower NaCl concentration than the previous B-MXene dispersions discussed prior that typically saw a decrease in rheological properties at 0.05-0.5 M. Decreases in rheological properties as a result of low salt concentration have been observed in nanoclay research and is attributed to network breakdown from decreased repulsive interparticle interactions.[88, 151]

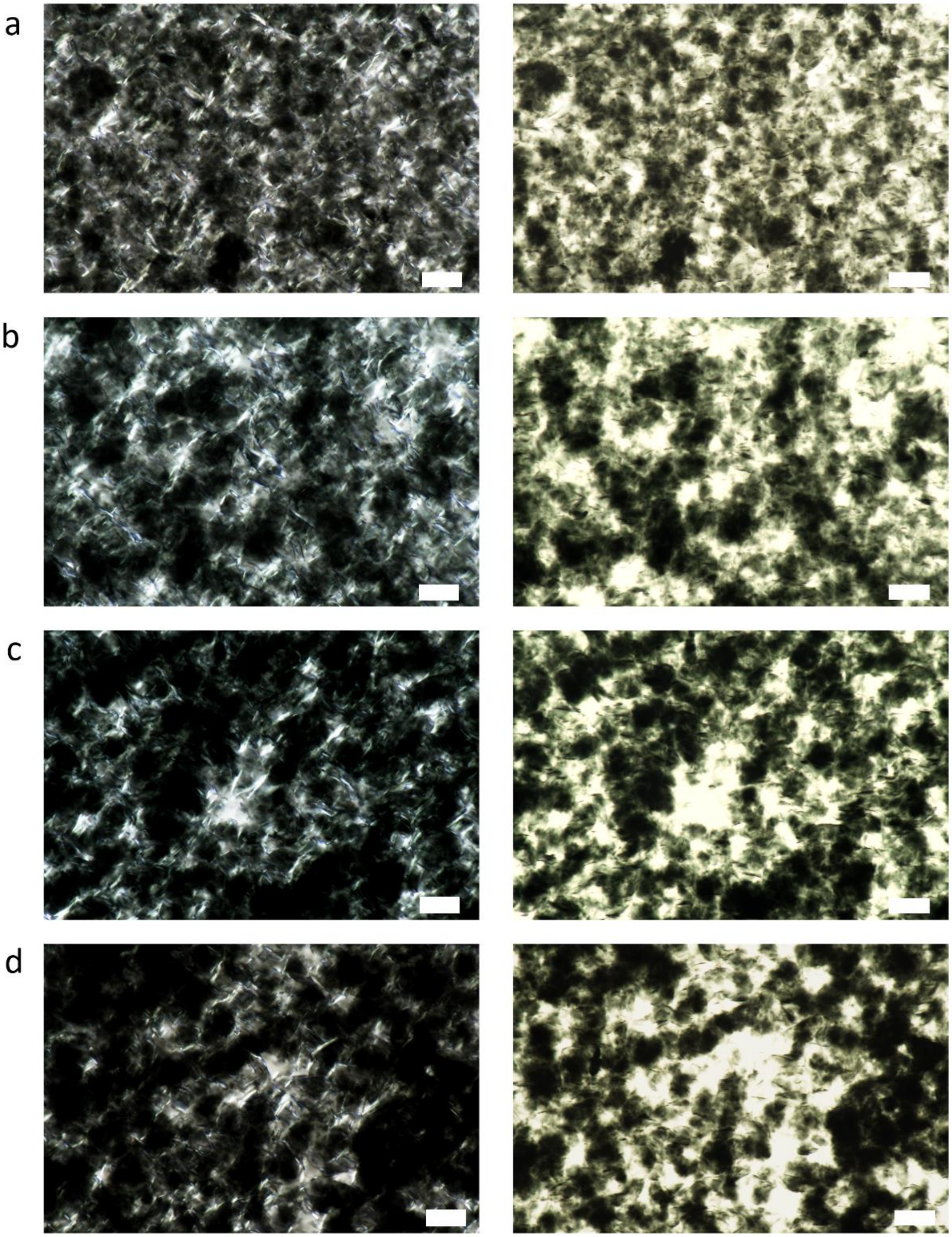

Figure 6.11. Optical microscopy images of 0.80 vol % B-MXenes at a) 0 M, b) 0.01 M, c) 0.05 M, and d) 0.1 M. Left column images are under partially cross polarization and right column images are without cross polarization. Scale bars represent 10 μm.

The optical microscopy images in **Figure 6.11** show a drastic change in structure upon addition of 0.01 M NaCl, indicating this was likely the cause of the drop in rheological properties. The subsequent increase in both viscosity and viscoelastic moduli at salt concentrations of 0.05 and 0.1 M align with observations in nanoclay literature as well, in which rheological properties increased after the initial decrease at low salt concentrations due to increased interparticle attraction from further compressed EDLs.[151] Similar to 0.60 vol % B-MXenes, gelation was likely induced in 0.80 vol % B-MXenes at 0.05 M as determined by the change in high frequency behavior of G’’ and large increase in magnitude of G’.[102]

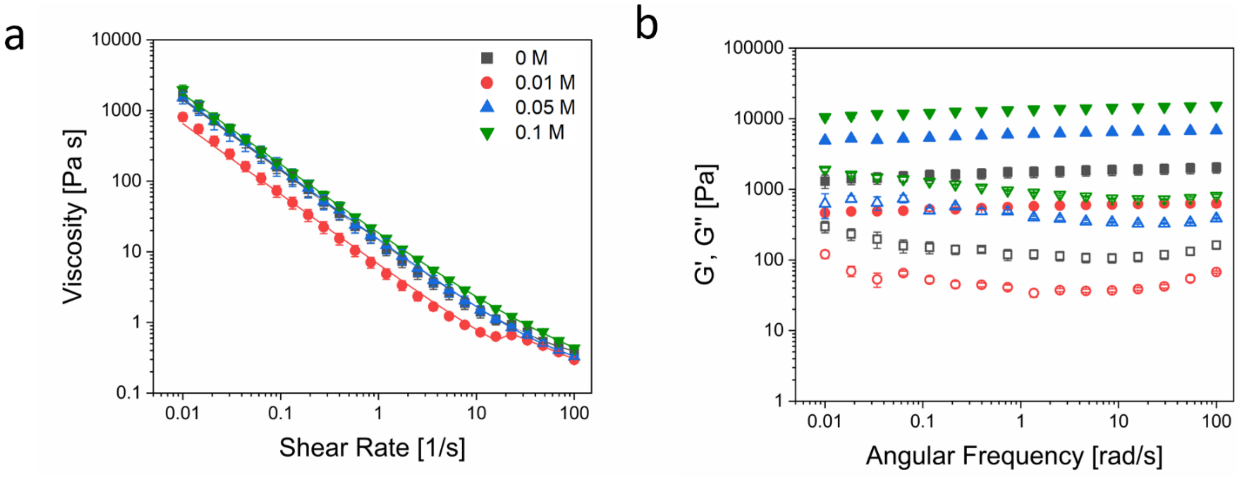

Figure 6.12 a) Steady shear rheology and b) oscillatory rheology (filled symbols represent G’ and hollow symbols represent G’’) of 0.80 vol % B-MXenes at 0 M (black squares), 0.01 M (red circles), 0.05 M (blue triangles), and 0.1 M (green upside-down triangles). Error bars represent standard error of three to four runs.

	Region 1			**Region 3**		
Salt Concentration (M)	Yield Stress (Pa)	K (Pa s^n)	n	Yield Stress (Pa)	K (Pa s^n)	n
0	14.2	0.25	1.00	-	-	-
0.01	6.51	0.14	1.00	0	3.99	0.44
0.05	14.8	0.21	0.97	-	-	-
0.1	17.1	1.40	0.64	-	-	-

Table 6.5 Herschel-Bulkley model fits for steady shear behavior of 0.80 vol % B-MXenes.

At 1.00 vol %/0 M B-MXenes, dense flocs extended throughout the sample though the microstructure remained intact (**Figure 6.13a**). At 0.01 M NaCl, the flocs increased in size with many reaching over 10μm in diameter (**Figure 6.13b**). Under cross-polarized light, the sample appeared so densely flocculated that very few aligned domains could be observed. As salt concentration increased to 0.05 and 0.1 M, the opacity of the MXene sample made it increasingly difficult to obtain cross-polarized images and study any microstructural changes; however, what could be seen in such images indicated that flocculation drastically increased with increasing NaCl concentration (**Figure 6.13c,d**).

In Chapter 5, it was discussed that 1.00 vol% bimodal MXenes are in a nematic gel phase due to increased rheological properties and the gel-like behavior found in the oscillatory measurements. Rheological measurements of 1.00 vol % B-MXene dispersions showed an immediate decrease in viscosity, yield stress, and viscoelastic moduli at 0.01 M NaCl (**Figure 6.14, Table 6.6**). The 1.00 vol %/0.05 M dispersion exhibited similar rheological properties to the 0.01 M dispersion. As determined for the similar behavior observed in 0.80 vol % B-MXenes with low salt concentration, this decrease in rheological properties upon salt addition was due to the compression of the electrical double layer and weakening of the percolated network.[151, 154] Interestingly, the high frequency behavior of G” changes at 0.01 and 0.05 M to an increasing slope from the decreasing slope of 0 M that is indicative of gel-like behavior. This further supports that the percolated, gel structure of the 1.00 vol %/0 M B-MXene dispersion was initially weakened upon salt addition, causing the drop in rheological properties. The increase in viscosity and moduli observed in 1.00 vol %/0.1 M, as well as the reappearance of gel-like G” behavior at high frequencies, was then ascribed to further EDL compression and flocculation resulting from the increased attractive energy between MXene sheets and reforming of a stronger microstructural network with the addition of more NaCl.[151]

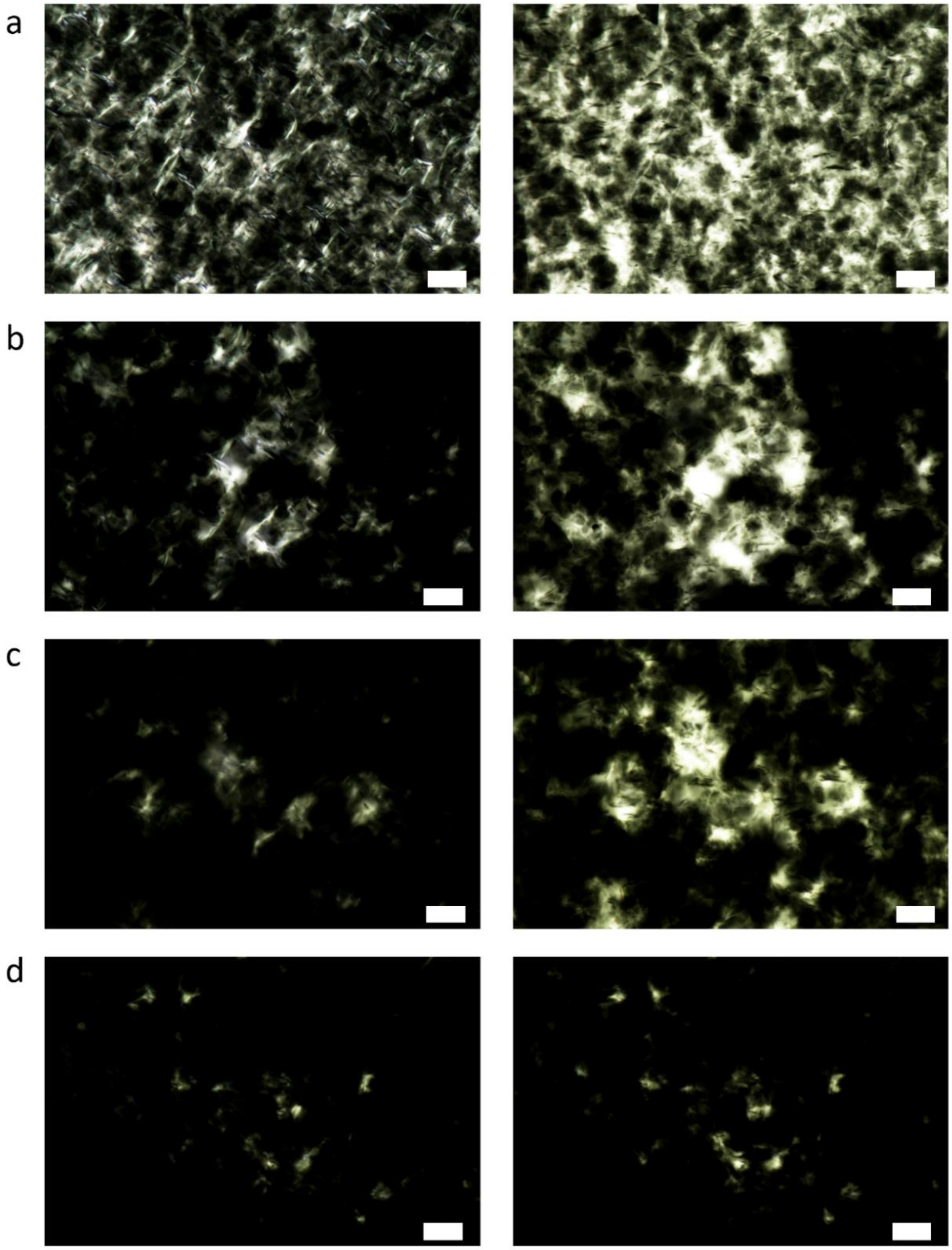

Figure 6.13. Optical microscopy images of 1.00 vol % B-MXenes at a) 0 M, b) 0.01 M, c) 0.05 M, d) 0.1 M, and e) 0.5 M. Left column images are under partially cross polarization and right column images are without cross polarization. Scale bars represent 10 μm.

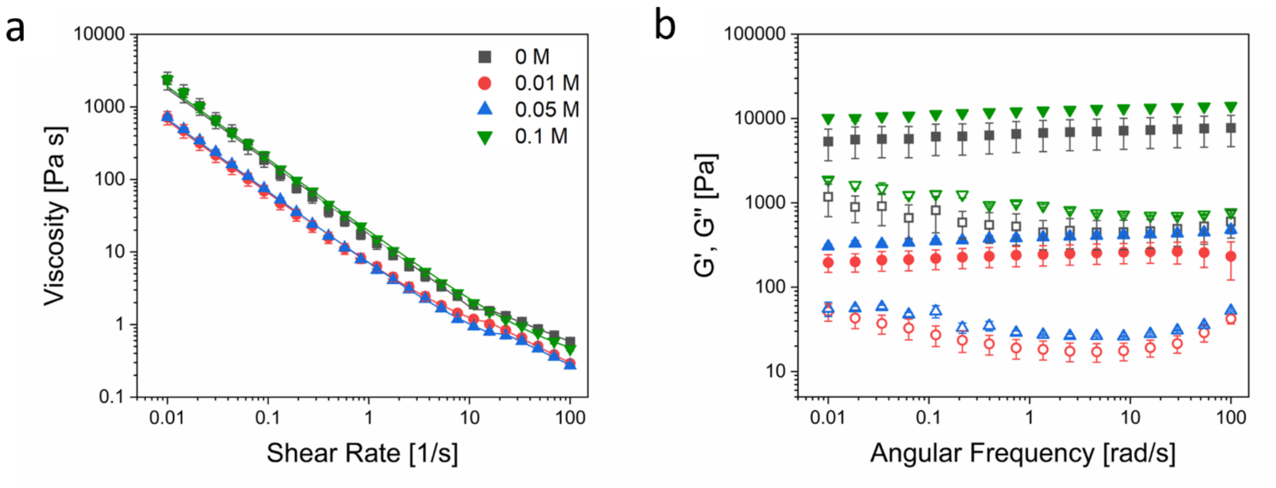

Figure 6.14. a) Steady shear rheology and b) oscillatory rheology (filled symbols represent G' and hollow symbols represent G'') of 1.00 vol % B-MXenes at 0 M (black squares), 0.01 M (red circles), 0.05 M (blue triangles), and 0.1 M (green upside-down triangles). Error bars represent standard error of three to four runs.

	Region 1			Region 3		
Salt Concentration (M)	Yield Stress (Pa)	K (Pa s^n)	n	Yield Stress (Pa)	K (Pa s^n)	n
0	17.5	0.25	0	0.01	7.29	0.45
0.01	6.41	0.72	0.93	0	7.33	0.31
0.05	6.79	0.34	1.00	0.06	5.84	0.34
0.1	19.0	0.47	0.90	-	-	-

Table 6.6. Herschel-Bulkley model fits for steady shear behavior of 1.00 vol % B-MXenes.

6.3 Conclusions

The work in this chapter provided insights into the phase behavior and associated rheological properties of bimodal MXenes at varying concentrations and ionic strengths. From these results, understanding is gained of methods to tune bimodal MXenes to achieve aligned and stable phases, as well as the rheological properties necessary for various fluid-phase processing. The negatively charged surfaces and positively charged edges of the MXene sheets coupled with NaCl salt induced electrical double layer interactions competing with van der Waals interactions, resulting in a rich phase behavior similar to various nanoclays.[85, 151] Salt addition resulted in maintaining the nematic ordering at low salt content while simultaneously adjusting rheological properties, emphasizing the practicality of using NaCl as a rheological modifier. However, flocculation occurred in all B-MXene dispersions at high salt concentrations, reiterating the importance of understanding the balance between salt concentration and microstructural changes that could affect processability.

To summarize the results from this work, a phase diagram of the B-MXene/NaCl system is proposed in **Figure 6.15a**. Nematic liquid crystalline phases were achieved at 0.40 vol % B-MXenes, though rheological properties could be adjusted at lower concentrations through utilizing NaCl as a rheological modifier. Without salt addition, nematic gels with increased rheological properties were formed 1.00 vol % B-MXenes, though by utilizing NaCl as an additive, gelation could be induced in dispersions with MXene concentrations as low as 0.40 vol %. High NaCl concentrations of 0.5 M resulted in flocculation and microstructural breakage in all concentrations of MXene dispersions studied, emphasizing the balance that must be kept in tuning dispersions to simultaneously enhance properties and maintain stability.

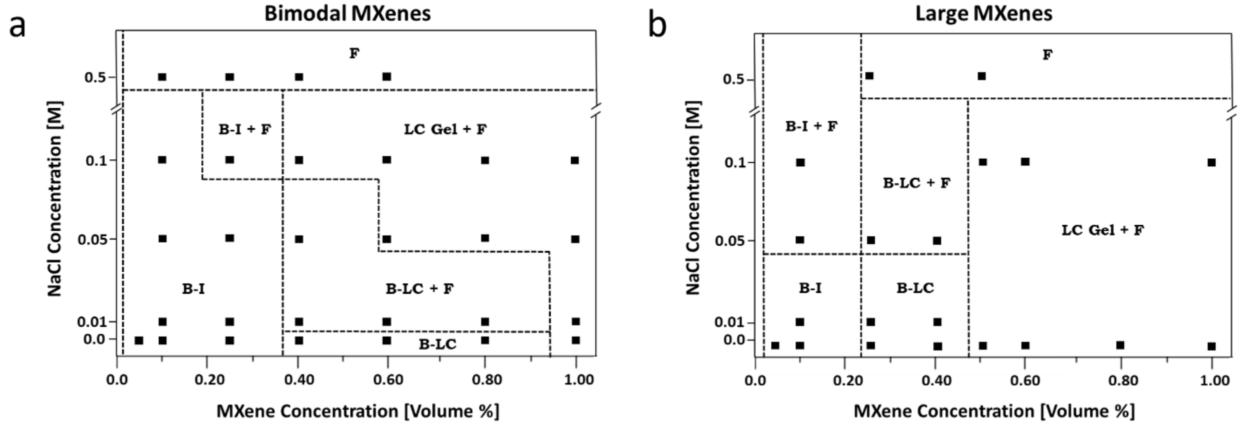

Figure 6.15. a) Phase diagram of the B-MXene/NaCl system, where B-I indicates a biphasic, mostly isotropic phase, B-LC indicates a biphasic, nearly complete liquid crystal phase, LC Gel indicates a nematic gel, and F indicates flocs. b) Phase diagram of the L-MXene/NaCl system, produced from the data obtained by previous graduate student, Dr. Fatima Hamade.[155]

Figure 6.15b depicts the L-MXene/NaCl phase diagram produced from research completed by a previous graduate student that worked on the MXene-NaCl project, Dr. Fatima Hamade. Dispersions of large MXenes were observed to reach nearly complete liquid crystalline phases at lower sheet concentrations than bimodal MXene dispersions, as also discussed in Chapter 5; however, the bimodal MXenes were more resistant to severe flocculation and jamming of the sheets. Bimodal MXenes exhibited a more complex phase behavior than large MXenes, such as induced gelation at lower MXene concentrations with added NaCl. The increased phase behavior complexity of the bimodal MXenes was likely due to the effects of the included small sheets on interparticle interactions. The selective polydispersity of the B-MXene dispersions likely contributed to the wider biphasic region observed in the lower salt concentrations compared to the L-MXenes. In addition to its resistance to aggregation and jamming, this research highlights the increased processability and tunability of bimodal MXene dispersions through both MXene and salt content.

Overall, it has been shown that aqueous B-MXene dispersions can readily form nematic liquid crystalline phases, while the addition of NaCl salt can be utilized as rheological modifier to achieve desired properties without requiring increased MXene content. Rheological properties of B-MXenes with salt displayed increased viscoelastic and steady shear properties by orders of magnitude indicating stronger network formation, elasticity, yield stresses, and viscosities due to electroviscous effect and compressed EDL of the charged sheets. Previous reports with similar trends in the rheological behavior for $Ti_3C_2T_x$ and ultra-large GO dispersions have shown potential processing capabilities for wet spinning, dry spinning, extrusion printing, and spray coating,[23, 84] which suggests potential processing routes for the dispersions studied in this work. Results from this work offer an interesting connection between the microstructures of MXene, GO, and nanoclay dispersions, extending the fundamental science governing the dispersion behavior of 2D materials.

Chapter 7 – Conclusions

The research in this dissertation elucidates the effects of sheet size and salt addition on aqueous MXene dispersion phase behavior and associated rheological properties. The knowledge gained from this work provides a deeper fundamental understanding of MXene dispersion behavior and is of practical importance in increasing the processability of the dispersions to enhance final properties of advanced materials. This research provides insights into the relationship between structure and rheological properties and allows increased predictability into the processing of the materials. This, in turn, enhances the accuracy of predicting the final properties of processed dispersions that can then round out the structure-property-processing relationships of aqueous MXene dispersions. The research undertaken for this dissertation resulted in the first MXene size-dependent phase diagram and MXene-NaCl phase diagram focused on the selectively polydisperse bimodal MXene dispersion.

The first half of this dissertation focused primarily on the sheet size effects on aqueous MXene dispersions. The aim of this work was the understand how the average size of MXene sheets affects the alignment of the sheets in concentration-dependent lyotropic liquid crystalline phases and the resulting changes in rheological properties. Based on Onsager's theory, the aspect ratio (length/diameter) of an anisotropic nanomaterial is a key determinant in of the concentration required to transition from isotropic to biphasic to liquid crystalline phases.[40] From this theory and previous exploration of GO size-dependent phase behavior,[14] it was hypothesized that large MXenes would readily align into a liquid crystal and small MXenes would not form any aligned phases due to their respective excluded volume effects. Selectively polydisperse dispersions of large and small MXenes were hypothesized to form a liquid crystalline phase at low concentrations due to the increased packing alignment from the addition of the small sheets. To study this, polydisperse MXene sheets were separated into large and small sheets through centrifugation and redispersion into three size fractions: large MXenes with ~3 μm in largest lateral dimension (denoted as L-MXenes), small MXenes with ~0.3 μm in largest lateral dimension (denoted as S-MXenes), and a bimodal mixture of large and small sheets at a 1:1 volume ratio (denoted as B-MXenes). A range of concentrations of each size fraction were prepared in order to observe the phase transitions and rheological changes as a function of both MXene concentration and sheet size.

Results from this work showed that in line with the hypothesis, L-MXenes readily formed aligned phases; however, upon further increasing of MXene concentration, they were observed through polarized optical microscopy to flocculate or aggregate before a single phase nematic liquid crystal could be achieved. This observation highlighted the importance of visually observing the MXene dispersions under polarized microscopy in conjunction with the rheological characterization of each dispersion. Though rheological properties may have appeared sufficient for processability in some higher concentrations of L-MXenes, the presence of aggregates indicated potential issues in fluid-phase processing. Severe aggregation not only indicates dispersion instability but also suggests future manufacturing problems such as nozzle clogging in processes like direct-ink-writing.

For the S-MXene dispersions, as hypothesized, a complete liquid crystal phase was not achieved. Rather, fine textures were observed in higher concentrations that were reminiscent of textures seen in dispersions of small GO sheets that were found difficult to utilize in fluid-phase processing.[144] It is likely that the fine textures observed in S-MXenes indicate that these dispersions would not result in high processability. It should be noted, though, that S-MXenes were not observed to severely aggregate. However, their increased stability over L-MXenes would likely not allow for any higher processability due to the lack of nematic liquid crystalline ordering. This clarity into the behavior of S-MXenes will allow future researchers to avoid possibly high cost and time-consuming experiments in the efforts to process dispersions consisting of only small MXene sheets.

The phase behavior and rheological properties that were observed in B-MXenes did not follow the original hypothesis that stated that a liquid crystal phase could be achieved at lower concentrations with the inclusion of small MXene sheets as compared to dispersions consisting of only large MXene sheets. Rather, the B-MXenes did not form extended alignment until 0.40 vol %, compared to the 0.25 vol % L-MXenes that exhibited similar birefringent microstructures. Despite the higher concentration requirement of B-MXenes to form a nearly complete liquid crystal, they were also observed to be more resistant to aggregation. Polarized optical microscopy provided insight into their increased stability with the onset of aggregation occurring at higher concentrations than L-MXenes, and the smaller diameter of the aggregates that formed as compared to the L-MXene aggregates. Therefore, the B-MXenes appeared to be the best candidate for fluid-phase manufacturing methods with their ability to form extended aligned structures and resistance to aggregation.

The results of the first half of this work provide clarity on utilizing size fractionated MXenes for increased stability and microstructural alignment in additive-free, aqueous dispersions. This research shows that MXene sheet size can be a tunable parameter utilized to achieve desired rheological properties and aligned phases without the use of additives or rheological modifiers. This research offers evidence that by using a bimodal dispersion of large and small sized MXene sheets, aggregation found in monodisperse large MXenes can be retarded while still achieving the long-range ordering necessary to enhance alignment in materials produced through fluid-phase processing methods. While this research only focused on a 1:1 volume ratio of large and small MXenes to comprise the B-MXene dispersions, future directions of this research should include adjusting these ratios to observe the resulting changes in rheological properties, concentration requirements for liquid crystal formation, and aggregation tendencies. New imaging techniques should also be utilized to provide a more quantifiable comparison in the different textures and microstructures observed in the size fractionated MXenes, most notably the finer structure of the S-MXenes. Early discussions with fellow colloid researchers brought forth ideas of color-processed microscopy imaging with a PolScope, based on director alignment in MXene dispersions with liquid crystalline textures. While obtaining access to proper equipment for this advanced imaging technique is beyond the scope of this dissertation, the insight such quantitative texture comparisons could provide lends this as a promising future direction of MXene dispersion research.

The results of this research on MXene size polydispersity will also support future research in the processing of MXene dispersions into aligned structures, such as in direct-ink-writing and fiber spinning. Through understanding the tunability of MXene dispersions by selection of sheet size, future researchers can better predict final properties of processed dispersions and more easily achieve desired results without the need to use additives to achieve required rheological properties for processing. Future directions to further enhance this knowledge include the use of scattering methods to better probe the spacing and alignment of the dispersed MXene sheets. This would provide a greater understanding of the structural changes and differences of the size fractionated MXene sheets. While originally planned to be included in the scope of this dissertation, advanced rheological measurements using small angle neutron scattering (Rheo-SANS) could not be completed within this work due to extended reactor shutdowns at the NIST Center for Neutron

Research that resulted in a subsequent global limitation on neutron and X-ray scattering accessibility. However, pursuing this method for elucidation of changes in MXene sheet spacing as a result of decreased or selective size polydispersity would provide valuable knowledge to further progress development of MXene inks and devices.

The second half of this research focused on the effects of salt addition on the phase behavior and associated rheological properties of bimodal MXenes. Based on the structural similarity of MXenes to nanoclays, it was hypothesized that by adding NaCl to aqueous MXene dispersions, a rich phase behavior would develop. Due to their ability to form extended aligned structures and their resistance to aggregation, B-MXenes were the focus of this work. This research found that NaCl could be used as a rheological modifier to aqueous B-MXene dispersions by adjusting their rheological properties through salt concentration alone. At low B-MXene concentrations, the addition of a small amount of salt (0.01-0.05 M) would generally result in increased viscosity, yield stress, and viscoelastic moduli that would make the dispersions more processable in many fluid-phase manufacturing methods. At higher B-MXene concentrations of 0.40 vol % or greater, the addition of NaCl induced gelation and resulted in a stronger percolated network while maintaining nematic ordering. However, the effect of NaCl addition on rheological properties at higher B-MXene concentrations is more nuanced than at lower concentrations. The preexisting percolated network of more highly concentrated B-MXene dispersions can also be initially weakened by the addition of small amounts of NaCl, as is the case for 0.80 vol % and 1.00 vol % B-MXenes. Viscosity and storage and loss moduli then increase upon further raising the concentration of NaCl in these dispersions with higher MXene concentrations. While this insinuates a more complex relationship between salt content and dispersion properties, it also emphasizes the increased tunability of the dispersions through adjusting only MXene and salt concentrations.

Dispersions containing 0.5 M NaCl resulted in dense flocs and breakage of the microstructure at all MXene concentrations. This was due to the highly compressed EDL surrounding the charged MXene sheets, where the Debye length had decreased to 0.43 nm from 3.04 nm at 0.01 M. This allowed for the MXene sheets to come in closer contact with one another, and thus, the attractive van der Waals forces could dominate and induce dense flocculation. Rheological properties of B-MXene dispersions at 0.5 M were varied, but generally at low MXene concentration, the high salt content increased properties and at high MXene concentration, the high salt content decreased rheological properties. However, it should be noted that the discontinuous microstructure and large flocs in these dispersions can cause misrepresentation of rheological properties. The lack of a continuous network of MXenes in these dispersions also indicates that B-MXene dispersions at 0.5 M would not be conducive to fluid-phase processing or manufacturing of efficient MXene-based devices.

Dr. Fatima Hamade, a previous graduate student in Dr. Virginia Davis's lab group, investigated NaCl addition to L-MXenes in a similar manner. Compared to L-MXene/NaCl systems, B-MXenes exhibited a more complex phase behavior. The increased complexity of bimodal MXenes is likely due to the effects of the included small sheets on interparticle interactions. The selective polydispersity that is the crux of B-MXene dispersions likely contributed to a wider biphasic region observed in the lower salt concentrations compared to the L-MXenes. In addition to their resistance to aggregation and jamming, this emphasizes the increased tunability and processability of bimodal MXene dispersions through both MXene and salt content.

The results from this research provide novel insight into the effects of both sheet size and salt addition on the phase behavior and associated rheological properties of aqueous MXene dispersions, thereby answering the foundational questions that prompted this research. Through extensive rheological characterization and study of microstructural changes, the relationships of phase transitions and aqueous dispersion behavior as a function of MXene sheet size, concentration, and ionic strength were developed. The fundamental understanding this research will facilitate MXene application development, as these dispersion properties and behaviors are directly related to dispersion processability and device performance. Preliminary research into the printability of the size fractionated MXene dispersions investigated in this work has begun in Dr. Virginia Davis's lab, led by a fellow graduate student, Francis Mekunye. The goal of Francis's work will be to relate the rheological properties and phase behavior of the selectively polydisperse MXene dispersions discussed in this dissertation to the print quality and device performance, thereby further developing the structure-property-processing relationships of aqueous MXene dispersions. This future work will be guided by the knowledge obtained from this dissertation, allowing for more strategic printing trials and a deeper understanding of why specific inks will likely result in higher printability and device performance. The knowledge of dispersion tunability through sheet size selection and NaCl addition will enhance the future work of developing higher quality MXene inks and MXene-based devices with less need for time-consuming ink formulation and testing efforts. Through understanding the complexities of MXene behavior, this relatively new 2D material system will be better utilized by present and future researchers to enhance fluid-phase processing and development of advanced materials with less time and financial obligations than many trial-and-error application methods. The knowledge gained from this dissertation extends beyond MXenes to the overarching field of 2D nanomaterials, by broadening the understanding of their similar, though complex, behavioral framework and formulating relationships among materials in the 2D family.

References

1. Lekkerkerker, H. N. W.; Vroege, G. J., Liquid Crystal Phase Transitions in Suspensions of Mineral Colloids: New Life from Old Roots. *Philosophical Transactions of the Royal Society A: Mathematical, Physical and Engineering Sciences* **2013,** *371* (1988).

2. Davis, V. A., Anisotropic Nanomaterial Liquid Crystals: From Fiber Spinning to Additive Manufacturing. *Langmuir* **2023,** *39* (11), 3829-3836.

3. Lagerwall, J. P. F.; Scalia, G., A New Era for Liquid Crystal Research: Applications of Liquid Crystals in Soft Matter Nano-, Bio- and Microtechnology. *Current Applied Physics* **2012,** *12* (6), 1387-1412.

4. Dierking, I.; Martins Figueiredo Neto, A., Novel Trends in Lyotropic Liquid Crystals. *Crystals* **2020,** *10* (7), 604.

5. Davis, V. A.; Parra-Vasquez, A. N. G.; Green, M. J.; Rai, P. K.; Behabtu, N.; Prieto, V.; Booker, R. D.; Schmidt, J.; Kesselman, E.; Zhou, W.; Fan, H.; Adams, W. W.; Hauge, R. H.; Fischer, J. E.; Cohen, Y.; Talmon, Y.; Smalley, R. E.; Pasquali, M., True Solutions of Single-Walled Carbon Nanotubes for Assembly into Macroscopic Materials. *Nature Nanotechnology* **2009,** *4* (12), 830-834.

6. van der Kooij, F. M.; Lekkerkerker, H. N. W., Formation of Nematic Liquid Crystals in Suspensions of Hard Colloidal Platelets. *The Journal of Physical Chemistry B* **1998,** *102* (40), 7829-7832.

7. Speranza, A.; Sollich, P., Simplified Onsager Theory for Isotropic–Nematic Phase Equilibria of Length Polydisperse Hard Rods. *The Journal of Chemical Physics* **2002,** *117* (11), 5421-5436.

8. Bruckner, J. R.; Kuhnhold, A.; Honorato-Rios, C.; Schilling, T.; Lagerwall, J. P. F., Enhancing Self-Assembly in Cellulose Nanocrystal Suspensions Using High-Permittivity Solvents. *Langmuir* **2016,** *32* (38), 9854-9862.

9. Xu, T.; Davis, V. A., Liquid Crystalline Phase Behavior of Silica Nanorods in Dimethyl Sulfoxide and Water. *Langmuir* **2014,** *30* (16), 4806-4813.

10. Xu, T.; Davis, V. A., Rheology and Shear-Induced Textures of Silver Nanowire Lyotropic Liquid Crystals. *Journal of Nanomaterials* **2015,** *2015*, 9.

11. Li, L. S.; Walda, J.; Manna, L.; Alivisatos, A. P., Semiconductor Nanorod Liquid Crystals. *Nano Letters* **2002,** *2* (6), 557-560.

12. Jalili, R.; Aminorroaya-Yamini, S.; Benedetti, T. M.; Aboutalebi, S. H.; Chao, Y.; Wallace, G. G.; Officer, D. L., Processable 2D Materials Beyond Graphene: MoS_2 Liquid Crystals and Fibres. *Nanoscale* **2016,** *8* (38), 16862-16867.

13. Mourad, M. C. D.; Byelov, D. V.; Petukhov, A. V.; Matthijs de Winter, D. A.; Verkleij, A. J.; Lekkerkerker, H. N. W., Sol−Gel Transitions and Liquid Crystal Phase Transitions in Concentrated Aqueous Suspensions of Colloidal Gibbsite Platelets. *The Journal of Physical Chemistry B* **2009,** *113* (34), 11604-11613.

14. Jalili, R.; Aboutalebi, S. H.; Esrafilzadeh, D.; Konstantinov, K.; Razal, J. M.; Moulton, S. E.; Wallace, G. G., Formation and Processability of Liquid Crystalline Dispersions of Graphene Oxide. *Materials Horizons* **2014,** *1* (1), 87-91.

15. Er, D.; Li, J.; Naguib, M.; Gogotsi, Y.; Shenoy, V. B., Ti_3C_2 MXene as a High Capacity Electrode Material for Metal (Li, Na, K, Ca) Ion Batteries. *ACS Applied Materials & Interfaces* **2014,** *6* (14), 11173-11179.

16. Ghidiu, M.; Lukatskaya, M. R.; Zhao, M.-Q.; Gogotsi, Y.; Barsoum, M. W., Conductive Two-Dimensional Titanium Carbide ‘Clay’ with High Volumetric Capacitance. *Nature* **2014,** *516* (7529), 78-81.

17. Rasool, K.; Mahmoud, K. A.; Johnson, D. J.; Helal, M.; Berdiyorov, G. R.; Gogotsi, Y., Efficient Antibacterial Membrane Based on Two-Dimensional $Ti_3C_2T_x$ (MXene) Nanosheets. *Scientific Reports* **2017,** *7* (1), 1598.

18. Sarycheva, A.; Polemi, A.; Liu, Y.; Dandekar, K.; Anasori, B.; Gogotsi, Y., 2D Titanium Carbide (MXene) for Wireless Communication. *Science Advances* **2018,** *4* (9), eaau0920.

19. Zhang, C.; Anasori, B.; Seral-Ascaso, A.; Park, S.-H.; McEvoy, N.; Shmeliov, A.; Duesberg, G. S.; Coleman, J. N.; Gogotsi, Y.; Nicolosi, V., Transparent, Flexible, and Conductive 2D Titanium Carbide (MXene) Films with High Volumetric Capacitance. *Advanced Materials* **2017,** *29* (36), 1702678.

20. Anasori, B.; Lukatskaya, M. R.; Gogotsi, Y., 2D Metal Carbides and Nitrides (MXenes) for Energy Storage. *Nature Reviews Materials* **2017,** *2* (2), 16098.

21. Maleski, K.; Mochalin, V. N.; Gogotsi, Y., Dispersions of Two-Dimensional Titanium Carbide MXene in Organic Solvents. *Chemistry of Materials* **2017,** *29* (4), 1632-1640.

22. AlHassoon, K.; Han, M.; Malallah, Y.; Ananthakrishnan, V.; Rakhmanov, R.; Reil, W.; Gogotsi, Y.; Daryoush, A. S., Conductivity Extraction of Thin $Ti_3C_2T_x$ MXene Films over 1–10 GHz Using Capacitively Coupled Test-Fixture. *Applied Physics Letters* **2020,** *116* (18), 184101.

23. Zhang, J.; Uzun, S.; Seyedin, S.; Lynch, P. A.; Akuzum, B.; Wang, Z.; Qin, S.; Alhabeb, M.; Shuck, C. E.; Lei, W.; Kumbur, E. C.; Yang, W.; Wang, X.; Dion, G.; Razal, J. M.; Gogotsi, Y., Additive-Free MXene Liquid Crystals and Fibers. *ACS Central Science* **2020,** *6* (2), 254-265.

24. Baravian, C.; Vantelon, D.; Thomas, F., Rheological Determination of Interaction Potential Energy for Aqueous Clay Suspensions. *Langmuir* **2003,** *19*, 8109-8114.

25. Davidson, P.; Batail, P.; Gabriel, J. C. P.; Livage, J.; Sanchez, C.; Bourgaux, C., Mineral Liquid Crystalline Polymers. *Progress in Polymer Science* **1997,** *22* (5), 913-936.

26. Delhorme, M.; Labbez, C.; Jönsson, B., Liquid Crystal Phases in Suspensions of Charged Plate-Like Particles. *The Journal of Physical Chemistry Letters* **2012,** *3* (10), 1315-1320.

27. Gabriel, J.-C.; Davidson, P., New Trends in Colloidal Liquid Crystals Based on Mineral Moieties. *Advanced Materials* **2000,** *12*, 9-20.

28. Gabriel, J.-C. P.; Sanchez, C.; Davidson, P., Observation of Nematic Liquid-Crystal Textures in Aqueous Gels of Smectite Clays. *The Journal of Physical Chemistry* **1996,** *100*, 11139-11143.

29. Mourad, M. C. D.; Wijnhoven, J. E. G. J.; van 't Zand, D. D.; van der Beek, D.; Lekkerkerker, H. N. W., Gelation Versus Liquid Crystal Phase Transitions in Suspensions of Plate-Like Particles. *Philosophical Transactions of the Royal Society A: Mathematical, Physical and Engineering Sciences* **2006,** *364* (1847), 2807-2816.

30. Paineau, E.; Michot, L. J.; Bihannic, I.; Baravian, C., Aqueous Suspensions of Natural Swelling Clay Minerals. 2. Rheological Characterization. *Langmuir* **2011,** *27* (12), 7806-7819.

31. Shahin, A.; Joshi, Y. M., Hyper-Aging Dynamics of Nanoclay Suspension. *Langmuir* **2012,** *28* (13), 5826-5833.

32. Verwey, E. J. W., Theory of the Stability of Lyophobic Colloids. *The Journal of Physical Chemistry* **1947,** *51* (3), 631-636.

33. Fettweis, M.; Baeye, M.; Lee, B. J.; Chen, P.; Yu, J. C. S., Hydro-Meteorological Influences and Multimodal Suspended Particle Size Distributions in the Belgian Nearshore Area (Southern North Sea). *Geo-Marine Letters* **2012,** *32* (2), 123-137.

34. Spencer, K. L.; Wheatland, J. A. T.; Bushby, A. J.; Carr, S. J.; Droppo, I. G.; Manning, A. J., A Structure–Function Based Approach to Floc Hierarchy and Evidence for the Non-Fractal Nature of Natural Sediment Flocs. *Scientific Reports* **2021,** *11* (1), 14012.

35. Kawamoto, H., The History of Liquid Crystal Displays. *Proceedings of the IEEE* **2002,** *90*, 460-500.

36. Sparavigna, A. C., The Earliest Researches on Liquid Crystals. **2019**.

37. Sonin, A. S., Inorganic Lyotropic Liquid Crystals. *Journal of Materials Chemistry* **1998,** *8* (12), 2557-2574.

38. Sonin, A. S., What Are Liquid Crystals? (on the 100th Anniversary of the Discovery). *Journal of Structural Chemistry* **1991,** *32* (1), 111-129.

39. Stanley, W. M., Isolation of a Crystalline Protein Possessing the Properties of Tobacco-Mosaic Virus. *Science* **1935,** *81* (2113), 644-645.

40. Onsager, L., The Effects of Shape on the Interaction of Colloidal Particles. *Annals of the New York Academy of Sciences* **1949,** *51*, 627-659.

41. Fraden, S.; Maret, G.; Caspar, D., Angular Correlations and the Isotropic-Nematic Phase Transition in Suspensions of Tobacco Mosaic Virus. *Physical Review E* **1993,** *48* (4), 2816.

42. Lagerwall, J.; Scalia, G., A New Era for Liquid Crystal Research: Applications of Liquid Crystals in Soft Matter Nano-, Bio- and Microtechnology. *Current Applied Physics* **2012,** *12*, 1387–1412.

43. Andrienko, D., Introduction to Liquid Crystals. *Journal of Molecular Liquids* **2018,** *267*, 520-541.

44. Hamade, F.; Amit, S. K.; Woods, M. B.; Davis, V. A., The Effects of Size and Shape Dispersity on the Phase Behavior of Nanomesogen Lyotropic Liquid Crystals. *Crystals* **2020,** *10* (8), 715.

45. Flory, P. J., Phase Equilibria in Solutions of Rod-Like Particles. *Proceedings of the Royal Society of London. Series A. Mathematical and Physical Sciences* **1956,** *234* (1196), 73-89.

46. Green, M. J.; Parra-Vasquez, A. N. G.; Behabtu, N.; Pasquali, M., Modeling the Phase Behavior of Polydisperse Rigid Rods with Attractive Interactions with Applications to Single-Walled Carbon Nanotubes in Superacids. *The Journal of Chemical Physics* **2009,** *131* (8).

47. Dogic, Z.; Fraden, S., Ordered Phases of Filamentous Viruses. *Current Opinion in Colloid and Interface Science* **2006,** *11*, 47-55.

48. Doi, M.; Edwards, S., The Theory of Polymer Dynamics *Oxford University Press,* England **1986**.

49. Davis, V. A.; Ericson, L. M.; Parra-Vasquez, A. N. G.; Fan, H.; Wang, Y.; Prieto, V.; Longoria, J. A.; Ramesh, S.; Saini, R. K.; Kittrell, C.; Billups, W. E.; Adams, W. W.; Hauge, R. H.; Smalley, R. E.; Pasquali, M., Phase Behavior and Rheology of SWNTs in Superacids. *Macromolecules* **2004,** *37* (1), 154-160.

50. Khokhlov, A. R.; Semenov, A. N., Liquid-Crystalline Ordering in the Solution of Partially Flexible Macromolecules. *Physica A: Statistical Mechanics and its Applications* **1982,** *112* (3), 605-614.

51. Stroobants, A.; Lekkerkerker, H.; Odijk, T., Effect of Electrostatic Interaction on the Liquid Crystal Phase Transition in Solutions of Rodlike Polyelectrolytes. *Macromolecules* **1986,** *19* (8), 2232-2238.

52. Cotter, M. A.; Wacker, D. C., van der Waals Theory of Nematogenic Solutions. I. Derivation of the General Equations. *Physical Review A* **1978,** *18* (6), 2669-2675.

53. Wensink, H. H.; Vroege, G. J., Isotropic–Nematic Phase Behavior of Length-Polydisperse Hard Rods. *The Journal of Chemical Physics* **2003,** *119* (13), 6868-6882.

54. Kayser, R. F.; Raveché, H. J., Bifurcation in Onsager's Model of the Isotropic-Nematic Transition. *Physical Review A* **1978,** *17* (6), 2067-2072.

55. Khokhlov, A. R.; Semenov, A. N., On the Theory of Liquid-Crystalline Ordering of Polymer Chains with Limited Flexibility. *Journal of Statistical Physics* **1985,** *38* (1), 161-182.

56. Shundyak, K.; Roij, R. v., Isotropic-Nematic Interfaces of Hard-Rod Fluids. *Journal of Physics.: Condensed Matter* **2001,** *13* (21), 4789.

57. Lekkerkerker, H. N. W.; Coulon, P.; Van Der Haegen, R.; Deblieck, R., On the Isotropic-Liquid Crystal Phase Separation in a Solution of Rodlike Particles of Different Lengths. *The Journal of Chemical Physics* **1984,** *80* (7), 3427-3433.

58. Speranza, A.; Sollich, P., Isotropic-Nematic Phase Equilibria in the Onsager Theory of Hard Rods with Length Polydispersity. *Physical Review E* **2003,** *67* (6), 061702.

59. Speranza, A.; Sollich, P., Isotropic-Nematic Phase Equilibria of Polydisperse Hard Rods: The Effect of Fat Tails in the Length Distribution. *The Journal of Chemical Physics* **2003,** *118* (11), 5213-5223.

60. Davis, V. A., Liquid Crystalline Assembly of Nanocylinders. *Journal of Materials Research* **2011,** *26* (2), 140-153.

61. Hanson, E. G.; Shen, Y. R., Refractive Indices and Optical Anisotropy of Homologous Liquid Crystals. *Molecular Crystals and Liquid Crystals* **1976,** *36* (3-4), 193-207.

62. Hoffman, R. Michel-Levy Birefringence Chart. *Olympus LifeSciences* (accessed 8/15/2023).

63. Wissbrun, K. F., Rheology of Rod-Like Polymers in the Liquid Crystalline State. *Journal of Rheology* **1981,** *25* (6), 619-662.

64. Onogi, S.; Asada, T., Rheology and Rheo-Optics of Polymer Liquid Crystals. In *Rheology: Volume 1: Principles*, Astarita, G.; Marrucci, G.; Nicolais, L., Eds. Springer US: Boston, MA, 1980; pp 127-147.

65. Larson, R. G., The Structure and Rheology of Complex Fluids. *Oxford University Press* New York: 1999; Vol. 150.

66. Kumar, P.; Maiti, U. N.; Lee, K. E.; Kim, S. O., Rheological Properties of Graphene Oxide Liquid Crystal. *Carbon* **2014,** *80*, 453-461.

67. Ureña-Benavides, E. E.; Ao, G.; Davis, V. A.; Kitchens, C. L., Rheology and Phase Behavior of Lyotropic Cellulose Nanocrystal Suspensions. *Macromolecules* **2011,** *44* (22), 8990-8998.

68. Xu, T.; Davis, V. A., Rheology and Shear-Induced Textures of Silver Nanowire Lyotropic Liquid Crystals. *Journal of Nanomaterials* **2015,** *2015*, 939587.

69. Gogotsi, Y.; Anasori, B., The Rise of MXenes. *ACS Nano* **2019,** *13* (8), 8491-8494.

70. Pogorielov, M.; Smyrnova, K.; Kyrylenko, S.; Gogotsi, O.; Zahorodna, V.; Pogrebnjak, A., MXenes - A New Class of Two-Dimensional Materials: Structure, Properties and Potential Applications. *Nanomaterials* **2021,** *11* (12), 3412.

71. Naguib, M.; Kurtoglu, M.; Presser, V.; Lu, J.; Niu, J.; Heon, M.; Hultman, L.; Gogotsi, Y.; Barsoum, M. W., Two-Dimensional Nanocrystals Produced by Exfoliation of Ti_3AlC_2. *Advanced Materials* **2011,** *23* (37), 4248-4253.

72. Maleski, K.; Ren, C. E.; Zhao, M.-Q.; Anasori, B.; Gogotsi, Y., Size-Dependent Physical and Electrochemical Properties of Two-Dimensional MXene Flakes. *ACS Applied Materials & Interfaces* **2018,** *10* (29), 24491-24498.

73. Kim, J. E.; Han, T. H.; Lee, S. H.; Kim, J. Y.; Ahn, C. W.; Yun, J. M.; Kim, S. O., Graphene Oxide Liquid Crystals. *Angewandte Chemie International Edition* **2011,** *50* (13), 3043-3047.

74. Green, A. A.; Hersam, M. C., Emerging Methods for Producing Monodisperse Graphene Dispersions. *The Journal of Physical Chemistry Letters* **2010,** *1* (2), 544-549.

75. Balnois, E.; Durand-Vidal, S.; Levitz, P., Probing the Morphology of Laponite Clay Colloids by Atomic Force Microscopy. *Langmuir* **2003,** *19* (17), 6633-6637.

76. Hope, M. A.; Forse, A. C.; Griffith, K. J.; Lukatskaya, M. R.; Ghidiu, M.; Gogotsi, Y.; Grey, C. P., NMR Reveals the Surface Functionalisation of Ti_3C_2 MXene. *Physical Chemistry Chemical Physics* **2016,** *18* (7), 5099-5102.

77. Lukatskaya, M. R.; Kota, S.; Lin, Z.; Zhao, M.-Q.; Shpigel, N.; Levi, M. D.; Halim, J.; Taberna, P.-L.; Barsoum, M. W.; Simon, P.; Gogotsi, Y., Ultra-High-Rate Pseudocapacitive Energy Storage in Two-Dimensional Transition Metal Carbides. *Nature Energy* **2017,** *2* (8), 17105.

78. Naguib, M.; Mochalin, V. N.; Barsoum, M. W.; Gogotsi, Y., 25th Anniversary Article: MXenes: A New Family of Two-Dimensional Materials. *Advanced Materials* **2014,** *26* (7), 992-1005.

79. Huang, K.; Li, Z.; Lin, J.; Han, G.; Huang, P., Two-Dimensional Transition Metal Carbides and Nitrides (MXenes) for Biomedical Applications. *Chemical Society Reviews* **2018,** *47* (14), 5109-5124.

80. Liu, H.; Duan, C.; Yang, C.; Shen, W.; Wang, F.; Zhu, Z., A Novel Nitrite Biosensor Based on the Direct Electrochemistry of Hemoglobin Immobilized on MXene-Ti_3C_2. *Sensors and Actuators B: Chemical* **2015,** *218*, 60-66.

81. Liu, J.; Jiang, X.; Zhang, R.; Zhang, Y.; Wu, L.; Lu, W.; Li, J.; Li, Y.; Zhang, H., MXene-Enabled Electrochemical Microfluidic Biosensor: Applications toward Multicomponent Continuous Monitoring in Whole Blood. *Advanced Functional Materials* **2019,** *29* (6), 1807326.

82. VahidMohammadi, A.; Hadjikhani, A.; Shahbazmohamadi, S.; Beidaghi, M., Two-Dimensional Vanadium Carbide (MXene) as a High-Capacity Cathode Material for Rechargeable Aluminum Batteries. *ACS Nano* **2017,** *11* (11), 11135-11144.

83. VahidMohammadi, A.; Mojtabavi, M.; Caffrey, N. M.; Wanunu, M.; Beidaghi, M., Assembling 2D MXenes into Highly Stable Pseudocapacitive Electrodes with High Power and Energy Densities. *Advanced Materials* **2019,** *31* (8), 1806931.

84. Akuzum, B.; Maleski, K.; Anasori, B.; Lelyukh, P.; Alvarez, N. J.; Kumbur, E. C.; Gogotsi, Y., Rheological Characteristics of 2D Titanium Carbide (MXene) Dispersions: A Guide for Processing MXenes. *ACS Nano* **2018,** *12* (3), 2685-2694.

85. Ruzicka, B.; Zaccarelli, E., A Fresh Look at the Laponite Phase Diagram. *Soft Matter* **2011,** *7* (4), 1268-1286.

86. Honaker, K.; Vautard, F.; Drzal, L. T., Investigating the Mechanical and Barrier Properties to Oxygen and Fuel of High Density Polyethylene–Graphene Nanoplatelet Composites. *Materials Science and Engineering: B* **2017,** *216*, 23-30.

87. Tomás, H.; Alves, C. S.; Rodrigues, J., Laponite®: A Key Nanoplatform for Biomedical Applications? *Nanomedicine: Nanotechnology, Biology and Medicine* **2018,** *14* (7), 2407-2420.

88. Luckham, P. F.; Rossi, S., The Colloidal and Rheological Properties of Bentonite Suspensions. *Advances in Colloid and Interface Science* **1999,** *82* (1), 43-92.

89. Kissa, E., Dispersions: Characterization, Testing, and Measurement. *Routledge*: **2017**.

90. Wilkinson, N.; Metaxas, A.; Brichetto, E.; Wickramaratne, S.; Reineke, T. M.; Dutcher, C. S., Ionic Strength Dependence of Aggregate Size and Morphology on Polymer-Clay Flocculation. *Colloids and Surfaces A: Physicochemical and Engineering Aspects* **2017,** *529*, 1037-1046.

91. Liss, S. N.; Droppo, I. G.; Flannigan, D. T.; Leppard, G. G., Floc Architecture in Wastewater and Natural Riverine Systems. *Environmental Science & Technology* **1996,** *30* (2), 680-686.

92. van der Beek, D.; Lekkerkerker, H. N., Liquid Crystal Phases of Charged Colloidal Platelets. *Langmuir* **2004,** *20* (20), 8582-8586.

93. Mourchid, A.; Lécolier, E.; Van Damme, H.; Levitz, P., On Viscoelastic, Birefringent, and Swelling Properties of Laponite Clay Suspensions: Revisited Phase Diagram. *Langmuir* **1998,** *14* (17), 4718-4723.

94. Zhu, Y.; Murali, S.; Cai, W.; Li, X.; Suk, J. W.; Potts, J. R.; Ruoff, R. S., Graphene and Graphene Oxide: Synthesis, Properties, and Applications. *Advanced Materials* **2010,** *22* (35), 3906-3924.

95. Liu, F.; Chu, X.; Dong, Y.; Zhang, W.; Sun, W.; Shen, L., Acetone Gas Sensors Based on Graphene-$ZnFe_2O_4$ Composite Prepared by Solvothermal Method. *Sensors and Actuators B: Chemical* **2013,** *188*, 469-474.

96. Al-Ghamdi, A. A.; Gupta, R.; Kahol, P.; Wageh, S.; Al-Turki, Y.; El Shirbeeny, W.; Yakuphanoglu, F., Improved Solar Efficiency by Introducing Graphene Oxide in Purple Cabbage Dye Sensitized TiO_2 Based Solar Cell. *Solid State Communications* **2014,** *183*, 56-59.

97. Chen, Q.; Meng, Y.; Hu, C.; Zhao, Y.; Shao, H.; Chen, N.; Qu, L., MnO_2-Modified Hierarchical Graphene Fiber Electrochemical Supercapacitor. *Journal of Power Sources* **2014,** *247*, 32-39.

98. Novoselov, K. S.; Geim, A. K.; Morozov, S. V.; Jiang, D.; Zhang, Y.; Dubonos, S. V.; Grigorieva, I. V.; Firsov, A. A., Electric Field Effect in Atomically Thin Carbon Films. *Science* **2004,** *306* (5696), 666-669.

99. Hernandez, Y.; Nicolosi, V.; Lotya, M.; Blighe, F. M.; Sun, Z.; De, S.; McGovern, I. T.; Holland, B.; Byrne, M.; Gun'Ko, Y. K., High-Yield Production of Graphene by Liquid-Phase Exfoliation of Graphite. *Nature Nanotechnology* **2008,** *3* (9), 563-568.

100. Bonaccorso, F.; Bartolotta, A.; Coleman, J. N.; Backes, C., 2D-Crystal-Based Functional Inks. *Advanced Materials* **2016,** *28* (29), 6136-6166.

101. Amieva, E. J. C.; Lopez-Barroso, J.; Martínez-Hernández, A. L.; Velasco-Santos, C. Graphene-Based Materials Functionalization with Natural Polymeric Biomolecules, In *Recent Advances in Graphene Research,* Nayak, P. K., Ed. InTech: **2016**.

102. Naficy, S.; Jalili, R.; Aboutalebi, S. H.; Gorkin Iii, R. A.; Konstantinov, K.; Innis, P. C.; Spinks, G. M.; Poulin, P.; Wallace, G. G., Graphene Oxide Dispersions: Tuning Rheology to Enable Fabrication. *Materials Horizons* **2014,** *1* (3), 326-331.

103. Chen, S.; Zhu, J.; Han, Q.; Zheng, Z.; Yang, Y.; Wang, X., Shape-Controlled Synthesis of One-Dimensional MnO_2 via a Facile Quick-Precipitation Procedure and Its Electrochemical Properties. *Crystal Growth & Design* **2009,** *9* (10), 4356-4361.

104. Ye, S.; Stewart, I. E.; Chen, Z.; Li, B.; Rathmell, A. R.; Wiley, B. J., How Copper Nanowires Grow and How to Control Their Properties. *Accounts of Chemical Research* **2016,** *49* (3), 442-451.

105. Rathmell, A. R.; Bergin, S. M.; Hua, Y.-L.; Li, Z.-Y.; Wiley, B. J., The Growth Mechanism of Copper Nanowires and Their Properties in Flexible, Transparent Conducting Films. *Advanced Materials* **2010,** *22* (32), 3558-3563.

106. Chang, Y.; Lye, M. L.; Zeng, H. C., Large-Scale Synthesis of High-Quality Ultralong Copper Nanowires. *Langmuir* **2005,** *21* (9), 3746-3748.

107. Lewis, J. A., Direct Ink Writing of 3D Functional Materials. *Advanced Functional Materials* **2006,** *16* (17), 2193-2204.

108. Zhang, Y.; Liu, C.; Whalley, D. In *Direct-Write Techniques for Maskless Production of Microelectronics: A Review of Current State-of-the-Art Technologies*, 2009 International Conference on Electronic Packaging Technology & High Density Packaging, IEEE: 2009; pp 497-503.

109. Lewis, J. A.; Gratson, G. M., Direct Writing in Three Dimensions. *Materials Today* **2004,** *7* (7-8), 32-39.

110. Li, Q.; Lewis, J. A., Nanoparticle Inks for Directed Assembly of Three-Dimensional Periodic Structures. *Advanced Materials* **2003,** *15* (19), 1639-1643.

111. Li, W.; Li, F.; Li, H.; Su, M.; Gao, M.; Li, Y.; Su, D.; Zhang, X.; Song, Y., Flexible Circuits and Soft Actuators by Printing Assembly of Graphene. *ACS Applied Materials & Interfaces* **2016,** *8* (19), 12369-12376.

112. Zhang, Y.; Shi, G.; Qin, J.; Lowe, S. E.; Zhang, S.; Zhao, H.; Zhong, Y. L., Recent Progress of Direct Ink Writing of Electronic Components for Advanced Wearable Devices. *ACS Applied Electronic Materials* **2019,** *1* (9), 1718-1734.

113. Vigolo, B.; Penicaud, A.; Coulon, C.; Sauder, C.; Pailler, R.; Journet, C.; Bernier, P.; Poulin, P., Macroscopic Fibers and Ribbons of Oriented Carbon Nanotubes. *Science* **2000,** *290* (5495), 1331-1334.

114. Xu, Z.; Gao, C., Graphene Chiral Liquid Crystals and Macroscopic Assembled Fibres. *Nature Communications* **2011,** *2* (1), 571.

115. Fang, B.; Chang, D.; Xu, Z.; Gao, C., A Review on Graphene Fibers: Expectations, Advances, and Prospects. *Advacned Materials* **2020,** *32* (5), 1902664.

116. Wu, J., Understanding the Electric Double-Layer Structure, Capacitance, and Charging Dynamics. *Chemical Reviews* **2022,** *122* (12), 10821-10859.

117. Park, S.-J.; Seo, M.-K., Chapter 1 - Intermolecular Force. In *Interface Science and Technology*, Park, S.-J.; Seo, M.-K., Eds. Elsevier: **2011**; Vol. 18, pp 1-57.

118. Israelachvili, J. N., *Intermolecular and Surface Forces*. 3rd Ed. Academic Press: **2011**. https://doi.org/10.1016/B978-0-12-375182-9.10026-0.

119. Hao, T., Viscosities of Liquids, Colloidal Suspensions, and Polymeric Systems under Zero or Non-Zero Electric Field. *Advances in Colloid and Interface Science.* **2008,** *142* (1), 1-19.

120. Einstein, A., Eine Neue Bestimmung Der Moleküldimensionen. *Annalen der Physik* **1906,** *324* (2), 289-306.

121. Smoluchowski, M. v., Theoretische Bemerkungen Über Die Viskosität Der Kolloide. *Kolloid-Zeitschrift* **1916,** *18* (5), 190-195.

122. Rubio-Hernández, F. J.; Carrique, F.; Ruiz-Reina, E., The Primary Electroviscous Effect in Colloidal Suspensions. *Advances in Colloid and Interface Science* **2004,** *107* (1), 51-60.

123. Onsager, L.; Fuoss, R. M., Irreversible Processes in Electrolytes. Diffusion, Conductance and Viscous Flow in Arbitrary Mixtures of Strong Electrolytes. *The Journal of Physical Chemistry* **1932,** *36* (11), 2689-2778.

124. Stone-Masui, J.; Watillon, A., Electroviscous Effects in Dispersions of Monodisperse Polystyrene Latices. *Journal of Colloid and Interface Science* **1968,** *28* (2), 187-202.

125. Booth, F., The Electroviscous Effect for Suspensions of Solid Spherical Particles. *Proceedings of the Royal Society of London. Series A. Mathematical and Physical Sciences* **1950,** *203* (1075), 533-551.

126. Watterson, I. G.; White, L. R., Primary Electroviscous Effect in Suspensions of Charged Spherical Particles. *Journal of the Chemical Society, Faraday Transactions 2: Molecular and Chemical Physics* **1981,** *77* (7), 1115-1128.

127. Chan, F.; Goring, D., The Primary Electroviscous Effect in a Sulfonated Polystyrene Latex. *Journal of Colloid and Interface Science* **1966,** *22* (4), 371-377.

128. Li, J.; Cheng, Y.; Chen, X.; Zheng, S., Impact of Electroviscous Effect on Viscosity in Developing Highly Concentrated Protein Formulations: Lessons from Non-Protein Charged Colloids. *International Journal of Pharmaceutics: X* **2019,** *1*, 100002.

129. Trefalt, G.; Borkovec, M., Overview of DLVO Theory. *Laboratory of Colloid and Surface Chemistry, University of Geneva, Switzerland* **2014,** *304*.

130. Mohona, T. M.; Gupta, A.; Masud, A.; Chien, S.-C.; Lin, L.-C.; Nalam, P. C.; Aich, N., Aggregation Behavior of Inorganic 2D Nanomaterials Beyond Graphene: Insights from Molecular Modeling and Modified DLVO Theory. *Environmental Science & Technology* **2019,** *53* (8), 4161-4172.

131. Akbari, A.; Sheath, P.; Martin, S. T.; Shinde, D. B.; Shaibani, M.; Banerjee, P. C.; Tkacz, R.; Bhattacharyya, D.; Majumder, M., Large-Area Graphene-Based Nanofiltration Membranes by Shear Alignment of Discotic Nematic Liquid Crystals of Graphene Oxide. *Nature Communications* **2016,** *7*, 10891.

132. Orangi, J.; Hamade, F.; Davis, V. A.; Beidaghi, M., 3D Printing of Additive-Free 2D $Ti_3C_2T_x$ (MXene) Ink for Fabrication of Micro-Supercapacitors with Ultra-High Energy Densities. *ACS Nano* **2020,** *14* (1), 640-650.

133. Naguib, M.; Mashtalir, O.; Carle, J.; Presser, V.; Lu, J.; Hultman, L.; Gogotsi, Y.; Barsoum, M. W., Two-Dimensional Transition Metal Carbides. *ACS Nano* **2012,** *6* (2), 1322-1331.

134. Eom, W.; Shin, H.; Ambade, R. B.; Lee, S. H.; Lee, K. H.; Kang, D. J.; Han, T. H., Large-Scale Wet-Spinning of Highly Electroconductive MXene Fibers. *Nature Communications* **2020,** *11* (1), 2825.

135. Murali, S.; Xu, T.; Marshall, B. D.; Kayatin, M. J.; Pizarro, K.; Radhakrishnan, V. K.; Nepal, D.; Davis, V. A., Lyotropic Liquid Crystalline Self-Assembly in Dispersions of Silver Nanowires and Nanoparticles. *Langmuir* **2010,** *26* (13), 11176-11183.

136. Li, S.; Chen, Y.; Huang, L.; Pan, D., Large-Scale Synthesis of Well-Dispersed Copper Nanowires in an Electric Pressure Cooker and Their Application in Transparent and Conductive Networks. *Inorganic Chemistry* **2014,** *53* (9), 4440-4444.

137. Song, H. Y.; Salehiyan, R.; Li, X.; Lee, S. H.; Hyun, K., A Comparative Study of the Effects of Cone-Plate and Parallel-Plate Geometries on Rheological Properties under Oscillatory Shear Flow. *Korea-Australia Rheology Journal* **2017,** *29* (4), 281-294.

138. Iqbal, A.; Hong, J.; Ko, T. Y.; Koo, C. M., Improving Oxidation Stability of 2D MXenes: Synthesis, Storage Media, and Conditions. *Nano Convergence* **2021,** *8* (1), 9.

139. Tkacz, R.; Abedin, M. J.; Sheath, P.; Mehta, S. B.; Verma, A.; Oldenbourg, R.; Majumder, M., Phase Transition and Liquid Crystalline Organization of Colloidal Graphene Oxide as a Function of pH. *Particle & Particle Systems Characterization* **2017,** *34* (9), 1600391.

140. Bates, M. A.; Frenkel, D., Nematic–Isotropic Transition in Polydisperse Systems of Infinitely Thin Hard Platelets. *The Journal of Chemical Physics* **1999,** *110* (13), 6553-6559.

141. Haywood, A. D.; Weigandt, K. M.; Saha, P.; Noor, M.; Green, M. J.; Davis, V. A., New Insights into the Flow and Microstructural Relaxation Behavior of Biphasic Cellulose Nanocrystal Dispersions from Rheosans. *Soft Matter* **2017,** *13* (45), 8451-8462.

142. Orts, W. J.; Godbout, L.; Marchessault, R. H.; Revol, J. F., Enhanced Ordering of Liquid Crystalline Suspensions of Cellulose Microfibrils: A Small Angle Neutron Scattering Study. *Macromolecules* **1998,** *31* (17), 5717-5725.
143. Zhang, S.; Li, Q.; Kinloch, I. A.; Windle, A. H., Ordering in a Droplet of an Aqueous Suspension of Single-Wall Carbon Nanotubes on a Solid Substrate. *Langmuir* **2010,** *26* (3), 2107-2112.
144. Geng, H.; Yao, B.; Zhou, J.; Liu, K.; Bai, G.; Li, W.; Song, Y.; Shi, G.; Doi, M.; Wang, J., Size Fractionation of Graphene Oxide Nanosheets Via Controlled Directional Freezing. *Journal of the American Chemical Society* **2017,** *139* (36), 12517-12523.
145. Kayali, E.; VahidMohammadi, A.; Orangi, J.; Beidaghi, M., Controlling the Dimensions of 2D MXenes for Ultrahigh-Rate Pseudocapacitive Energy Storage. *ACS Applied Materials & Interfaces* **2018,** *10* (31), 25949-25954.
146. Verhoeff, A.; Wensink, H.; Vis, M.; Jackson, G.; Lekkerkerker, H., Liquid Crystal Phase Transitions in Systems of Colloidal Platelets with Bimodal Shape Distribution. *The Journal of Physical Chemistry B* **2009,** *113* (41), 13476-13484.
147. Khokhlov, A. R., Theories Based on the Onsager Approach. In *Liquid Crystallinity in Polymers*, Ciferri, A., Ed. VCH Publishers: New York, 1991; pp 97-129.
148. Buffa, J. M.; Casado, U.; Mucci, V.; Aranguren, M. I., Cellulose Nanocrystals in Aqueous Suspensions: Rheology of Lyotropic Chiral Liquid Crystals. *Cellulose* **2019,** *26* (4), 2317-2332.
149. Davis, V. A., Liquid Crystalline Assembly of Nanocylinders. *Journal of Materials Research* **2011,** *26*, 140 - 153
150. Urena-Benavides, E. E.; Ao, G.; Davis, V. A.; Kitchens, C. L., Rheology and Phase Behavior of Lyotropic Cellulose Nanocrystal Suspensions. *Macromolecules* **2011,** *44* (22), 8990-8998.
151. van Olphen, H., Internal Mutual Flocculation in Clay Suspensions. *Journal of Colloid Science* **1964,** *19* (4), 313-322.
152. Rueb, C. J.; Zukoski, C. F., Viscoelastic Properties of Colloidal Gels. *Journal of Rheology* **1997,** *41* (2), 197-218.
153. Zaccone, A.; Winter, H. H.; Siebenbürger, M.; Ballauff, M., Linking Self-Assembly, Rheology, and Gel Transition in Attractive Colloids. *Journal of Rheology* **2014,** *58* (5), 1219-1244.
154. Shafiei-Sabet, S.; Hamad, W. Y.; Hatzikiriakos, S. G., Ionic Strength Effects on the Microstructure and Shear Rheology of Cellulose Nanocrystal Suspensions. *Cellulose* **2014,** *21* (5), 3347-3359.
155. Hamade, F., Advances in Understanding Graphene Hybrids and MXenes. **2023**.